3-2022

Effects of Cone Tip Changes On Wall-Cooled Hypersonic Boundary Layer Transition and Turbulence

Mathew M. Major

Follow this and additional works at: https://scholar.afit.edu/etd

Part of the Aerospace Engineering Commons

**EFFECTS OF CONE TIP CHANGES ON WALL-COOLED HYPERSONIC
BOUNDARY LAYER TRANSITION AND TURBULENCE**

THESIS

Mr. Mathew M. Major, USAF

AFIT-ENY-MS-22-M-307

**DEPARTMENT OF THE AIR FORCE
AIR UNIVERSITY**

AIR FORCE INSTITUTE OF TECHNOLOGY

Wright-Patterson Air Force Base, Ohio

AFIT-ENY-MS-22-M-307

EFFECTS OF CONE TIP CHANGES ON WALL-COOLED HYPERSONIC
BOUNDARY LAYER TRANSITION AND TURBULENCE

THESIS

Presented to the Faculty

Department of Aeronautics and Astronautics

Graduate School of Engineering and Management

Air Force Institute of Technology

Air University

Air Education and Training Command

In Partial Fulfillment of the Requirements for the

Degree of Master of Science in Aeronautical Engineering

Mr. Mathew M. Major, BS

USAF

March 2022

DISTRIBUTION STATEMENT A.
APPROVED FOR PUBLIC RELEASE; DISTRIBUTION UNLIMITED.

AFIT-ENY-MS-22-M-307

EFFECTS OF CONE TIP CHANGES ON WALL-COOLED HYPERSONIC
BOUNDARY LAYER TRANSITION AND TURBULENCE

Mr. Mathew M. Major, BS

USAF

Committee Membership:

Dr. Mark F. Reeder, PhD
Chair

Lt Col Darrell Crowe, PhD
Member

Lt Col Jeffery Komives, PhD
Member

AFIT-ENY-MS-22-M-307

Abstract

Boundary layer measurements took place at the Air Force Research Laboratory's (AFRL) Mach-6 Ludweig Tube using a 7-degree half-angle, single piece cone with a spherically blunted tip of 1.5 mm radius. Experiments compared uncooled and cooled flow conditions on the blunt-nosed model, and then were closely examined with respect to previous data collected for a sharp-tipped cone of similar geometry. Liquid nitrogen (LN2) circulation within an internal cavity achieved the desired surface cooling conditions. High-speed Schlieren data obtained at 600 kHz obtained relevant boundary layer flow data. The direct comparison was then made between blunt-tipped and sharp-tipped cone data at an uncooled surface temperature of 298 K ($T_w/T_0 = .59$) and a cooled surface temperature at an average of 95 K ($T_w/T_0 = .19$). Comparisons were made at similar freestream unit Reynolds numbers across an order of magnitude of initial tunnel driver tube pressures ($Re_\infty = 2.7 \times 10^6$ /m $- 2.7 \times 10^7$ /m) over the length of the 0.61 m (24-inch) long cone. Decreasing surface temperature delayed transition onset and decreased boundary layer thickness on the blunt-tipped cone. Some stabilization of transition onset location occurred, consistent with the known effects of entropy-layer swallowing effects. Blunting significantly delayed transition to turbulence when compared to the sharp-tipped case in both uncooled and cooled surface conditions. Dominant frequencies of Mack's second mode instabilities increased with a decrease in surface temperature, which is consistent with the resulting thinner boundary layer.

Table of Contents

List of Figures

List of Tables

List of Abbreviations

Abbreviation

AFRL	Air Force Research Laboratory
AFIT	Air Force Institute of Technology
TPS	Thermal Protection System
HIFiRE	Hypersonic International Flight Research Experimentation
mm	Millimeter
in	Inches
ft	Feet
CFD	Computational Fluid Dynamics
TS	Tollmien-Schlichting
LST	Linear Stability Theory
DNS	Direct Numerical Simulation
HWT	Hypersonic Wind Tunnel
BAM6QT	Boeing/AFOSR Mach-6 Quiet Tunnel
FFT	Fast Fourier Transform
QS	Quasi-Steady State
CAD	Computer Aided Design
Ppm	Parts Per Million
LN2	Liquid Nitrogen
PPE	Personal Protective Equipment
PCX	Plano-convex
PFV	Photron FASTCAM Viewer

FPS   Frames per second

PSD   Power Spectral Density

List of Symbols

Symbol

δ	Hydrodynamic Boundary Layer Thickness
u_e	Streamwise Velocity at the Edge of the Hydrodynamic Boundary Layer
δ_T	Thermal Boundary Layer Thickness
u_∞	Freestream Velocity
T_w	Wall Temperature
T_e	Temperature at the Edge of the Boundary Layer
T_0	Stagnation Temperature
T_∞	Freestream Temperature
Re_x	Local Reynolds Number at a Distance x
ρ_∞	Freestream Density
x	Distance
μ_∞	Freestream Kinematic viscosity
T_w	Surface or Wall Temperature
M_∞	Freestream Mach Number
γ	Ratio of Specific Heats at Constant Pressure and Volume
T_{ad}	Adiabatic Temperature
T_R	Recovery Temperature
P_0	Stagnation Pressure
P_{DT}	Driver Tube Pressure
T_{DT}	Driver Tube Temperature
ρ_0	Stagnation Density

R   Specific Gas Constant

Re_∞/L Reynolds Number per Unit Length

In   inches

L   Liters

W   Watts

A   Leading Coefficient

R_n Nose radius

R_b Base Radius

EFFECTS OF CONE TIP CHANGES ON WALL-COOLED HYPERSONIC BOUNDARY LAYER TRANSITION AND TURBULENCE

I. Introduction

In recent years, there have been many advances in the field of hypersonic flight as the practicality of vehicles having hypersonic capabilities became of increasing interest. Although this interest brought about increased attention to research and development, there remain several challenging areas with phenomenon that remain uncharacterized or disputed. Among these challenges is the effect of wall temperatures on boundary layer conditions. In real world flight conditions, the surface temperatures of many vehicles in the hypersonic regime are generally much lower than the stagnation temperatures experienced. This affects the boundary layer thickness and flow state (i.e. laminar, transitioning, or turbulent), which in turn affects the design of thermal management of the vehicle. Reproducing this effect presents unique challenges to wind tunnel testing. Temperature control of model walls can be difficult to achieve, and prior work investigating the full effect of wall temperature on boundary layer growth and conditions has not provided conclusive results. Recent work done by the Air Force Research Laboratory (AFRL) and the Air Force Institute of Technology (AFIT) has added to this body of research for the case of a sharp tipped cone. The present effort expands on this work to gather evidence on the effects of introducing a sphere-tipped (blunt) geometry.

1.1 Background and Motivation

There exists an abundance of material in both experimental and analytical evidence for the characterization and study of factors that affect boundary layer transition from laminar to turbulent flow for subsonic and even for some supersonic flight conditions below the Mach-5 general hypersonic threshold. For hypersonic flight, the prediction of boundary layer transition remains a challenge, with differing experimental results and theoretical predictions. This information can be critical for the design of hypersonic vehicles as the state of the boundary layer influences both controllability of the vehicle and the implementation of the Thermal Protection System (TPS) of the craft. Due to the high boundary layer temperatures relative to the body surface, thermal management is a more demanding design consideration during hypersonic flow as compared to slower flight regimes. Much of the heat transfer that the craft experiences is determined by this state of the boundary layer, where the difference between laminar, turbulent, and transitioning flow can lead to an order of magnitude effect on surface heating load [1] [2]. Accurate prediction of the boundary layer states can lead to design optimization of TPS installation allowing for the prioritization of areas more at risk for higher heating.

Boundary layer instabilities are the primary cause for turbulence transition from laminar flow to turbulent flow, and caused by either internal or external disturbances to the boundary layer [3]. Destabilizing internal disturbances present at lower speeds, such as Mack's first mode waves, are stabilized at hypersonic speeds due to sonic line reflections in the boundary layer, and thus higher mode instabilities dominate transition [4]. These second mode instability waves are highly temperature dependent, and thus the wall temperature may become an important factor in affecting the onset of turbulence in the

boundary layer. The temperature ratio between wall and stagnation temperatures, sometimes described as a cooled-wall condition because of the extraordinarily high stagnation temperatures seen in hypersonic flight conditions, is one of particular interest as to the exact effect on transition. Creating a cooled-wall condition is typically a difficult challenge in many models and experimental configurations, resulting in the exact effect of the cold wall condition remaining inconclusive. This topic has been explored in many analytical and experimental studies, but no consensus has been reached due to conflicting results [5] [6] [7]. Cooled-wall conditions are of particular importance to real-world flight, as flight articles regularly fly in regimes of low surface temperature and high flow stagnation temperature. The Hypersonic International Flight Research Experimentation (HIFiRE-5) series of flight tests experienced a wall-to-stagnation temperature ratio of about .2, classifying the flight test as occurring in nominal cooled-wall conditions [8].

Currently, due to the high cost and difficulty of performing hypersonic flight tests, significantly more boundary layer data collected in ground tests in various wind tunnels than have been performed through flight tests. This data is collected to both verify and update existing analytical and computer models, but also to gain insight into the physical phenomenon that affect potential flight article designs in flight. While the variations among wind tunnels can influence the results presented in ways not identical to real life flight conditions, such as tunnel wall effects and freestream noise, wind tunnel data still provides valuable insight into the processes related to transition and turbulence.

1.2 Research Objectives

Past research on this topic performed by AFIT/AFRL upon which this thesis expands includes work conducted by Lieutenant Ryan Oddo and Captain Joshua Embrador. Oddo's research established a method of Schlieren imaging for gathering data and used said method to gain preliminary insight into boundary layer transition on a 7° half-angle sharp-tipped cone in hypersonic conditions [9]. Embrador's research expanded to a more full characterization of the same test article of boundary layer flow and surface temperature distribution of the cone to identify the transition region and examine disturbance mechanisms [10]. Both research efforts concluded that the effect of cooling the cone surface with liquid nitrogen thinned the boundary layer and delayed boundary layer transition when compared to the uncooled case. Embrador's work also concluded that the frequency of the observed modes shifted towards higher frequencies in the cooled cone case. Oddo's work postulated that wall cooling "in-and-of-itself" might be what led to the effects of boundary layer transition delay [11]. Both these research efforts explored only cooled wall transition effects on cones with sharp tips (i.e. tips where the radius of the cone's nose is much smaller than the radius of the cone base, to the point where it is practically a sharp cone). To build on past efforts, the current work used an altered cone model with a rounded, more blunt-tipped nose in wind tunnel experimentation. This attempts to characterize boundary layer transition and surface temperature distribution for both cooled and uncooled cases on the blunted cone.

The objective of this current research was to implement the method presented by Oddo, utilize the flow conditions and cooling capabilities set by Embrador, then apply them to wind tunnel testing on a 7° half-angle cone with a blunt, rounded tip of 1.5 millimeter

4

(mm) radius. A characterization of both cooled and uncooled conditions allowed for a comparison of significant changes in boundary layer flow from past research. The addition of the rounded tip introduces an entropy layer which could alter the observed trends of previous research, specifically through the production of eddies in the near wall region. The work of this thesis lays out a more complete understanding of the effects of extreme wall cooling on cones with different nose geometries, specifically relating to boundary layer transition locations and the development of instability mechanisms. The interplay of wall cooling and nose-tip blunting was of interest to investigate in order to observe the combined effects towards delay. Although experimental data exists that each delays transition individually, the non-linear nature of the internal disturbances infers the possibility that the effects of each do not necessarily combine to increase this effect when together [11] [12].

High-Speed Schlieren imaging captured and visualized boundary layer transition data for the purposes of the current work. Schlieren is a non-intrusive mechanism that provided a means of calculating transition Reynolds number, turbulence intermittency statistics, and instability frequencies. These values were compared both to the conditions gathered in current efforts, but also to the past work on sharp cones performed by Embrador.

1.3 Thesis Overview

This thesis is structured beginning with a literature review in Chapter II, which presents the basic theory of boundary layers, turbulent flow, the physical characterization of hypersonic flow, and linear boundary layer stability theory. It also outlines past

experimental and analytical research as well as test data reflecting the current knowledge of both wall temperature effects and cone geometry on boundary layer transition. Chapter III provides a description of the test facility, used test apparatuses, data acquisition methods, cooling systems, and experimental procedures and methodology. Chapter IV presents the overall results, as well as compared to past results from previous studies both done at AFIT/AFRL and other sources. Chapter V discusses final thoughts and recommendations for future research.

II. Literature Review

In hypersonic flows, heat flux and shear forces generated by the boundary layer can be orders of magnitude higher than that in lower-speed flight regimes. Heat flux, primarily, is an overwhelming driver of design in hypersonic vehicles. Predicting a more accurate location of turbulence transition in the boundary layer during hypersonic flight can lead to an optimization of design parameters such as the TPS, which can increase overall performance and survivability. The literature review will cover the basic theory and current pertinent research and experimental data relevant to the research performed in this thesis.

2.1 The Boundary Layer

When flowing fluid encounters a solid object or wall within a flow, at the contact point between these two the flow conditions of the fluid must match the conditions of the wall or the body due to the effects of diffusion. These collective conditions are termed the no-slip boundary conditions, called so because this prevents slipping layers between the near-wall flow conditions and some solid boundary to the fluid. Beyond an initial fluid layer which matches the boundary, a near-wall region is formed which extends normal to the boundary surface in which velocity, temperature, and momentum of the flow all gradually change to that of the free stream. Each of these gradients correspond to a thickness, δ, which defines a boundary layer. The boundary layer is the region with thickness δ in which the flow transitions from the solid boundary condition to 99% of the freestream condition [13]. As noted, there exists a few different types of boundary layers, depending on the flow variable examined. These are the hydrodynamic boundary layer, the

7

momentum boundary layer, and the thermal boundary layer. For the purposes of this paper, the hydrodynamic and thermal boundary layers receive special consideration.

The hydrodynamic boundary layer is the area in which the transition of velocity from boundary conditions to freestream conditions in the direction normal to the boundary surface occurs. The edge of the boundary layer is defined where the streamwise component of the velocity, u_e, is 99% of the freestream streamwise velocity component u_∞. In the standard wind tunnel inertial reference frame, the solid boundary is an object assumed to be at rest and the freestream flow is the freely moving object. Similarly, the thermal boundary layer is the area in which the temperature transitions from the wall temperature, T_w, to the freestream temperature, T_e, in the direction normal the boundary surface that is 99% of the freestream static temperature T_∞. Both of these boundary layers exhibit different boundary layer thicknesses and are generally denoted by δ for the hydrodynamic boundary layer thickness and δ_T for the thermal boundary layer thickness. Figure 1 shows a qualitative example of each boundary layer in a general case and the respective profiles at specific downstream locations.
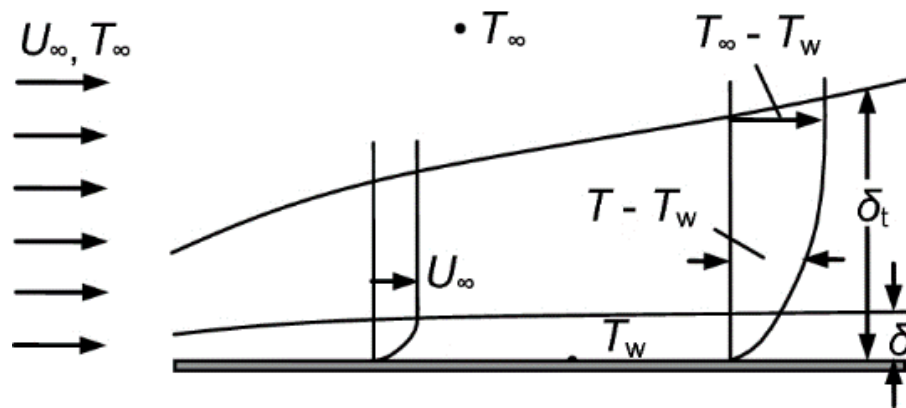
Figure 1: General Depiction of Laminar Hydrodynamic and Thermal Boundary Layers [14]

8

Non-dimensional parameters in the subsonic and supersonic cases, namely the Reynolds number for the hydrodynamic boundary layer and the Prandtl number for the thermal boundary layer, are relevant measures for the thicknesses of both categories of boundary layers. In principle, these two boundary layer thicknesses differ from one another. However, in gases of moderate temperature where both the Prandtl number and the Schmidt number, a non-dimensional ratio of momentum and mass diffusivity, are close to one, then both boundary layers approach the same thickness by the Reynolds analogy [15].

The conditions of development of these boundary layers produces measurable effects in both wind tunnel and real world flight conditions, and can influence design parameters for vehicles. The varying of these conditions impacts the shear drag and the heat transfer that are experienced by a vehicle in a given flight condition. These two effects are dependent of each other generally, as the kinetic energy lost in the hydrodynamic boundary layer increases the thermal energy gradients present in the thermal boundary layer.

2.2 Turbulent Flow

Flow within the boundary layer can exist within one of three states: laminar, turbulent and transitional flow. While laminar flow produces neat orderly flow with streamlines parallel to each other, turbulent flow is a more chaotic type of flow. Qualitatively, turbulent flow consists of small ever-decreasing three-dimensional vortices known as eddie vortices. These eddies lead to mixing and dissipation throughout the boundary layer. The mixing due to turbulence in turn causes high momentum fluid to

approach the surface, causing both increased drag and heat flux from the body. Transitional flow is the short region in which instable flow structures generated first in laminar flow grow and develop into fully turbulent flow. Figure 2 shows a schematic describing all three boundary layer states.
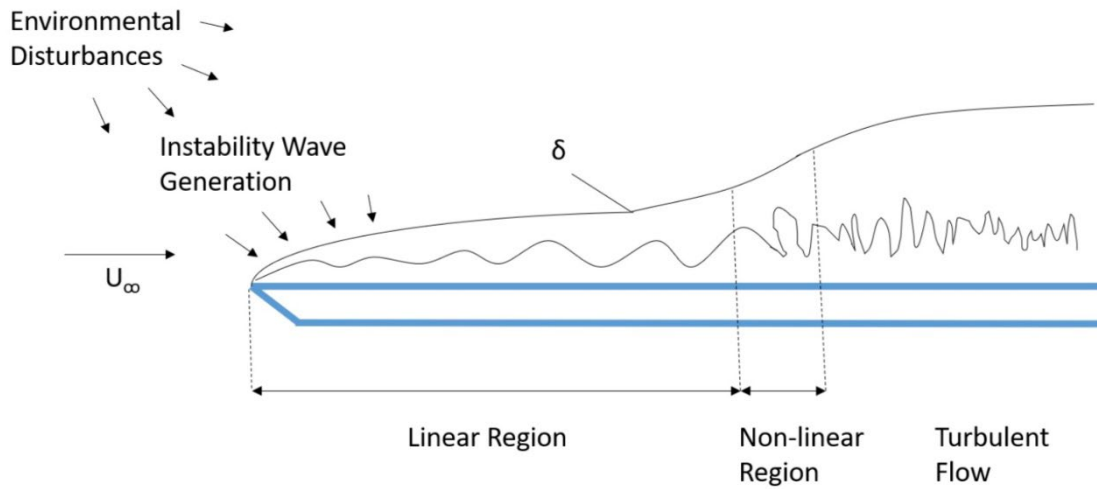
Figure 2: General Depiction of The Regions and Mechanism of Turbulence Transition [10]

The flow state of the boundary layer at any given position trends with the local Reynolds number, analytically given as:

$$Re_x = \frac{\rho_\infty u_\infty x}{\mu_\infty} \tag{1}$$

where ρ_∞ is the freestream density, x is the position along the length, and μ_∞ is the freestream kinematic viscosity. A general "rule-of-thumb" is that turbulence begins around the point Re_x is $4\text{x}10^6$ up to $6\text{x}10^6$. This generality, however, is not universal as transition to turbulence depends on many factors. Transition to turbulence is a function of freestream conditions, as well as surface roughness and curvature, local Mach number, and many other factors [15].

Models of transitional and turbulent flow, due to this complexity, use computational fluid dynamic (CFD) algorithms to solve for variables such as temperature, pressure, or even expected eddy size and turbulence intensity. As freestream velocity increases to the hypersonic regime, and since the scale of resolution needed on the simulation becomes increasingly small as the boundary layer gets thinner at higher Mach numbers, the grid resolution needed to fully simulate and characterize boundary conditions is exceptionally large and requires significant resources. Therefore, to both validate existing models and to correct and adjust them for real world deviations, experimental data obtained anchors the development and implementation of CFD models.

2.3 Analytical Prediction Techniques of High Speed Flow

This thesis examines experimentally a right circular cone with a 1.5 mm spherical, blunt nose tip incidental at zero-degree angle of attack and yaw, as described fully in Section 3.2. There are key analytical prediction techniques in high Mach number test conditions that can determine key factors in the flow. These include the shock angle and boundary layer thickness given the general geometry of the cone, the speed of the flow, and the effects of cooling the surface.

After an initial bow shock region due to the cone tip being blunt, the cone will experience an oblique shock developed at a low angle relative to the surface of the cone. The amount of the cone surface over which the oblique region extends versus that of the bow shock is dependent on how blunt the upstream region of the cone is precisely. When a fluid traveling at supersonic speeds flows past a three-dimensional cone, streamline curving and relieving effects serve to both decrease shock angle and reduce surface

11

pressure when compared to the oblique shock wave effects on the analogous 2D wedge case [13]. When desiring the inviscid pressure effects behind the shock wave, the Taylor-Maccoll equations for a sharp-tipped cone numerically approach a solution. The addition of boundary layer effects slightly increase the angle that the oblique shock makes with respect to the cone.

Additionally, the surface layer temperature plays a role in the prediction of boundary layer thickness. The thermal boundary layer thickness is often a function of the heat transfer and therefore the temperature differential is an important factor in the development of thermal boundary layer [16]. Therefore, in characterizing the effect of wall temperature on the boundary layer, the wall-to-boundary layer-edge temperature ratio, defined as the ratio between the wall temperature and the temperature at the edge of the boundary layer (T_w/T_e), is a useful measure. While the Taylor-Maccoll method only strictly applies for perfectly sharp cones, its values can still provide a reasonable basis for comparison for a blunt-nose cone to the sharp-tipped case when the radius of the blunt-nose is much less (i.e. orders of magnitude less) than the distance on the cone being examined. Both wall-to-boundary layer-edge temperature ratio and the wall-to-stagnation temperature ratio (T_w/T_0) will be the main temperature ratios of focus throughout this thesis for purposes of comparison to past data and substantial measure of cooling effect.

Additionally, both the velocity and thermal boundary layers are self-similar in the non-dimensional case [17]. This can be exemplified by the findings of Van Driest, who computed velocity profiles at varying Mach numbers for both an insulated flat plate and a cold wall (T_w/T_e=.25) flat plate [18]. Figure 3 shows a sample of the solutions found by Van Driest comparing the adiabatic wall case to a cold wall case where the wall

12

temperature was one-fourth of the temperature at the edge of the boundary layer ($T_w/T_e = .25$).

Generally, the figure presents that a decrease in wall-temperature ratio corresponds to a decrease in expected boundary layer thickness for similar Mach numbers. Specifically, at the Mach number of interest to the current work (M~6), the figure presents that the non-dimensional boundary layer thickness (y-axis) is more than doubled at the edge of the boundary layer (u/u_e) between the cold-wall case (~8) and the adiabatic case (~18). An explanation of this is given by Anderson, that through the equation of state ($P=\rho RT$), a lower wall temperature must increase density since in a boundary layer pressure does not vary in the direction normal to the wall. Conservation of mass then states that for the same mass flow rate (velocity being constant), the boundary layer thickness must therefore decrease [13]. Given these conditions, the boundary layer thickness shows dependence on Mach number, Prandtl number, and the wall temperature ratio.
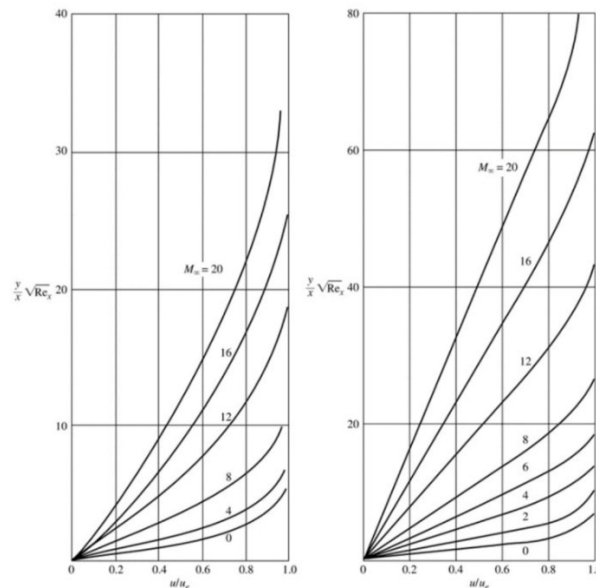
Figure 3: Velocity Profiles Over a Flat Plate for Various Mach Numbers, cold wall (left, T_w/T_e=.25) and adiabatic wall (right) [19]

2.4 Physical Characteristics of Hypersonic Flows

Flow at which the freestream velocity is at Mach 5 or greater typically characterizes hypersonic flow. This, however, is only an accepted approximation to generalize a regime at which the effects of hypersonic flow begin. Hypersonic flow is distinct from supersonic flow instead by the start of specific physical changes to the flow, which Anderson [20] describes within terms of viscous interactions, thin shock layers, the development of an entropy layer, high temperature flows, and low-density flows. This section details the physical effects of hypersonic flow that are of particular interest to the current work.

At subsonic and supersonic speeds, boundary layer growth grows purely as a function of Reynolds number and Mach number. For the case of a flat plate under laminar, adiabatic, compressible flow, Anderson [20] stated that a proportional relationship that the laminar boundary layer thickness, δ, described by:

$$\delta \propto \frac{M_\infty^2}{\sqrt{Re_x}} \tag{2}$$

where M_∞ is the freestream Mach number and Re_x is the Reynolds number at a point x along the flat plate. In hypersonic conditions, a solid wall influencing near-field flow is no longer the sole factor dominating the growth of the boundary layer. Instead, the high temperatures present in hypersonic flows begin to take significant effect on boundary layer growth. Hypersonic boundary layers generally increase in thickness at much more rapid rate than at slower speeds due to the viscous dissipation of the high-speed flow near the wall. This extended boundary layer then interacts with what would otherwise be purely inviscid phenomenon in lower speed regimes.

Significant entropy gradients are also a concern in boundary layer analysis in many hypersonic regimes that are not similarly present at lower speeds. Crocco's theorem states

changing shock angles (which can result from curvature on the vehicle body) will create strong entropy gradients [13]. These entropy gradients create an ensuing entropy layer close to the vehicle body. Due to the relatively small shock layer, the entropy layer creates vorticity that interacts with the boundary layer and complicates analysis.

Due to the high kinetic energy present in hypersonic flows, the temperature increases extraordinarily high due to both shock wave interactions and impacts caused by thin boundary and shock layers. These high temperatures manifest in several ways. The first is a breakdown of the standard assumption in most other aerodynamics of the presence of a calorically perfect gas. This is especially important within the boundary layer as the high temperatures close to the wall can be a significant point of potential damage due to ablation or other forms of destruction of the TPS. Ordinarily, the changes in chemical and thermal properties occur sufficiently fast within the flow such that an assumption of chemical and vibrational equilibrium is sufficient. For the Mach numbers present in the current work, the current work assumes a constant specific heat ratio of 1.4 and a calorically perfect gas in the flow. Although an approximation, the stagnation temperatures observed in experimentation do not indicate a significant change in specific heat ratio otherwise in worse case scenarios (about a 1.3% difference at 505 K).

2.5 Boundary Layer Transition

In between the regions of the boundary layer where flow is either fully turbulent or fully laminar, there is a region of transition within which the straight and parallel streamlines of laminar flow begin to develop into the eddy vortices, which make up turbulent flow. Reynolds, Taylor, and Prandtl performed early work to first predict and

15

characterize the causes of transition [13]. This led to the development of the Reynold number as a method of predicting transition, as establish viscosity as a destabilizing factor in boundary layer transition. This theoretical and experimental work in boundary layer transition allowed for design and optimization work in both subsonic and supersonic regimes; however, expanding this work to gain further insight into boundary layer transition phenomenon during hypersonic flight is still an area of active research. Ablation and surface roughness, as well as instabilities due to specific wind tunnel facilities, can further complicate where and how transition occurs [21].

The general development of the theory behind the full characterization of boundary layer transition to turbulence had its first general foundation in the 1950s, when the field of linear stability theory began to form as an explanation of transition mechanisms. Beginning from the basis point of the incompressible, viscous Navier-Stokes equations, linear stability theory studies the growth of small disturbance waves, generated by environmental disturbances, in the boundary layer parallel to the wall [3]. These waves are Tollmien-Schlichting (TS) waves or simply instability waves. Linear stability theory states that these waves, within a given transition region where amplitudes are small enough, change slowly enough such that they grow linearly in space and time in a local region. External stimuli generate the instability waves that enter the flow, then confine and amplify them within in the boundary layer. Outside the boundary layer, these small disturbances would otherwise exponentially decay. These external stimuli could come from a number of sources, including surface roughness and ablation, acoustic waves from the surroundings, wind turbulence in flight, and more. Figure 4 shows a diagram highlighting a roadmap describing the mechanisms by which transition can begin.
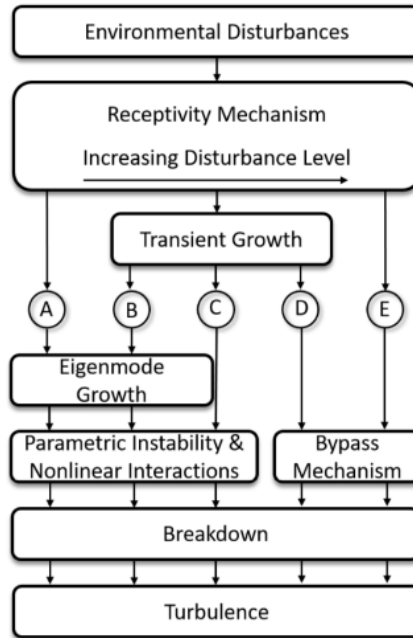
Figure 4: Boundary Layer Transition Roadmap [22]

For boundary layer transition, there exists two main classes of transition. The first comes from the breakdown of laminar flow in the freestream or other substantially large disturbances, known as a bypass. Bypasses cause almost no transition region to occur, and begin an almost instantaneous region of turbulence. Within real world flight regimes, however, this mode of disturbance is uncommon and thus often is not as much of a design concern [23]. This, however, can be a factor when performing ground tests in wind tunnels as it is possible that relatively large amplitude waves can propagate downstream from an otherwise low-fluctuation-energy core flow of a given wind tunnel [24].

The second category of transition mechanisms relate to boundary layer instabilities, caused by modal growth of small disturbances within the boundary layer [25]. In subsonic flow over a flat plate, these disturbances are what give way to the TS waves which grow in accordance to linear stability theory, including the amplification and the growth of

eigenmodes with are defined by the wavenumber of the TS waves. As Mach number increases to the hypersonic regime, higher mode waves supersede TS waves. The three processes by which natural boundary layer instability growth occurs are receptivity, linear stability, and non-linear breakdown. Figure 2 exemplifies the regions in which each of these processes occur. The process of interest to the current work is described primarily by the A path of turbulence transition described in Figure 4, as paths C, D, and E apply to more abrupt mechanisms of generating turbulence. Path B accounts for two non-orthogonal stable modes where a region of algebraic growth can occur, thus leading to span-wise modulations of 2D disturbance waves in the flow [26]. This thesis primarily looks at high-speed laminar incident flow, which due to destabilizing mechanisms naturally grows boundary layer stabilities. Additionally, as will be discussed more in detail in Section 2.6, the high-speed characteristic of the flow stabilizes modes that would otherwise interact in path B. Thus, path A is the most applicable to the problem at hand. This is justified by the assumption of weak freestream disturbances and a large linear growth region compared to that of the nonlinear region (as exemplified in Figure 2). Path A consists of mostly instability waves, which are signals of natural transition such as Mack's instability modes and cross flow instabilities [27].

Morkivin first described the first phase of the transition process, known as receptivity, in 1969 [28]. In this process, naturally occurring disturbances from the freestream (such as acoustic waves) enter the boundary layer. The initial disturbances that enter in the linear region due to receptivity typically are small enough that accurate measurement prior to sufficient growth is difficult [29]. In path A, these initial disturbances are weak and typically occur over a small region on the scale of viscous lengths [26]. Over

these small scales, the subsequent growth or attenuation of these disturbance waves are gradual enough such that a theory of linear growth describes the process. This introduces the linear region where the second phase of the transition process, linear stability, occurs. This approach forms the basis of the field of Linear Stability Theory (LST). Whether these disturbances grow or attenuate in the linear region is often dependent on flow and boundary layer conditions, as well as article geometry and surface roughness [30].

When these disturbances begin to grow to a critical amplitude, then the assumptions described by LST no longer apply and the linear growth now devolves into a non-linear breakdown. This stage of disturbance growth is brief, but then leads directly into full turbulence of the boundary layer, breaking down any remaining 2D laminar flow into fully 3D turbulent flow [27].

The above-described process is also dependent on freestream conditions of the flow. Wind tunnel tests inherently produce more small-scale disturbances that may enter the boundary layer than real world flight tests might expect to produce. This is due primarily to the walls and flow generating equipment of ground test facilities introducing additional thermal and acoustic waves into the freestream that would otherwise not be present [31]. This additional noise influences the process, and subsequent start location, of transition by increasing the amplitude of freestream disturbances which receptivity permits into the boundary layer. Generally, some wind tunnels receive a "quiet" classification if the freestream disturbance levels are sufficiently low. The wind tunnel employed in the current work and described in Section 3.1, does not have a "quiet" tunnel classification.

2.6   Boundary Layer Instabilities at High Speeds

In low-speed incompressible fluids, the dominant instability mode that naturally occurs in boundary layers is often TS waves. This type of flow is conductive to the orderly vorticity patterns expected of TS waves [22]. However, as speeds increase and compressibility effects become important, new instability modes, in addition to TS waves, emerge. This includes higher mode instabilities, as well as an increase in 3D instabilities such as cross flow or centrifugal instabilities [32]. In the inviscid limit, the generation of boundary layers' instabilities is a function of the mean angular momentum of the surrounding fluid. However, cooling the surface relative to the surrounding fluid and increasing the fluid speed stabilizes the TS waves and destabilizes other, higher mode, instability waves [3]. In addition, blunting the nose tip of a cone provides stability to the boundary layer, especially in regions before the entropy swallowing length [33]. The most dominant instability mechanisms are Mack's instability modes, which are instability waves which exist on a discrete spectrum of infinite whole number modes which are present during high Mach number flow [34] [35]. The "mode" of these instability modes derive from the wave numbers of pressure-fluctuation eigenfunctions obtained from LST analysis. From this LST analysis, unstable frequencies can be analyzed to find the dominant instability mechanisms for a given flow condition. The unstable frequency that causes a vorticity wave to reach a critical amplitude thereby triggers transition to occur, while other stable frequencies are attenuated [23].

Disturbances within the boundary layer that generate a transition to turbulence are external waves that, through receptivity, enter and propagate within the boundary layer. Mack's instability modes are instability waves generated from trapped acoustic waves,

which then break down according to frequency and flow conditions to either amplify or attenuate as different mode types within the boundary layer. As specified in LST, the method by which the eigenmodes grow temporally or spatially depends on whether the different components of wave number are complex or real valued. When looking at a specific region where LST applies at a given flow condition, the temporal amplification effect is useful to observe ongoing transition in a given area [3].

The most dominant instability mode present is largely dependent on freestream Mach number, and Figure 5 exemplifies this for the case of a sharp tipped cone. For more blunted cones, the dominant Mack's instability modes shift with bluntness of the cone as the stabilizing effect of the nose tip begins to take effect with larger nose radii. Mack's first mode (Mode 1) is ordinarily the first dominant mode to appear at subsonic and low supersonic regimes. This mode is similar qualitatively to TS waves. In high enough Mach regimes, however, stabilization of this first mode occurs. Higher modes then become dominant and are destabilized. Upon reaching Mach 2, Mack's second mode (Mode 2) becomes the overwhelmingly dominant instability mode, and remains the most dominant for the earlier parts of the hypersonic regime. The second mode is primarily an acoustic wave, although it can spur the onset of additional vorticity waves. Especially in experiments where cooled walls are present, second mode disturbances were observed to be the primary trigger for turbulence transition in the hypersonic regime given path A transition to turbulence [36] [37]. As Mach number increases, however, the other modes also amplify and increase in prevalence within the flow. Experimental results performed by Kendall showed that that second mode instabilities become the dominant mode at Mach numbers of 5.6-7.7, which ultimately culminated in boundary layer transition [6].
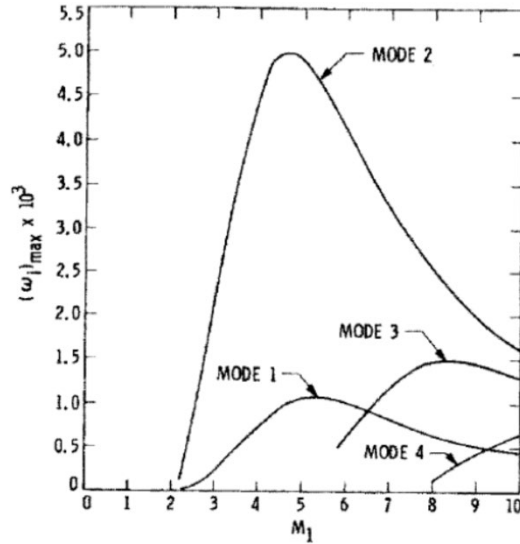
Figure 5: Mach Effect on Max Temporal Amplification Rate for the First Four Modes of 2D Waves [3]

Amplification of higher Mack modes at increased Mach numbers are due to wave reflection interactions within the boundary layer. There exists a sonic line inside the boundary layer where, between the no-slip condition on the stationary body and the hypersonic speeds of the freestream flow, the boundary layer flow must pass the local speed of sound. This is a height above the wall of the flight article where the local speed of sound at and above said line is supersonic relative to mean velocities of the flow [38]. Because of the sharp density gradient created at this point, the sonic line acts as a solid surface guiding acoustic instability waves downstream. This amplifies and traps second mode and higher Mack instability waves beneath this line and, at higher Mach numbers, this sonic line increases amplification of these higher mode waves.

Within the hypersonic regime, some computational models predict a so-called supersonic mode that may be present wherein the disturbances themselves move at supersonic speeds above the given Mach line. These models show that supersonic modes may be more likely to occur for cooled surfaces, which corresponds to a decrease in

boundary layer thickness. With no reflecting surface to trap and amplify these waves, they become Mach-like structures that behave more in line with Mach waves, but share some qualitative characteristics with acoustic waves [39]. However, despite being qualitatively like acoustic waves, predictions show that the amplification rates of these disturbances are much smaller than that of second mode instabilities, and thus more so "travel" along the flight article. However, recent developments hint that these, as well as the second mode reflections off the sonic line and the article wall, may be more nonlinear phenomenon rather than an extension of LST [40]. More research can better quantify and understand the effects of these Mach-like lines on transition. Figure 6 shows an example of how these different reflections with corresponding sonic lines and barriers would interact in a general sense.
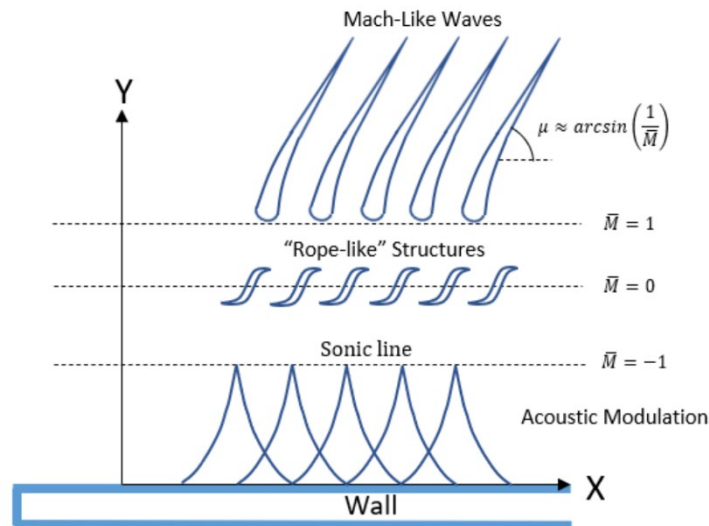
Figure 6: Visual Representation of Second Mode Waves Interacting off Barriers and Sonic Lines [39]

2.7 Cooled Wall Effects on Boundary Layer Transition in Hypersonic Flow

Although there has been many attempts at quantifying the effect of temperature ratio on boundary transition, there has been no experimental consensus on the effect

23

cooled-walls have on the transition to turbulence. As noted by Stetson and Kimmel, *"A reduction in surface temperature has been reported to increase the transition Reynolds number, to have no effect on the transition Reynolds number, or to reduce the transition Reynolds number"* [24]. Throughout the literature available of cooled wall effects on transition, however, researchers employed varying definitions for wall temperature ratio than the previously defined wall-to-boundary layer-edge temperature ratio (T_w/T_e) and wall-to-stagnation temperature ratio (T_w/T_0) used in the current and preceding works. Other temperature ratios employed throughout various literature sources include wall-to-adiabatic temperature ratio (T_w/T_{ad}) and wall-to-recovery temperature ratio (T_w/T_R).

One complication with using edge values is, unlike the sharp-tipped cone, estimation of edge conditions when considering blunted cones use advanced analytical approaches [13]. However, for the sake of comparison to the sharp-tipped cone condition, a Taylor-Maccoll solution for the sharp-tipped roughly approximates the edge conditions in the blunt-nose cases where distances along the cone length are far from the nose tip curvature. This under-predicts the wave angle and subsequent flow values at the edge, producing lower-than-true values for temperature and Reynolds number. For the current work, wall-to-stagnation temperature ratio receives primary focus, with wall-to-boundary layer-edge temperature ratio employed secondarily as a point of comparison to past sharp-tipped cone data. This approximated on the current blunt-nose cone using the equivalent sharp cone geometry as a basis.

Transition prediction and the influence of factors like temperature ratio is a complicated matter of study. This is largely because although for simple shapes, such as cones and flat plates, transition prediction via Mach Number and Reynolds number are

useful approximate measures in lower-speed regimes, using these to fully predict transition at increasing Mach number is limited in accuracy and reliability [41]. This is because the general instability mechanisms are only partially associated with these measures, and outside well studied cases like the cone and flat plate generalizations based on only a few parameters ignore finer nuances in flow conditions [12]. When deviating from well-studied cases, more factors can come into play that add to the complication of transition. Cassel et al. numerically studied the effect of transition and separation on a flat plate but with the introduction of an upward ramp, and found the Mach characteristics within the different sections of the boundary layer (rather than freestream qualities) determined transition and subsequent instabilities [42]. This is because many variations between test set-ups can significantly alter flow conditions, such as noise level in ground test facilities and even heat transfer differences between test articles. When performing cooled wall experiments, this can be a factor in different test environments, especially since some numerical results show that boundary layer receptivity, especially along the leading edge, increases in hypersonic flow [26]. Even the overall spectrum of the flow can change due to factors usch as adjustment of flow temperature. These changes lead to different disturbance frequencies present in the boundary layer, possibly ending in differing experimental conclusions.

Basic LST formulated by Mack predicts that a cooling effect would stabilize the first mode while destabilizing additional higher modes [35]. This is in confirmation of the analytical prediction first offered by Lees in 1946, where analysis of the acceleration of a fluid near the surface of a non-insulated flat plate predicts a stabilizing effect on the boundary layer [4].

Later numerical results supported the claims of Mack and Lees in the case of sharp tipped circular cones. Computations performed by Kara et al simulated cooled wall-to-adiabatic temperature ratios ranging from 0.2-1. They used fifth-order accurate weighted essentially non-oscillatory scheme for discretizing the Navier-Stokes equations. Their results predicted delay in transition location downstream for a 5-degree half-angle sharp cone at a zero-degree angle of attack [43]. They also predicted a reduction in the receptivity coefficient, a measure of the relative amplitude of acoustic disturbances in the boundary layer generated by TS waves. It was observed to be decreased by almost 700-fold as compared to the uncooled case. This supports the notion that the stabilization of TS waves, and the related first mode disturbances, occurs with the introduction of cooled walls as predicted by LST. Federov et al additionally ran a Direct Numerical Simulation (DNS) on a 7-degree half-angle sharp tipped cone and found that cooling the wall produced similar results of a delay in transition and a reduced amplitude in second mode instability waves [44].

Differences in consensus mostly lie in results obtained from experimental work obtained during different research endeavors. Early experiments were the first to notice considerable differences between the expected disturbance stabilizations from theory. Experiments performed in 1957 at the Lewis Flight Propulsion Laboratory in Cleveland, OH by Jack et al. showed that at moderate wall-to-adiabatic temperature ratios (.55-1) for a 9-degree half-angle sharp cone at Mach 3.12 delayed transition. It was noted in the same experiment, however, that further reducing the temperature ratio to between .25-.55 yielded a reversal at which the boundary layer transition came sooner [45]. These results were later confirmed in the same facility with additional experimentation with a 6.75-degree half-

angle cone at Mach 3.8, but lower wall-to-adiabatic temperature ratios revealed an additional two delay reversals at ratios of .46 and .35 [46]. Despite interesting explanations for the possible causes of these trend reversals, the data offered no definitive conclusions at the time as to the reason for these trend reversals. These preliminary results into the effects of cooled-walls on boundary layer transition at high Mach number, however, do not fully represent hypersonic boundary layer transition. Since these experiments occur around Mach 4, the strictly monotonic nature of increasing transition Reynolds number with decreasing wall temperature ratio is expected to break down as more complex interplay between transition factors occurs in the hypersonic regime [47].

Additional later experimental data exist to support that boundary layer transition, in the presence of cooled walls, either experiences delay, experiences early onset, sees a trend reversal, and observes no significant change. As Schneider in his summary of sharp cone transition data noted, when examining the effect of temperature ratios on even just sharp cones, a multitude of contributing factors can have an effect on observations as even the choice of measurement methodology could have an impact on the data [12].

Beyond the initially described results of Jack et al., several more studies came forward to support the notion that trend reversal occurs in hypersonic cones. Stetson and Rushton found in hypersonic wind tunnel tests at Mach 5.5 of an 8 degree half angle cone that there did appear a transition reversal between the wall-to-adiabatic temperature ratios of 0.25-0.58 [48]. The authors also predict the possibility of an additional transition reversal at a temperature ratio of 0.6, but they were unable to test at such value. Mateers, in a study of wall-to-adiabatic temperature ratio on 5 degree and 15 degree total angle blunt nose cones of various radii, found that although a decrease in transition Reynolds number

(early onset), there was present enough data possibly to indicate a trend reversal at a temperature ratio of 0.2 on the larger angle cone [49]. However, there is reason to be cautious with these results, as other researchers have pointed out that the complex factors at play in transition mechanisms do not necessarily combine in a straight-forward manner, as Morkovin warned that rounded tips and cooling, two instances of moving the transition location, do not necessarily work to "double delay" [22]. As these parameters do not necessarily scale with each other or with Mach number, Morkovin states that assuming a delay in two parameters independently do not necessarily culminate to add to disturbance instabilities in such a linear fashion. He notes that cooling in particular is a very sensitive parameter by which transition can be possibly changed on an article, and by adjusting other parameters in addition to wall cooling does not necessarily lead to a an automatic correlation between the combination of parameters and their linear combination of effects.

Delay and a corresponding increase in transition Reynolds number is also a commonly reported result in many more recent hypersonic wind tunnel tests. In experiments performed in the AFRL Ludweig Tube (the same facility that the current work is being conducted) at Mach 6.1 with a sharp tipped 7-degree half-angle cone at zero-degree angle of attack, Embrador, Oddo, and others conducted cooled wall tests at a wall-to-stagnation temperature ratio of about 0.2. Their experiments found both a delay in boundary layer transition, as well as a decreased in boundary layer thickness and an increase in occurrence of second mode instability waves [11]. Additionally, Hameed et al., using Focused Laser Differential Interferometry (FLDI), found for a 5-degree half-angle sharp-tipped cone that transition was delayed accompanied by a thinner boundary layer when the wall-to-boundary layer edge temperature ratio was set to about 2.8 [50]. They

28

were also able to confirm the high frequency peaks of second mode disturbance waves associated with the thinner boundary layer.

Experimental outcomes in some hypersonic tests also report results of early onset and a decreased transition Reynolds number. Stetson et al. performed, as part of a series of stability experiments, measurements focused on the effect of cooled walls on transition on a sharp-tipped 7-degree half-angle cone at Mach 8, cooling to a wall-to-stagnation temperature ratio of 0.42 [5]. They found that while agreeing with others that destabilization of second mode disturbances occurs in cooling, also observed was a decrease in transition Reynolds number. Additionally, Kendall [6] and Demetriades [51], using similar 4-degree half-angle sharp tipped cones both showed an early onset to transition with cooled walls. Kendall performed tests over a range of Mach numbers from 1.6-8.5 with a wall-to-adiabatic temperature ratio of 0.6, while Demetriades had wall-to-stagnation temperature ratios of 0.41 and 0.8. Demetriades also confirmed the amplification of second mode instability frequencies at hypersonic velocities. In an effort to eliminate noise as a possible factor, Blanchard and Selby performed tests in a Mach 6 quiet wind tunnel at NASA Langley Research Center, and overall found agreement with Stetson et al. confirming slightly earlier transition onset and an amplification in second mode instability frequencies [52].

Finally, some published works claim no change in transition Reynolds number occurs due to wall cooling. Sanator et al, using a 5-degree half-angle sharp cone at Mach 10 with wall-to-adiabatic temperature ratios from 0.08-0.4, found no significant change in transition Reynolds number [53]. The authors even questioned whether a substantial correlation between transition Reynolds number and wall temperature existed. Deem and

Murphy found no significant change in transition location on a flat plate at Mach 10.2 for wall-to adiabatic temperature ratios between 0.2 and 0.8 [54]. Additionally, over a wall-to-adiabatic temperature ratio range of 0.4-0.6 at Mach 8.9, Hamilton et al. found no significant change in transition location either [7].

There have been several attempts to reconcile the many different ranges of results obtained by experimental research into boundary layer transition. One possible explanation comes from the fact that freestream properties varying, rather than simply just wall temperature, could play a factor into the various results obtained by different groups, as often stagnation temperature is the factor changed in many experiments to achieve desired temperature ratios, rather than changing wall temperature through cooling [12]. Changes in surface roughness, due to frost build-up or differences in test article manufacturing, may also play a significant factor in the difference in experimental results [55]. Surface roughness is one of the variables that determines not only the path by which turbulence develops, but also determines the boundary layer receptivity as a whole. Especially concerning frost build-up, surface roughness is a variable that can significantly vary between experiments, even in the same facility.

2.8 Nose Geometry Effects on Boundary Layer Transition in Hypersonic Flow

A general result obtained from basic hypersonic aerodynamic theory is that due to flight article curvature, the resulting shock wave generated by the hypersonic body changes angle with respect to the freestream significantly in the area of body curvature. After the area of body curvature, this shock wave then begins to "flatten" to an oblique shock wave. In the change of angle in the shock wave, generates an entropy gradient making an almost

constant thickness entropy layer. The created entropy layer induces vorticity that can interplay with and be absorbed by the boundary layer due to the low angle of the shock wave relative to the surface [20]. The boundary layer encompasses vorticity generated by the entropy layer starting at a swallowing length, and at this point along the flight article that the characteristics of the boundary layer begin to change [56]. Figure 7 shows a diagram displaying the interplay of the entropy layer with the boundary layer. Rotta showed that the length at which swallowing length happens on a body is dependent on Reynolds number and Mach number, as well as the geometrical bluntness of the cone itself [57]. Rotta found, by examining the analytical equations describing swallowing length, that in lower hypersonic regimes, blunter cones had more stable swallowing length locations with increasing Mach number when normalized to Reynolds number. Figure 8 shows these results for a swallowing length parameter, which takes into account freestream unit Reynolds number and the radius of the nose tip as a function of Mach number.
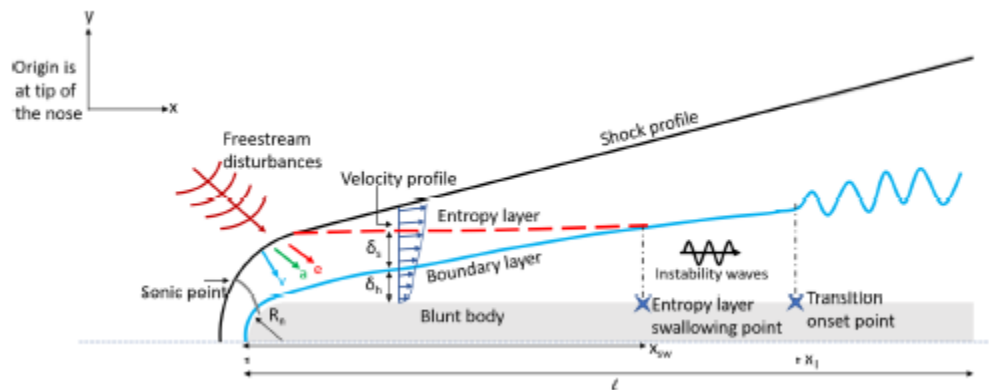
Figure 7: Schematic of the Hypersonic Flow around a Blunt Flat Plate [56]

31
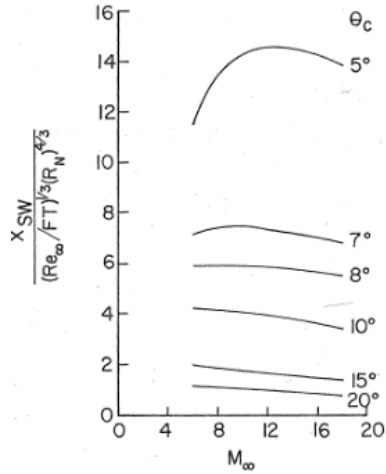
Figure 8: Swallowing Length Parameter as a Function of Freestream Mach Number for Various Total Cone Angles [58]

The interaction of the boundary layer with the entropy layer does create some instabilities that can lead to the onset of turbulence in hypersonic flows, in addition to ordinary second mode waves that can develop. These instabilities also begin to dominate over the second mode instabilities in triggering turbulent transition in the area after swallowing length occurs [33]. A noted feature that can appear to trigger turbulence is an entropy layer-boundary layer interaction visualized by a wisp-like structure that carries along the top of the boundary layer and eventually causes turbulence. This was observed in work performed by Kennedy et al. in the AFRL Mach-6 Ludwieg Tube using a 7-degree half-angle cones of various nose tip radii, noting that these wisps at nose radii of greater than 2.54 mm begin to grow in prevalence dramatically and begin a non-modal path to turbulence transition [59]. Figure 9 shows images displaying these wisp-like structures as observed by Kennedy et al., and observations show these structures grow in size with increasing nose-tip radius. Gossir et al. found that, in realms of increasing Mach number of 10 and higher, these wisp-structures do share similar frequency characteristics to second

32

mode disturbances and may in fact be related, but the influence of these structures on turbulence transition is still unknown [60].

A point where there seems to be consensus experimentally and analytically regarding the effect of nose bluntness is on the transition location. On a theoretical level, study of the Parabolized Navier-Stokes Equations along with LST predict that for small bluntness transition Reynolds number increases on cones (and generalized to flat plates as well) up to a critical nose radius beyond which a transition reversal occurs and transition Reynolds number decreases [61]. These predictions matched with predictions found experimentally with cones with nose bluntness. Bluntness increases transition Reynolds number, as well as increasing boundary layer thickness compared to the sharp cone case [62]. In addition, the location of this transition point was experimentally confirmed to be highly dependent on freestream Mach number, and at a given flow condition there exists an optimal nose radius for which the transition Reynolds number was furthest downstream before transition reversal was apparent [63]. Transition reversal due to nose radius, however, is a non-linear phenomenon not directly related to other conditions that normally define transition, such as second mode amplification [33].

(a) Enhanced image for 0.508 mm nosetip-radius configuration condition A

(b) Enhanced image for 1.524 mm nosetip-radius configuration condition B

(c) Enhanced image for 2.54 mm nosetip-radius configuration condition C

(d) Enhanced image for 5.08 mm nosetip-radius configuration condition D
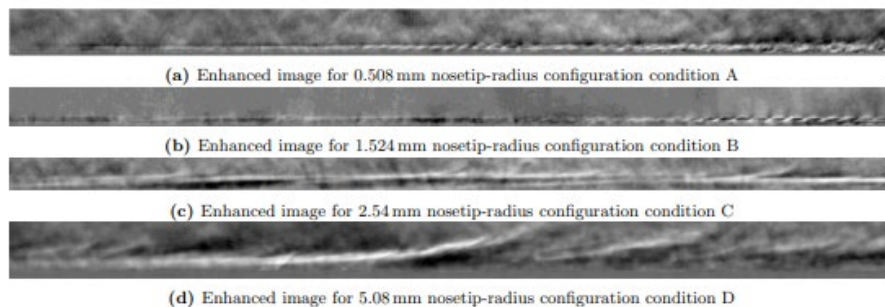
Figure 9: Schlieren Images of Observed Wisp-Structures with Increasing Nose Radii [59]

One area that is still open in investigation with a lack of complete understanding is the effect on boundary layer receptivity and disturbance wave amplification in blunt nose cones. There has been numerical simulation work performed by Zhang et al. that tests on a blunt flat plate at Mach 6, finding that slower moving acoustic disturbances did not enter the boundary layer at all when compared to the sharp tipped case, but faster moving disturbances experienced a much larger amplification [64]. Other numerical work performed by Malik et al. predicts a stabilizing effect on the higher frequency disturbances on blunted tipped cones as compared to sharp tipped cones, while enlarging the overall receptivity and band of frequencies accepted into the boundary layer [61].

Experimentally, the effect of nose bluntness on the disturbances within the boundary layer is still an open question. There has been experimental work on blunt nose cones performed by Zhong et al., which claims to have found not significant evidence of first or second mode disturbances within the early stages of the boundary layer prior to the swallowing length [65]. Prior to the swallowing length, since Mack instability waves can still exist, generation of first and second mode instabilities is still possible. There is, with the introduction of a blunt nose, an introduction of the role of entropy in generating and amplifying existing first and second mode instabilities. Stetson noted, however, that these modal amplifications occur much later than the onset of turbulent transition generally [62]. Numerical results presented by Federov and Turner showed that, though second mode disturbances may be dampened prior to the swallowing length, entropy generated disturbances are not enough to trigger transition [66]. However, Maslov later presented experimental evidence showing the damping of second mode disturbances in a 7-degree half-angle cone [67]. In fact, Jagde et al later showed it difficult to differentiate a dominant

34

mode between second mode and entropy instabilities as the core-destabilizing factor in transition [68].

2.9   Boundary Layer Transition Calculation Using Schlieren Imaging

Schlieren imaging is a process which collimated light captures planar density gradients of flow due to the differing indexes of refraction in the fluid. Since density is a factor that changes both along and normal to a surface within a boundary layer as it transitions, flow and turbulence information within the boundary layer can be determined with sufficient resolution and frame rate of the receiving camera. Casper et al. in a 2013 study validated a foundational algorithm to track transition-comparing Schlieren to other determinative methods [69]. In this study, a 7-degree half-angle cone at zero-degree angle of attack was examined using Schlieren imaging, pressure transducers, and thermocouples at the Sandia National Laboratories Hypersonic Wind Tunnel (HWT) (generally considered a noisy tunnel) and the Boeing/AFOSR Mach-6 Quiet Tunnel (BAM6QT). Using these instruments, instability curves, instability frequencies, and convective velocities within the boundary layer were calculated and used to determine transition location.

The various methods in the Sandia-based study tended to agree on where fully turbulent flow occurred. It was additionally found that the visual data provided by Schlieren was overall the most conservative of the methods, but was still in rough agreement with the results of the thermocouple method and one of the applied pressure transducers, presenting that Schlieren was a reasonable method by which transition could be determined in reference to other methods examined. This highly useful and non-

intrusive approach to determining boundary layer transition was adopted in experimental work performed by Embrador and Oddo, and was additionally used in the work presented in this thesis [11]. Figure 10 shows the overall transition location results, and Chapter 3 presents further discussion on the implementation of this method in the current experimental set-up.
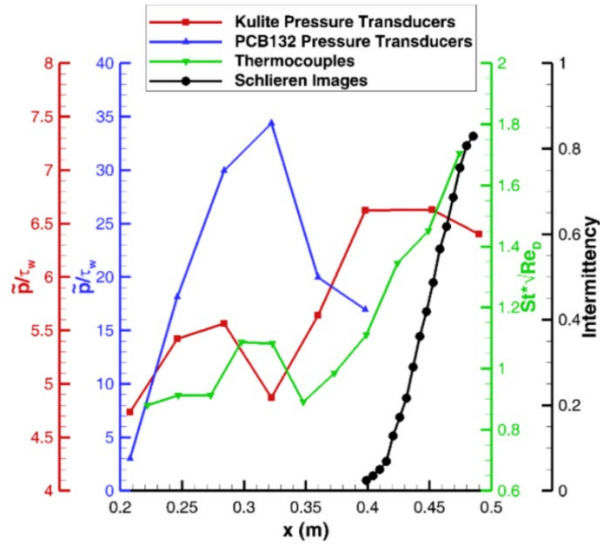
Figure 10: Comparison of Transition Location using Various Measurement Methods at HWT using a Re$_\infty$ near 7x10^6/m [69]

2.10 Boundary Layer Instability Calculations Using the Fast Fourier Transformation

To obtain quantitative data about boundary layer instabilities from the visually represented data provided from the Schlieren images obtained, an application of a spatial Fourier transform extracts velocity data from the observed density gradients. Jagde et al. describes in their work a method to obtain the quantitative data of a wave packet within a forming boundary layer instability, such as the dominant frequency [70]. To accomplish

this, they employed a high frequency (30-40 ns) pulse diode laser along with a high-speed camera set at a frame rate of one-half the estimated second mode fundamental frequency. An experimental set-up can substitute the high-frequency pulse diode laser with a lamp light source with sufficient power for adequate lighting with no significant effect on the results. This enables high-frame rates and short exposure times and to allow maximum light intensity to be observed in the Schlieren set-up.

With the height of the image from physical units to pixels correlated, a cross correlation was performed between frames to determine the velocity of the second mode waves. A spatial fast Fourier transform (FFT) applied to the data output boundary layer thickness and second mode wave-propagation speed and wave number. Dominant frequency can then be determined from the product of the propagation speed and the wave number.

III. Methodology

Literature as to previous investigations on the effect of surface temperature on cones either use cones of multiple pieces or change the freestream conditions to change temperature ratio [12]. Past work performed by Oddo and Embrador examined the effect of surface temperature on boundary layer transition on a sharped-tipped cone using single-piece cones and internal cooling to affect temperature ratios. The current work attempts to replicate the methodology presented by Embrador, but apply the process to a blunt-nose cone geometry.

3.1 Facility

The experimental work for this thesis took place at the AFRL Mach-6 Ludwieg Tube Wind Tunnel at Wright-Patterson Air Force Base in Ohio. A Ludwieg tube wind tunnel operates by pumping air into an initial high-stagnation pressure chamber connected to a driver tube. This driver tube can hold pressures ranging from 50-580 psia and maintains a temperature of 505 K. An actuator connected to a fast acting valve separates the initial high-pressure region from the initially evacuated test section prior to testing. At the AFRL Mach-6 Ludwieg Tube, reduction of test section pressure to 0.02 psia or lower is required prior to testing. After achieving adequate pressures in the driver tube, the actuator receives the control signal to begin the test thereby retracting the valve flowing air through a converging-diverging nozzle into the test section. The converging-diverging nozzle set-up into the test section guarantees the test section experiences the desired hypersonic flow condition of Mach 6.1. This flow condition exists on the scale of a quarter of a second. Quasi-steady state (QS) flow periods develop in the tunnel due to the development of

unsteady expansion waves [71]. In the AFRL Ludwieg Tube, two such periods typically develop during a run. Figure 11 presents a diagram of the AFRL Ludwieg Tube rendered using Computer Aided Design (CAD) software.
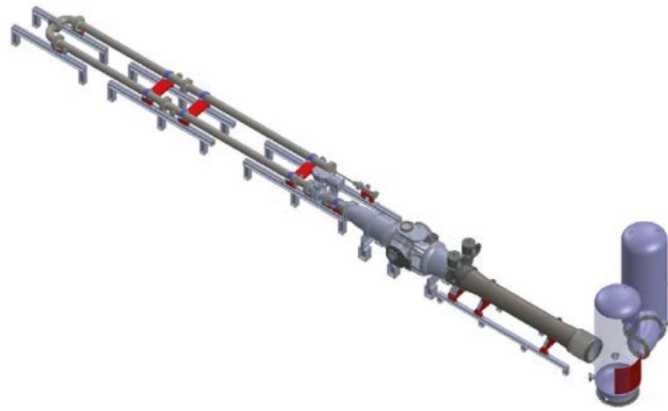
Figure 11: CAD Rendering of the AFRL Mach-6 Ludwieg Tube [71]

3.1.1 Facility Design

The AFRL Ludwieg tube is a closed air system wind tunnel. This offers the advantage of having greater control over the conditions of the air used in the test, such as reducing the water vapor content in experimental trials. This is important because in the cooled-cone experiments significant frost build up can influence the surface roughness of the model and trigger turbulence unnecessarily. To address this problem, air dryers are installed at the two 27 HP intake compressors such that the circulating air has a water vapor content of less than 20 parts per million (ppm). Oddo encountered the problem of water content in the circulated air during initial experimental work [9], but the solution was present before Embrador began tests [10].

Upon exiting the intake compressor, a commercial 18 kW resistance heats the air to 505 K. Upon achieving a desired stagnation pressure within the driver tube, a bypass

valve shuts off flow from the intake compressors. The desired stagnation pressure ordinarily takes between five to twelve minutes between runs to achieve, and during this period two 25 HP Leybold vacuum pumps work to bring the test section pressure toward 0.02 psia or less. The system automatically maintains desired initial conditions during any additional time in which the driver tube spent otherwise idle. Excess idle time between runs can cause driver tube pressures to be lower (due to leaks) or higher (due to continuous running of the compressor) than would otherwise be the desired pressure condition.

The driver tube is made of 304 stainless steel constructed from two 35 ft sections connected by a 180° bend with an inner diameter on 9.75 inches. The driver tube allows for two QS periods of uniform flow that last about 100 ms each. A fast-valve actuator connects the driver tube to the test section, which allows for the quick turnaround times between successive runs.

A three-part converging-diverging nozzle assembly guarantees the desired Mach-6.1 flow condition in the test section. The assembly consists of a 3.71-inch diameter throat made of 316 stainless steel and two entrance/exit sections made of 6061-T6 aluminum. The total length of the nozzle is 117 inches and has an exit diameter of 50 inches that connects to the test section. The test section, similarly, consists of three circular hatch segments with 12-inch fused silica windows on either side of the tunnel to allow viewing and/or the collection of visual data from the tunnel during runs. A pneumatically operated closed hatch grants access to the test section. It is bolted shut prior to bringing the test section down to vacuum. A converging-diverging diffuser follows the test section, comprised of three sections: a 6° converging inlet, a straight section, and a 4° diverging outlet.

Beyond initial warm up and shut down procedures that require manual operation of Ludwieg tube machinery, programmable logic controllers located in the Ludwieg tube control room perform tunnel operations such as setting driver tube pressures. These work through a LabVIEW UI, which allows for connection, control, and regulation of tunnel instruments through Ethernet connection. These also can report and monitor pressure conditions in various areas of the tunnel, most notably within the driver tube and test section, through pressure transducers that interfere minimally with standard operation.

3.1.2   Calculating Flow Conditions

Past experiments in the AFRL Ludwieg tube have confirmed various properties of the tunnel and the quality of flow that is to be expected. Tunnel qualification efforts performed by Labuda et al. have confirmed that the tunnel achieves Mach 6.1 for approximately 200 ms in the presence of a cone like test article [72]. The initial testing of the tunnel confirmed maintenance of nominal Mach 6 flow throughout the test section with about 2.3% standard deviation, and maintaining uniform flow to within 1% deviation [71].

Two QS periods share the Mach 6.1 flow condition during tunnel operation. A short period of high turbulence caused by expansion waves reflecting off the walls of the test section separates these periods. Pressure transducer performs pressure measurements at the beginning of the nozzle connecting the driver tube to the test section. Time-series data in which the stagnation pressure measured by this transducer remains constant is one quantitative way of visualizing these QS periods. During initial characterization of the tunnel, the drop in total pressure during the QS periods along the test section was less than 0.2% [71]. Figure 12 shows an example of this stagnation pressure data from a performed run during testing for the current work. As can be seen from the data, associated with these

constant pressure periods is a drop in stagnation pressure relative to the initial driver tube pressure. This pressure drop during each QS state associated with tunnel and shock losses. Previous tunnel characteristic quantifying efforts have placed estimates of the stagnation pressure during QS state 1 (QS1) and QS state 2 (QS2) to be 87% and 67% respectively [71]. Relative stability of the stagnation pressure during these QS periods allows for the derivation of reliable freestream unit Reynolds numbers during these cases.
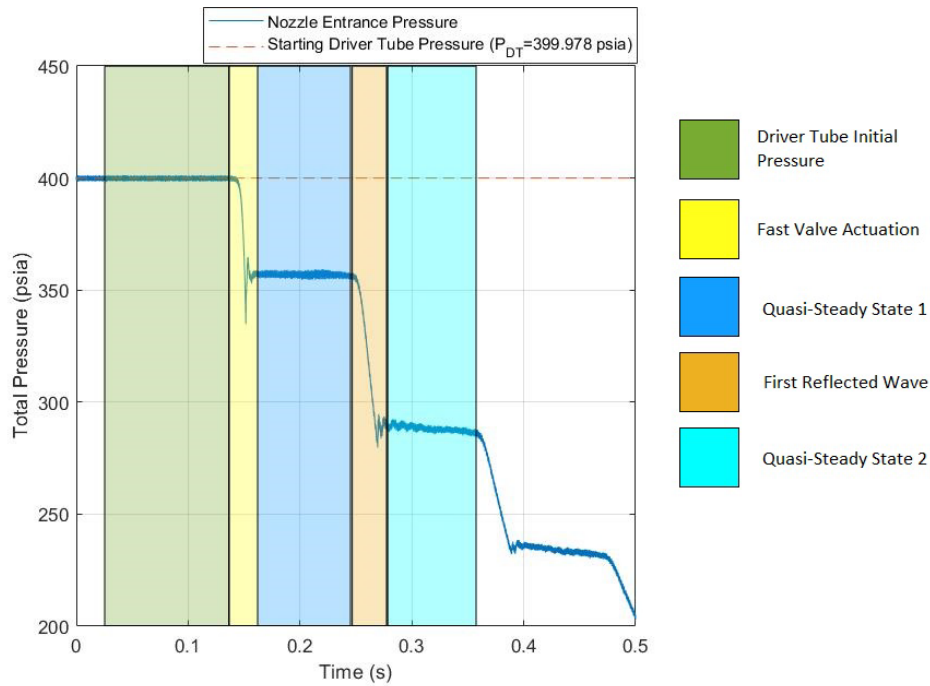
Figure 12: Stagnation Pressure Reading for a Minimal 400 psi Run (Run 13)

Assumptions made within the following calculations is that the air in question is an ideal, calorically perfect gas with a specific heat ratio of 1.4. Additionally, using the experimental values found in the tunnel characterization work (a Mach number of 6.1, the driver tube pressure, driver tube temperature, and stagnation pressures 87% and 67% of the driver tube pressure), various freestream flow conditions can be found for each QS state.

Using the isentropic relations with the given info, stagnation temperature within the test section, neglecting viscous effects, is:

$$T_0 = T_{DT} \left(\frac{P_0}{P_{DT}} \right)^{\frac{\gamma-1}{\gamma}} \tag{3}$$

where T_0 is the stagnation temperature at the current state, P_0 is the stagnation pressure at the current state, P_{DT} is the driver tube pressure, and T_{DT} is the driver tube temperature. Speed of sound measurements during initial tunnel characterization found that in the test section, stagnation temperature was around 486 K after a linear fit of the data in QS 1 [71].

The stagnation density (ρ_0) can be determined with:

$$\rho_0 = \frac{P_0}{RT_0} \tag{4}$$

R is the specific gas constant for air, 287.06 J/(kg K). Then, the freestream temperature is:

$$T_\infty = T_0 \left(1 + \frac{\gamma-1}{2} M_\infty^2 \right)^{-1} \tag{5}$$

In addition, the freestream density (ρ_∞) is:

$$\rho_\infty = \rho_0 \left(1 + \frac{\gamma-1}{2} M_\infty^2 \right)^{\frac{-1}{\gamma-1}} \tag{6}$$

Next, the freestream velocity is:

$$U_\infty = M_\infty \sqrt{\gamma R T_\infty} \tag{7}$$

Equations (3)-(7) lead to the terms necessary to calculate the freestream Reynolds number as described in Equation (1). However, two terms from that equation are still unknown. Dividing out the position term (x) presents it it as a freestream unit Reynolds number (Re_∞/L). Mack presented an experimentally derived relationship for the freestream viscosity term, μ_∞, in terms of the freestream temperature as follows [3]:

$$\mu_\infty * 10^5 = 1.458 \frac{T_\infty^{\frac{3}{2}}}{T_\infty + 110.4}, \quad T \geq 110.4\ K \tag{8}$$

$$\mu_\infty * 10^5 = .0693873 * T_\infty, \quad T < 110.4\ K \tag{9}$$

According to cooled-model temperature data discussed in detail in Section 3.4, 82.5 K was the coldest surface temperature and 127.4 K was the warmest surface temperature during the cooled condition. Performing nominal flow conditions using Equation (8) appeared to match best the freestream temperature conditions. Table 1 shows these nominal flow conditions for each of the desired driver tube pressures to run.

Table 1: Nominal Flow conditions for Mach 6.1 flow in the AFRL Ludwieg Tube, T_{DT}=505 K

P_{DT} (psia [MPa])	QS Period	P_0 (psia [MPa])	T_0 (K)	U_∞ (m/s)	T_∞ (K)	μ_∞ (kg/m*s)	Re_∞/L (1/m)
50 [.34]	1	43 [0.296]	480.5	923	56.92	3.74×10^{-6}	2.55×10^6
50 [.34]	2	33 [0.228]	445.9	889	52.82	3.43×10^{-6}	2.23×10^6
100 [.69]	1	87 [0.600]	480.5	923	56.92	3.74×10^{-6}	5.18×10^6
100 [.69]	2	67 [0.462]	445.9	889	52.82	3.43×10^{-6}	4.52×10^6
150 [1.03]	1	130 [0.896]	480.5	923	56.92	3.74×10^{-6}	7.74×10^6
150 [1.03]	2	100 [0.690]	445.9	889	52.82	3.43×10^{-6}	6.75×10^6
200 [1.38]	1	174 [1.201]	480.5	923	56.92	3.74×10^{-6}	1.04×10^7
200 [1.38]	2	135 [0.925]	445.9	889	52.82	3.43×10^{-6}	9.04×10^6
300 [2.07]	1	261 [1.801]	480.5	923	56.92	3.74×10^{-6}	1.55×10^7
300 [2.07]	2	201 [1.387]	445.9	889	52.82	3.43×10^{-6}	1.36×10^7
400 [2.76]	1	348 [2.401]	480.5	923	56.92	3.74×10^{-6}	2.07×10^7
400 [2.76]	2	268 [1.849]	445.9	889	52.82	3.43×10^{-6}	1.81×10^7
500 [3.45]	1	435 [3.002]	480.5	923	56.92	3.74×10^{-6}	2.59×10^7
500 [3.45]	2	335 [2.312]	445.9	889	52.82	3.43×10^{-6}	2.26×10^7

3.2 Test Article

All experiments in the current work implemented a 303 Stainless steel 7° half-angle cone with a 1.5 mm radius at the spherically blunted nose tip. Figure 13 shows a detailed engineering drawing of the cone. The cone itself consists of two main parts: the base and

the cone section. The design of the cone was such that the area cooled and examined under test conditions was of one solid piece, as to eliminate possible thermal expansion differences from triggering transition to turbulence early. The main geometry of this cone was based on a test article previously employed in experiments performed by Oddo and Embrador, but with an increase in nose tip radius from 0.1 mm to 1.5 mm [9] [10]. The cone included a hollow step-like cavity, which allowed liquid nitrogen (LN2) to cool the model to desired temperatures during cooled runs. The cone is 23.6 inches (in) in length and has a base diameter of 5.9 in.

a)
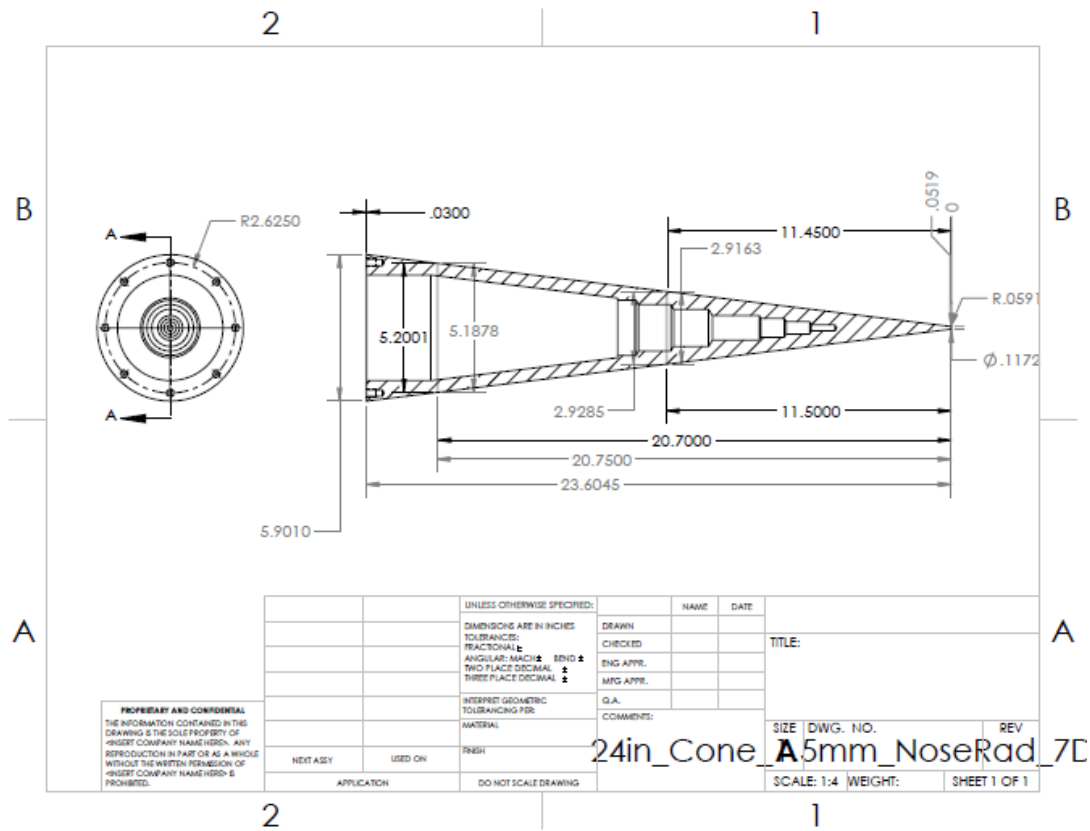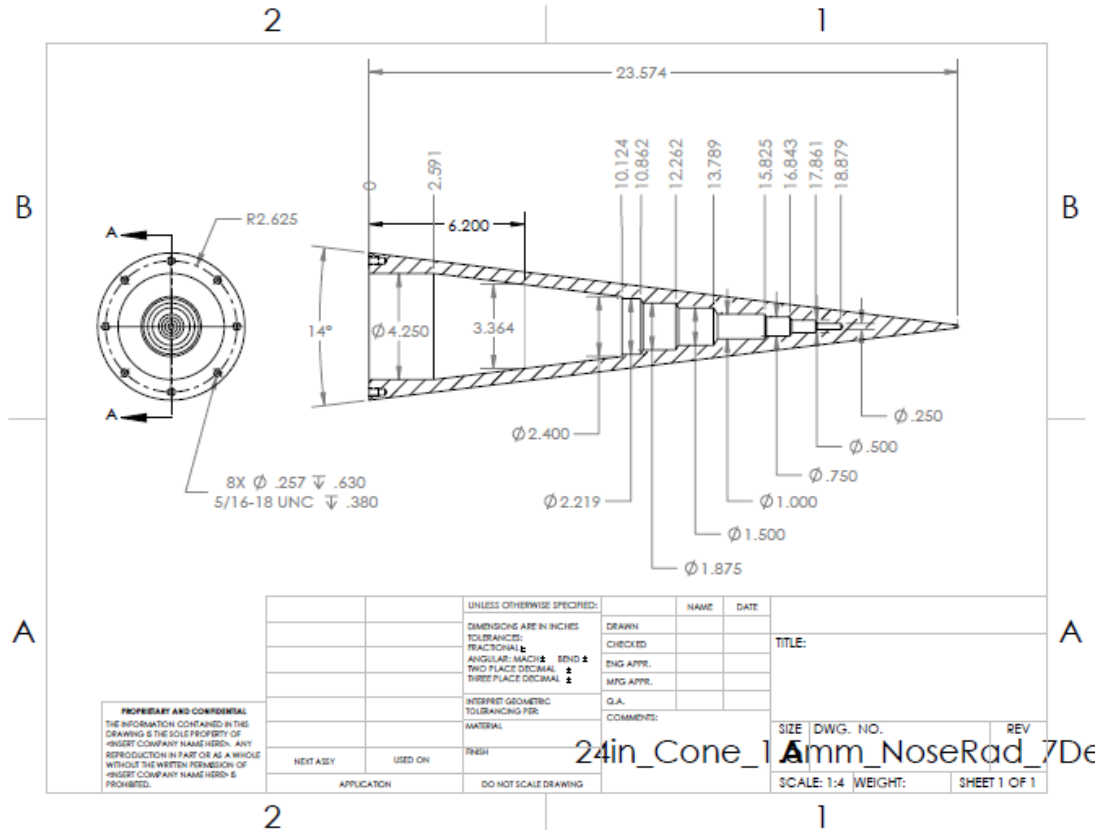
Figure 13: Engineering Drawing of the Spherically Blunted Cone Employed for All Runs, a) Outer Measurements and b) Inner Chamber Measurements

The base attaches to the cone to provide a mounting mechanism to the Ludwieg tube test sting and to provide a seal between the external environment and the internal cavity. The base secures to the sting by tightening four threaded quad bolts with around the sting that prevented horizontal movement of the model. The base contains three one-fourth inch threaded NPT holes. Two of these holes connect to an insulated LN2 transfer NPT-threaded ports, which are a part of the cryogenic cooling system described in more detail in Section 3.3. The remaining threaded port seals with a 90 psi rated pressure relief valve, which serves to prevent LN2 over pressurization during runs. The base attaches to the cone

46

using eight 18-8 5/16-inch high strength stainless steel screws outfitted with cryogenic rated O-rings to prevent leakage. Appendix A shows a full outline of the parts used to assemble the model into the Ludwieg tube sting. Additionally, Appendix A presents reports of the average roughness profile across both the current cone model, as well as the model employed by both Oddo and Embrador. A portable roughness tester measured average roughness at 1-inch intervals measured from the tip. The tester examined the roughness over a half-inch stretch of the cone length, measuring the arithmetic mean average roughness of the surface of the cone. The average roughness of the cone across the entire length is about 21 µin. Figure 14 shows a photo of the spherically blunted nose tip cone fully mounted without the cryogenic system attached.
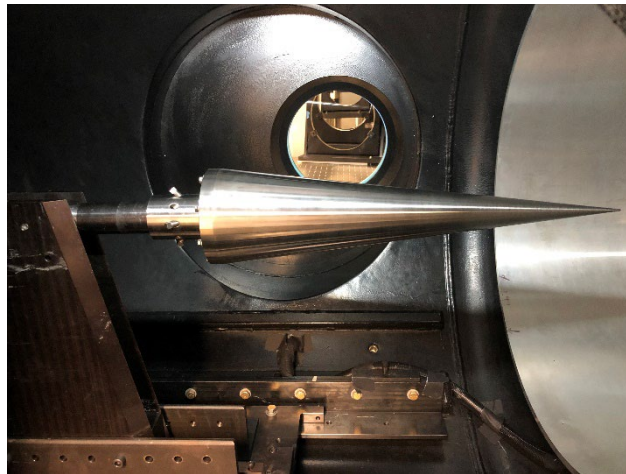

Figure 14: Spherically Blunted Test Article Mounted on the Sting of the AFRL Ludwieg Tube

3.3   Cooling System

For the cooled runs, LN2 flowed into the cone internal cavity using a cryogenic cooling hose system. The hose system then circulated the LN2 flow to exhaust into the open environment as gaseous nitrogen. The system employed was adapted from that

employed during Embrador's work. The system begins with a 120 liter (L) cryogenic dewar containing LN2. The dewar maintains a nominal pressure of 22 psi. Figure 15(a) shows the dewar just after obtaining the cone temperature profile. Extending out from the Dewar "liquid" line is a 6 foot, non-insulated connector line. That line connects to a 14-foot insulated transfer hose that feeds to ports located at the bottom of the test section. Figure 15(b) shows this connection. All hose and line connections have cryogenically ratings, and Appendix B shows a full list of individual components used in the cryogenic system, as well as systems schematics. For Runs 36-52, the initial chosen spot for the intake connector was the location shown in Figure 15(b). Due to space limitations and safety, the intake connector's location changed to a test section port further upstream for runs 53 and onward.

a)   b)

Figure 15: Post Run 44, a) Cryogenic Dewar Attached to Cryogenic Hose system, b) Transfer Line Connector into the Tunnel Test Section

Inside the test section, two additional 6-foot insulated hoses connected the outside intake and exhaust hoses to the model to allow circulation throughout the model. Stainless steel clamping mechanisms and braces secured the lines inside the tunnel to the Ludwieg tube sting and prevented damage. Aluminum support brackets additionally secured the lines to the test section. Attaching a combination of metal and plastic zip-ties to available

holes within the wind tunnel helped address additional slack in the lines for safety of operation. When possible, metal zip-ties always accompanied plastic zip-ties to provide extra rigidity and security to the lines, as Oddo observed plastic zip-ties alone to fail around driver tube pressures of 300 psi or greater [9]. Figure 16 shows the final set-up of these mounts to the model intake and exhaust valves.
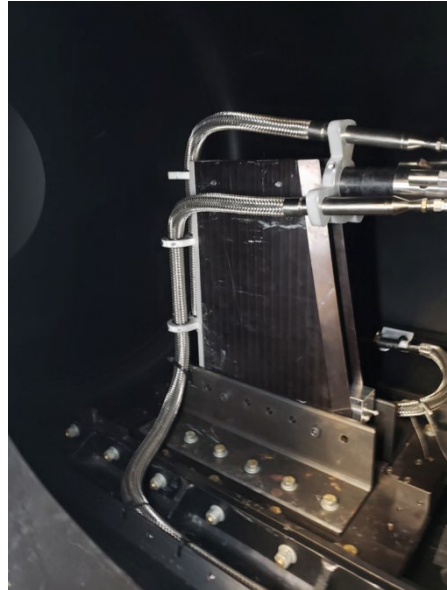
Figure 16: Typical Mounting and Clamp Set-Up for the Model

The 6-foot intake and exhaust lines connect to the model via cryogenic rated fittings. After circulating LN2 into the model via the line pictured to the side in Figure 16, it flows out through the exhaust line at the top. This is to ensure that, due to gravity, the LN2 sufficiently fills the internal cavity of the model during testing. That line exits out a test section port on the opposite side and the exhaust ventilates through a 75-foot uninsulated hose to the open atmosphere. By this point, the LN2 has evaporated into gaseous nitrogen.

3.4 Cooling Process

Current tests examined the effectiveness of cooling processes adapted from Oddo and Embrador to gain an insight into the cooling process and the resulting temperature profile of the new model. Appendix C presents the outcomes for cooling and defrost of the sharp tipped cone employed in testing performed by Oddo and Embrador. Oddo's results use two temperature silicon diodes to track the time to reach thermal equilibrium and the minimum temperature at those points. Embrador expanded on the measurements by applying six diodes instead of two in order to obtain a more complete picture.
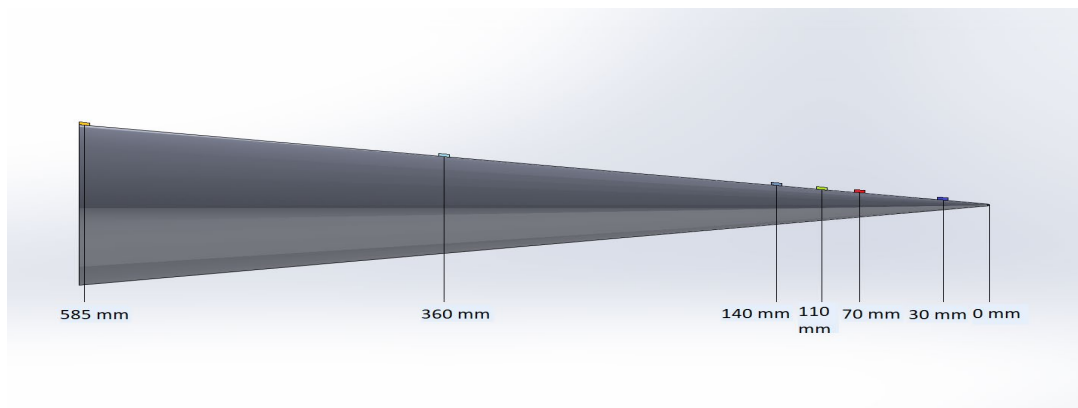
Figure 17: Sensor Positions for the Cooling Test

Placing the six silicon thermal diodes at distances similar to that described by Embrador, the temperature data captures both the cavity region and solid material region of the model with three diodes per region. Apiezon-N cryogenic grease and PTFE tape attached the Lakeshore DT-670B1 diodes to the model. The cryogenic grease serves to ensure sufficient thermal contact with the surface. Figure 17 shows the placed location of each diode, with distances measured along the central axis of the cone. The diodes themselves were rectangular with two leads, measuring 3.18 mm long, 1.91 mm wide, and 1.08 mm tall.

The thermal diode output wires fed through 8-hole Connax fittings and connected to three output ports on the wind tunnel test section. These wires connected through female-to-male wire connectors to output port wires on a Lakeshore 2181 218-8 output temperature monitor. Data recording took place via security camera to obtain results throughout the test at 5-minute intervals.

After closing the test section, reducing the pressured in the test section to 0.02 psia or less prior to LN2 flow prevented frost formation from being a significant factor in cooling. This also reduces cooling time by limiting the amount warm air convection possibly affecting the cooling process. This precaution repeats prior to LN2 cool down during runs, along with an initial "dummy run" to remove additional water vapor from the tunnels circulated air. During this process, a visual confirmation of minimal frost build-up confirmed frost was not a significant factor during runs. Figure 18 shows an example of this type of minimal sheen observed. As additional safety precautions, oxygen monitors were placed both at the entrance of the tunnel room and next to the LN2 dewar itself to check for sudden drops in oxygen levels that could be indicative of leaks along the cooling system.

After donning appropriate personal protective equipment (PPE) for handling cryogenic storage containers, the schedule defined in Table 2 defined the gradual opening of the dewar to full LN2 flow as to prevent the formation of crystals within the lines. At the end of this schedule, flow continued until the change in temperature profile was negligible on all measured portions of the model. Figure 19 shows the temperature measured by the diodes across time of the experiment. As can be seen, the final time it takes to reach equilibrium is about 100 minutes.

Table 2: Liquid Flow Valve Turning Schedule

Initial opening procedure	
time (mins)	turn valve (deg)
1	20
4	180
5	180
12	360
15	360
21	360
25	360 (full flow)
95 mins	start runs

Figure 18: Light Frost Sheen on Model during Tunnel Operations at Vacuum conditions

From the results, when thermal equilibrium is achieved the temperature distribution along the surface of the blunted cone may be documented. While the open cavity section diodes (diodes 4-6) all seem to converge around the minimum of 82.5 K, the diodes that cover the solid body section of the model seem to diverge a bit, with diode 1 having a thermal equilibrium temperature of 127.4 K. While temperature measurements experience some deviations because of the effects of thermal conduction and radiation, it does present difficulties when attempting to take the system as a single wall temperature to obtain an

overall cooled wall-to-stagnation temperature ratio. Since it is observed that a majority of the data points (diodes 3-6) do more converge to a singular value, their median minimum values is taken as the wall temperature condition for the cooled runs, that being about 85 K. There exists a small difference between the values found with the current series of thermal tests and the results presented by the same thermal tests done by both Embrador and Oddo, as seen in Appendix C. Overall, there exists agreement between the temperature conditions of both models.
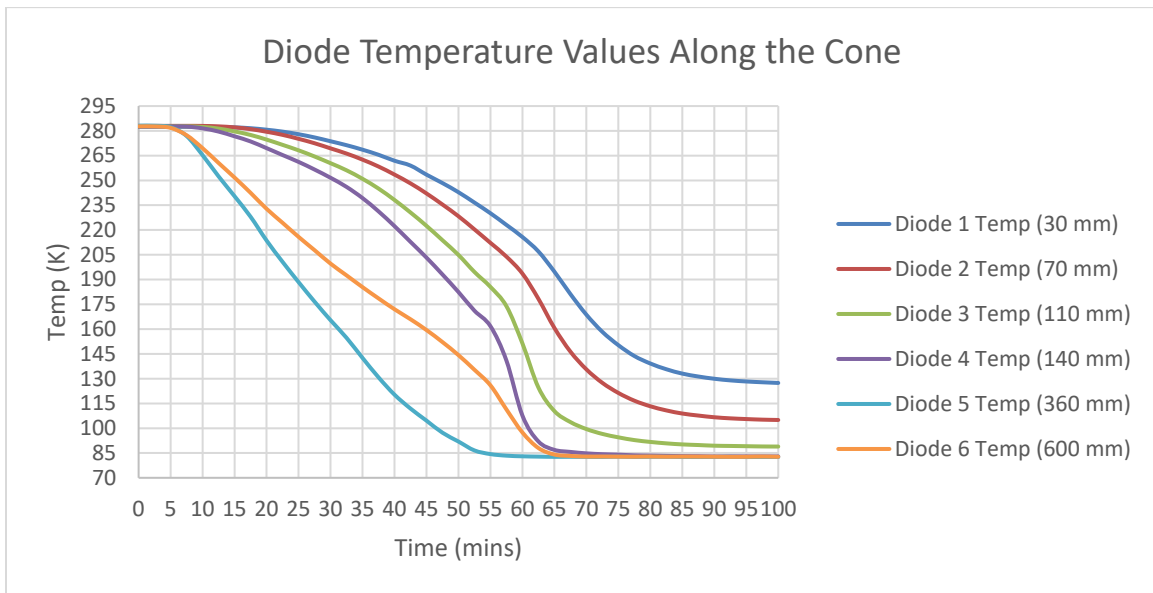
Figure 19: Results of Cooling Test. Listed Distances are Measured using Tape Measure Along the Horizontal from Cone Tip Edge (±5 mm)

With initial confirmation that this procedure reached desired cooled-wall conditions, each day began with the same initial cooling procedures outlined in the initial temperature profile test. After performing the entire procedure, a day's cooled runs could commence after turning off LN2 flow. After a given run, opening the LN2 liquid valve allowed the LN2 flow to restore thermal equilibrium from any energy addition the

hypersonic flow might have added during the run. This process consisted of a 30-minute period in between runs to re-cool the model and shut-off LN2 flow before another run was attempted. Precedent of previous LN2 work in the Ludwieg tube determined that a 30-minute period would be sufficient to cool the model. These periods also allowed an opportunity to confirm visually minimal frost build-up on the model in-between runs.

3.5 High-Speed Schlieren

All runs in this thesis obtain boundary layer and turbulence information from visual data collected from a Schlieren visualization set up. Density gradients in the flow locally alter the index of refraction. These local changes in refraction indexes bend or block otherwise parallel beams of light to give a planar view of how these density gradients change across a viewing section. Since density in a compressible fluid relates to both local velocity, pressure, and temperature conditions in a fluid, this parallel light visualizes changes in the flow across an area.
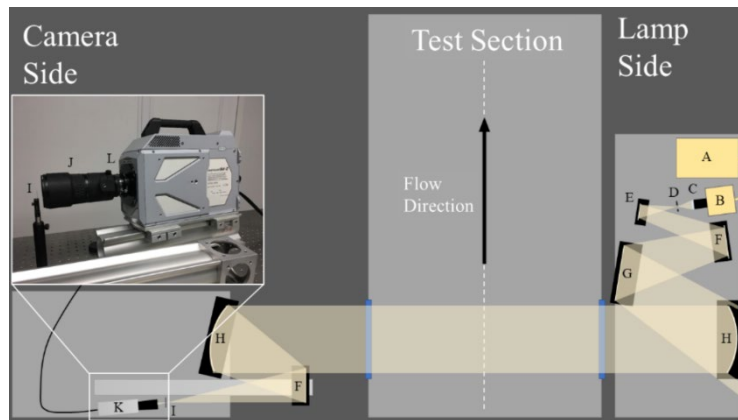

Figure 20: Approximate Diagram of Schlieren Set-up [9]

The experimental set-up utilizes a Schlieren set-up first established by Oddo and Embrador [9] [10]. Figure 20 shows the experimental Schlieren set-up. The Schlieren

system consists of three main parts: the main light source, the reflecting initial set up on the lamp side, and a reflecting refocusing set up on the camera side. A Newport 66921 Arc Lamp capable of up to 1000 W acts as the initial light source. That light projects through a focusing lens and reflects across several convex mirrors to collimate the light across the test section. On the other side of the test section, the collimated light reflects off parabolic mirrors and refocuses over a part of a razor's edge and into a camera for data recording. The razor's edge is at the focal point between the final mirror and the camera, which acts as a filter better distinguishing the new gradients from background light by dimming the entire image without obstructing it.

Table 3: Schlieren Set-up Components [9]

Component	Description
A	Oriel OPS-A1000 Arc Lamp Supply
B	Newport 66921 Arc Lamp, 1000W
C	BK7 A Coated Plano Convex Lens, 2" Diameter, F=150 mm
D	Circular Aperature, 2.5" Diameter
E	Planar Mirror, 3" Diameter
F	Planar Mirror, 6" Diameter
G	Planar Mirror, 10" Diameter
H	Concave Mirror, 12" Diameter, Parabolic, F=75"
I	Razor Blade and Holder, 2.4375" length
J	Camera Lens, Nikon Nikkor 80-200mm 1:2.8D
K	Photron Fastcam SA-Z-2100K-M
L	2K Zoom Tleconverter, Nikon

Table 3 describes in detail each component listed in Figure 20. The initial light source was a Newport 66921 Arc Lamp powered by an OPS A1000 Arc Lamp Power Supply set to an output wattage of 650 W. This was well below the full capability of the Arc Lamp that had a rated maximum of 1000 W. A plano-convex (PCX) lens focuses the light onto a circular aperture in order to limit the light passing through to a small diameter

of about .2 inches. This provides greater clarity to the images, as focus to the light source increases the sensitivity of the overall Schlieren system [73]. Three flat mirrors expand and collimate the light across the fully allowed window and too meet the focal distance limitation of the concave mirror, that being 75 inches. Each mirror was progressively larger than the last to capture as much light as possible due to spreading. Short distances between these mirrors minimized reflection angle and possible errors relating to such. This also helps to maintain the uniformity of the light throughout the process, as distortion tends to increase the more distance the light must travel.

The light then projects to fill a concave mirror that collimates the light over the test section through the 12-inch viewing mirrors. On the other side of the test section, an identical concave mirror gathers the light collected from the test section and refocuses it towards the camera using an additional planar mirror. The razor's edge was at the found horizontal focal point and oriented so that the planar densities observed would be for the vertical direction.

The Photron Fastcam SA-Z-2100K collected the Schlieren data. The camera could take up to two million frames per second (fps) and had a minimum exposure time of up to 159 nanoseconds. All parts of the optics utilized specialty optic tables for stabilization designed to reduce vibrations on the components during tunnel operation. Figure 21 shows images of the final physical set up for this system.

Post set-up some additional modification is possible to better diagnose the quality of images received by the camera. Each mirror is adjustable as needed to increase light quality or to move a viewing window into appropriate view. The camera's lens is also adjustable for changes in focal length that occur. The built in software provided for camera

use, Photron FASTCAM Viewer (PFV), provides some assistance for determining where finer adjustments are necessary. The software's probe tool helps report needed changes required to light intensity and other important factors.

Figure 21: Physical Schlieren set-up for experiments

Noticed during data analysis, obtained Schlieren data was not of equal quality for both QS1 and QS2 data. While QS1 Schlieren data was of sufficient quality throughout all tests, QS2 Schlieren data often saw variations in light intensity and in vertical position of the boundary layer. This inferred that either the knife-edge or the camera was vibrating due to tunnel activity during later parts of a given test. This inference has more weight as metal plates, which Figure 21 shows beneath the camera, adjusted the camera angle would match the half-angle of the cone. L brackets screwed into the table and pressed up against the plates to provide support to the metal plates. This would make it more prone to vibrational disturbance than if there was more secured support mechanisms for the camera. Towards the end of testing the purchase of a more secure camera mount for adjusting angle addressed this issue, but camera position and light intensity variation still affected a majority of QS2 data. While runs still obtained good QS2 data, the vibration led to

compromises in the number of Schlieren frames used for analysis of QS2 in comparison to the amounts used in QS1. Section 3.7 describes the process of frame selection in each state in more detail in.

3.6 Viewing Locations

To obtain a complete picture of the boundary layer across the entirety of the cone, five viewing locations represented different flow portions along the length of the cone in the Schlieren data. Each viewing location defined a viewing window that spans across the described horizontal length at each location. The approximate locations of these viewing windows correspond to the viewing locations chosen by Embrador to compare results [10]. Slight geometrical differences in the ability to obtain viewing windows resulted in viewing windows with minor differences from those chosen by Embrador. Figure 22 shows the viewing windows employed for the current work. Appendix D lists a full list of the positions of each viewing window used, and the chronologic order and driver tube pressures used during each run. All viewing windows employed the same camera settings in order to maintain consistency across photos.

Recommendations of Oddo and Embrador's theses suggested an employed camera frame rate of 600000 frames per second (fps), shutter speed of 0.16 microseconds, and total resolution of 640x32 pixels per viewing window. A high frame rate and close to minimum shutter speed allowed for higher levels of detail in turbulence features. If too low of a shutter speed cannot capture the features of the flow due to insufficient light. Embrador calculated that for one particular flow feature, second mode waves, .16 microseconds would be sufficient to capture a second mode wave traveling in the boundary layer with

sufficient detail [10]. Additionally, the resolution of 640x32 pixels fully captures the boundary layer sufficiently throughout all viewing windows based on previous observations.
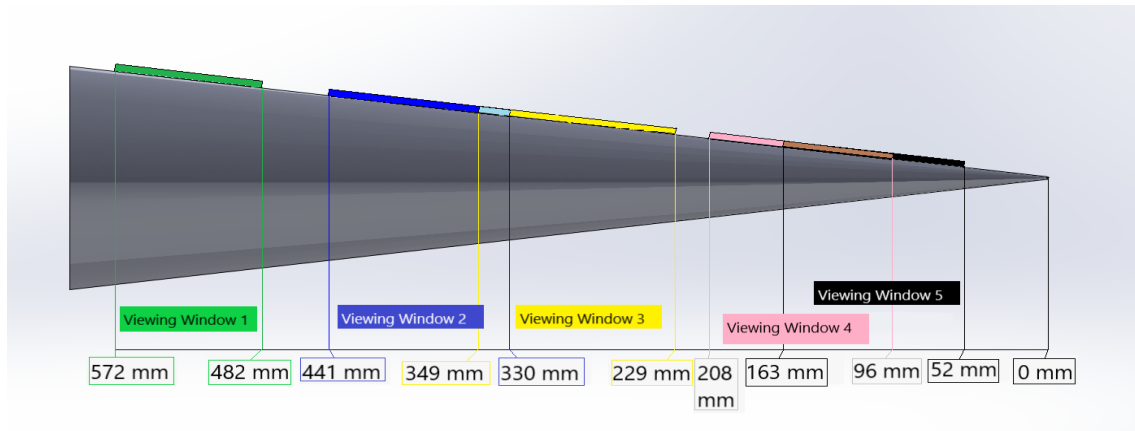

Figure 22: Viewing Windows, Distances are Measured with Respect to the Tip Along the Central Axis

When capturing data during flow, camera recording synchronized to the actuation of the fast-relief valve on the driver tube. The camera starts recording 0.3 seconds before the actuation occurs, allowing the camera to record the entirety of the expected 200 milliseconds of Mach-6.1 flow. This operated off a preset 25%/75% split set-up through the tunnel operation LabVIEW UI. Recording was primed via manual operation on the camera software, and then the syncing/recording process begins upon sensing of the beginning of tunnel operation.

Two steel nuts measuring about 5.6 mm in height were the basis for image calibration photos in each viewing window. Figure 23 shows an example calibration image from viewing window 4 during the uncooled runs. A pixel-to-millimeter conversion based on these heights output conversion factors for each viewing window for the conversion of

59

Schlieren data to physical units. Appendix D includes a full table of pixel to millimeter conversions for each viewing window during cooled and uncooled runs. The conversion factors listed in this table include a measurement uncertainty of 5 mm for the horizontal direction and an uncertainty of .1 mm in the vertical direction.

Figure 23: Calibration Image for Uncooled Viewing Window #4

Finally, the model and the tunnel were ready for testing after a clearing of measurement and calibration tools from the model surface. The model then received a final cleaning of acetone to remove any oils that may have come off on the model due to human interaction. Those oils could build up frost or unnecessarily trigger boundary layer transition, which was undesirable. After the cleaning process, the tunnel underwent air evacuation processes to bring it down to vacuum, after which final adjustments to the knife-edge occurred.

3.7 Turbulence Intermittency Calculations

Turbulence intermittency calculations as described by Casper et al. allowed for a quantitative measurement of where onset to transition occurred [69]. The method utilized sequential Schlieren images obtained during testing and applied a Canny edge-detection algorithm to detect boundary layer edges. This algorithm works by locating local maximum light gradients along an input reference image, which represents the average laminar boundary layer. Strong edges detected in this case define a baseline boundary layer thickness δ. With the laminar-boundary layer thickness defined, sequential Schlieren

images of the flow utilize the same edge detection algorithm, then a comparison of the two thickness outputs an intermittency value.

There are two main outputs from the algorithm. For each frame of the input Schlieren data, the edge detection algorithm calculates the current edge height and compares it to the reference height from the laminar layer height. For each pixel along the horizontal for the current edge height, if the current edge height is larger than the reference height, then the flow is marked as turbulent (an intermittency value of 1). All other results for δ at or below the reference boundary layer thickness report a turbulence intermittency value of zero, and thus laminar. The average values of turbulence intermittency at each pixel across all input frames output a total intermittency curve across the selected distance. Overall, the expected trend is that the flow should increase in turbulence intermittency as both driver tube pressure increases and distance along the cone increases, starting at near-zero intermittency eventually plateauing at or near a value of 1 in the most regions/conditions, monotonically increasing as a function of distance similar to a sigmoid curve. Figure 24 shows an example of a typical output curve as described by Casper et al [69].

Pre-processing of both the reference image and the input Schlieren data allowed the Canny Edge Detection algorithm to better discern boundary layer edges from surrounding flow noise. Two different sections of data serve as the basis of pre-processing, a 100-frame sample of pure background taken prior to the flow beginning and a large frame (2000 for QS1, 1000 average for QS2) sample of flow. The number of frames selected represent a compromise between computational time and accuracy to characterize fully the flow. 2000 frames was the target amount of frames for both QS1 and QS2; however, for a large number

of experiments, lighting during QS2 considerably varied for an accurate separation of flow details from noise for all 2000 frames normally desired. For a desire still to obtain QS2 data, a smaller subset Schlieren frames, averaging around 1000 frames was often taken instead of the 2000 obtained for QS1. The software ImageJ handled all image processing. The software both subtracted image noise from necessary data but also achieved reference images for the algorithm to compare to the data.
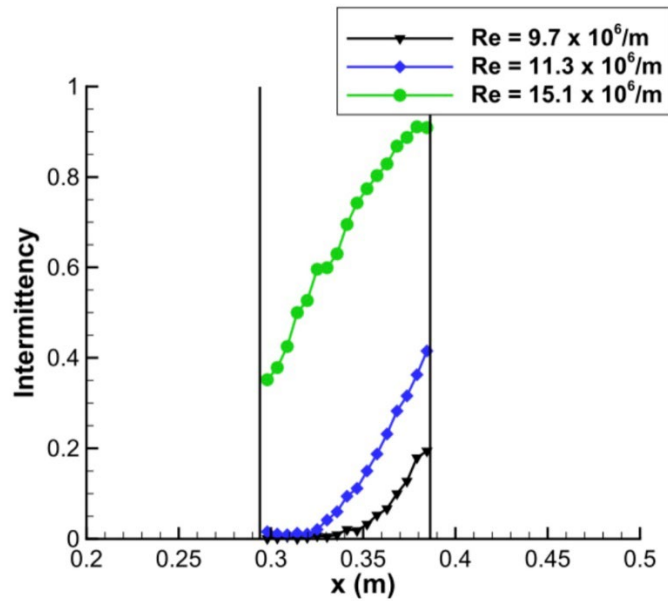

Figure 24: Example Boundary Layer Intermittency Results as Explained by Casper et al. [69]

For most cases of turbulence intermittency calculation, analysis mostly consisted of QS1 states. QS1 typically had the most pictorial clarity and consistency with lighting conditions. Due to vibrations due to tunnel operations ending up causing variation in camera tilt and relative knife-edge position, some of the collected QS2 data obtained showed varying intensity values in lighting conditions. Unfortunately, this problem appeared only after collecting the data. Fortunately, some QS2 data was good enough for image processing, averaging about 1000 frames per run. The worst case of QS2 obtained

800 frames of useable Schlieren data, while the best case could obtain the full 2000 frames. Analysis of QS2 data focused primarily during qualitatively observed transition regions, utilizing the often-smaller subset of frames to minimize the effect of lighting and position variation. While lower than the ideal case of 2000 frames, the frames used for QS2 analysis were still suitable for data analysis. The original paper from Casper et al., which identified this method of calculating transition, noted that its data sets worked with 1200 useable frames [69], so the 1000 frame average of QS2 was suitable to gather enough information about intermittency from the data.

The first step of image processing for both the background and each of the QS flow data was to flip the images so that flow would be travelling from left to right in the images, since the algorithm employed utilizes an assumption of left-to-right flow. Once completed, the average intensity across all frames in each case achieved a basic, unprocessed reference image for both the background and the data flow. Figure 25 shows an example of what is output at this point. The intensity of the background reference image was increased by a factor of 1.05, as it was found when implementing the canny-edge detection algorithm this most reliably reduced most of the background noise when combined with the other steps. This new background image subtracts from the average-intensity flow image to obtain an image of a reference boundary layer thickness consistent with times when the boundary remained in a laminar state. A non-linear histogram gamma-correction factor of 1.3 corrected the photos for remaining noise, chosen based processing settings selected by Embrador [10]. Small samplings of 100 frames of data confirmed that this methodology in most data cases removed most, if not all, noise from the images leaving on boundary layer flow details present for the algorithm. Figure 26 shows the result of this image processing,

with the flow shown traveling from left to right. This same background subtraction and gamma correction then applies to the entire Schlieren frame data sets for QS1 and QS2. These frames utilize the Canny Edge Detection algorithm for intermittency calculations.
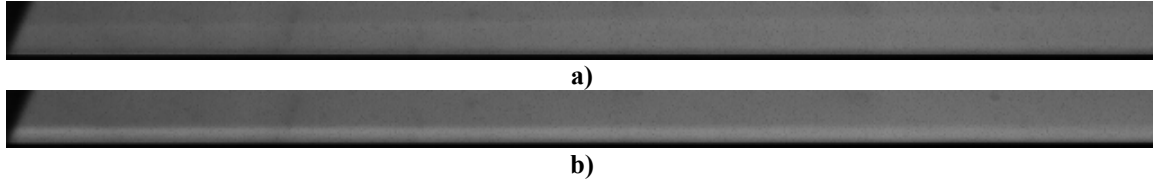

a)

b)

Figure 25: Pre-Processed for a) Average Background Intensity and b) Average Laminar Boundary layer thickness for Run 17 (150 psi) Uncooled ($T_w/T_0 = .59$)

Figure 26: Post-Processed Image for Average Laminar Boundary Layer for Run 17 (150 psi) Uncooled ($T_w/T_0 = .59$)

The Canny Edge Detection algorithm analyzed the then post-processed data frames via MATLAB file. Within the algorithm, empirical observations defined a few user-defined parameters prior to running. The first parameter defines any necessary image rotations to eliminate constant error due to slight imprecisions due to camera alignment. This was due to the fact that even small offsets, such as a rise of 3 pixels over the entire 640 pixel length, produces significant differences in turbulence intermittency and boundary layer thickness data.

The second parameter defines a boundary layer offset. The offset is a parameter the algorithm used to distinguish real turbulence from minor height modulations in otherwise laminar flow. This set the criterion line for turbulence a certain number of pixels above a defined point. The magnitude of the offset was set to be a value greater than or equal to one, which accounts for statistical variations due to remaining noise, weak edges detected

by the algorithm, as well as account for natural growth and disturbances of the boundary layer over the length of the cone. An offset value of less than one pixel produces unexpected discontinuities in turbulence intermittency or leads to turbulence values biased higher. Too large of an offset value produces turbulence intermittency values biased too low.

The final parameters of the Canny Edge Detection algorithm, such as threshold coefficient and pixel connectivity, affect the ability of the algorithm to discern strong enough of a gradient to warrant an edge being detected as a boundary layer. Adjusting the threshold coefficient reduces risk of remaining background noise identification as flow features. Adjusting pixel connectivity also helps with this differentiation. Most other algorithm parameters remain constant at default values between runs, as both light remained constant and noise left over from pre-processing remained relatively low not to warrant any changes to those values. These default values included a Canny threshold coefficient of 2.9 and a noise-removing constant of 10. The noise-removing constant is a constant that stated the algorithm located unconnected pixels (noise) in the current image of length less than the stated value and remove them from the image.

3.7.1 Capturing Boundary Layer Instabilities

In addition to turbulence information and boundary layer thickness, the characteristics of instability mechanisms within the flow was also a flow factor that was some insight was desired, with specific focus on second mode waves and the wisp characteristics. To perform this an analysis derived from a process similar to that employed by Jagde et al. in order to determine wave speed, wave frequency, and location of both types of structures [70]. A reutilization of Schlieren data employed for turbulence

intermittency is necessary. All processed Schlieren frames undergo a fast Fourier transform to search for relative frequency spikes characteristic of instability structures. Figure 27 presents an example of instability structures within the boundary layer flow.
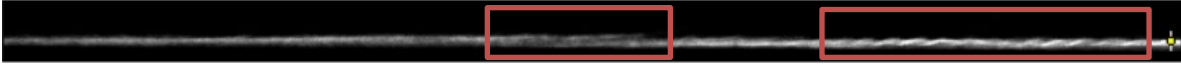

Figure 27: Wisp (Left Box) and Second Mode (Right Box) Structures Traveling Left-to-Right in Run 12 (300 psi, x=96-208 mm) Uncooled (T_w/T_0=.59)

First, the transformation of the processed images output a calculated wave speed. This calculation involves a pixel-to-pixel cross correlation between frames where an instability mechanism is present. Combining this information with the knowledge of time between frames, which in the 2000 frame case is 3.33 µsec per frame, can output the wave speed of each mechanism. The pixel-to-distance conversion rates calculated previously and listed in Table 9 to obtain a final wave speed in terms of physical units. A spatial FFT uses the velocity information, as well as the movement between frames of a selected instability at each row of pixels in a frame, to determine the frequency characteristics of a desired instability across a spectrum.

The method described above gives frequency spectra as a function of height along the image due to the correlation being row-based. Second mode instabilities, in particular, travel across the top of the boundary layer in particular so qualifies as a pixel row-based method. The frequency spectra output can be analyzed to observe the dominant instability frequencies at a given height. A power spectral density graph presents relevant frequency characteristics of each instability. These figures show local maximum intensity values at the dominant frequencies of the investigated instability.

IV. Analysis and Results

The results presented in this chapter are from a hypersonic boundary layer transition experiment performed at the AFRL Ludwieg Tube using a 7-degree half-angle cone with a 1.5 mm radius rounded tip at a 0-degree angle of attack. Schlieren imaging utilized similar viewing windows as described in Embrador's work to determine transition location and disturbance frequencies in comparison to the sharp tipped cone case studied by Embrador [10]. This effort expands on work relating to the effect of wall cooling and temperature ratios on boundary layer transition by looking into the possible role of cone geometry.

4.1 Boundary Layer Thickness Comparison

To measure nominal boundary layer thickness, sequences of images that presented the fully laminar flow for each run case were analyzed. An edge detection algorithm determined the locations of both the height of the boundary layer and the height of the cone surface at each viewed location. Given the free-stream Reynolds number conditions of each run and QS states, Equation 10 could determine the laminar boundary layer thickness across a given condition.

$$\delta = A \frac{x}{\sqrt{Re_x}} \tag{10}$$

A in Equation 10 is known as a leading coefficient and is approximated by the edge detection algorithm. For cases where the flow was sufficiently turbulent such that no laminar boundary layer could be obtained from the Schlieren data for use in the edge detection algorithm, a polynomial fit equation was employed, extrapolating from the last

upstream viewing window at a given driver tube pressure where laminar data could be obtained.

4.1.1 Uncooled Boundary Layer Thickness

Appendix E shows the results of the obtained laminar boundary layer thicknesses for each viewing window in the uncooled cases for each driver tube-pressure condition. Each initial driver tube pressure corresponds with approximately equal freestream unit Reynolds number conditions. With each figure is included the available data from Embrador showing boundary layer thicknesses from similar flow conditions during sharp-tipped cone experiments [10]. The thick solid dashed lines denote the new data obtained from the blunt-tipped cone, while the thinner dot-dashed lines denote past data obtained by Embrador. The solid color vertical lines show each individual viewing window limits used in the current experimental work. When frames of a given run contained solely turbulent flow and no frames of pure laminar flow (i.e. the downstream viewing window in all cases), laminar boundary layer thickness was extrapolated from the laminar boundary layer reference image of the next upstream viewing window fully laminar flow was observed. This extrapolation occurred only during uncooled runs. Cooled runs exhibited sufficiently laminar conditions that extrapolation was not necessary.

While results for the blunt-tipped cone do not perfectly align with upstream/downstream values under similar conditions, the data was consistent within experimental error. The largest discontinuity presented is at lower Reynolds number conditions. Higher noise present at these conditions makes contrast for the edge detection algorithm harder to distinguish accurately the boundary layer thickness. Overall, though, the boundary layer thicknesses showed good continuity. The data obtained supports

existing theory and data indicating thicker boundary layers during the blunt-tipped cases than the compared sharp-tipped cases, as expected. Table 4 summarizes the total differences in laminar boundary layer thicknesses for the uncooled surface conditions. The data presents that the boundary layer thickness consistently increases during the transition between QS1 and QS2 states, which is expected due to the lower unit Reynolds number conditions.

Table 4: Height and Percent Differences in Laminar Boundary Layer Thicknesses Between Uncooled Blunt-Tipped and Sharp-Tipped Cones in Analogous Conditions

Initial Driver Tube PSI	QS State	Average Difference in Thickness (mm)	Average Percent Difference
50	1	.323	9.3%
100	1	.230	10.4%
100	2	.462	18.5%
200	2	.803	40.9%
400	1	.571	48.5%
500	1	.380	48.4%

4.1.2 Cooled Boundary Layer Thickness

Appendix E additionally shows the results of the estimated laminar boundary layer thicknesses for each viewing window in the cooled runs for each driver tube-pressure condition. Available data from Embrador's sharp-tipped data was also included for comparison to the sharp-tipped case [10]. Formatting for these figures follow that of the uncooled figures. An aspect in each of the cooled boundary layer thicknesses that may

stand out is that the furthest downstream viewing window in each driver tube-pressure condition seems to be discontinuously thinner than the next upstream location. Figure 28 exemplifies the physically observed difference observed in boundary layer thickness between the runs, ruling out the possibility of an algorithmic mistake. The most likely explanation for the differences comes from unanticipated differences in cooling during cooled experiments.
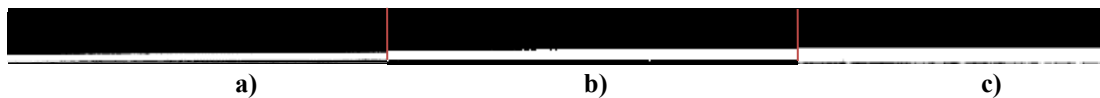

a)   b)   c)

Figure 28: Comparison of Cooled (T_w/T_e=1.40 ± 0.05) Laminar Boundary Layer Thicknesses at P_{DT} = 200 psi for a) Run 40 QS1 (Cooled Viewing Window 1, x=476-578 mm), b) Run 49 (Cooled Viewing Window 2, x=330-445 mm), c) Run 18 (Unccoled Viewing Window 2, x=330-441 mm)

Cooled experimentation employed two different dewars during different run days. A dewar replacement took place about halfway through testing because a loose valve during LN2 refilling prevented safe operation of the dewar in later experiments. Both dewars that supplied LN2 to the model for cooling were sufficient to supply enough LN2 for two full days of experimentation. Since Embrador got three days' worth of experimentation out of a 180 liter dewar, a 120 L dewar assumed enough capacity for two days' worth [10]. The order in which the experiments were performed, which Appendix D presents schedule information pertaining to, meant that on a single canister of LN2 first Runs 37-43 were performed and two days later Runs 46-52 were performed. These differences in the data only emerged upon analysis. The data suggests that Runs 46-52 may not have achieve adequate cooling to reach the same temperature conditions as the rest of the runs. Possible explanations include a low supply of LN2 or possibly the formation of

crystals in the supply lines. There was some effect of cooling present, as those conditions did see a noticeably lower laminar boundary layer thickness when compared to the uncooled case; however, the data suggested that the cooling did not to reach the desired condition in these particular runs as it did in Runs 37-43. These runs, which represent the most downstream viewing window in all driver tube pressure conditions (viewing window 1), present data which suggest that the cone surface cooled to the desired point and are more representative of the fully cooled system. Examining turbulence transition exemplifies a possible difference of surface cooling further, and Section 4.3 discuss these more in length.

Beyond this discontinuity jump in the data, it also confirms a larger boundary layer thickness on the cooled blunt-tipped case when compared to the cooled sharp-tipped case, but an overall reduction in boundary layer thickness when compared to the uncooled blunt-tipped case. It also confirms a general trend of QS2 having a slightly larger laminar boundary layer thickness than QS1.

4.2 Transition Results – No Surface Cooling

Turbulence intermittency analysis was the method for obtaining a quantitative measure turbulence transition in the boundary layer. High-speed Schlieren methods calculated intermittency using methodology as described in Section 3.7. As noted by Casper et al. [69], a turbulence intermittency of unity normally indicates a fully turbulent flow and an intermittency of zero suggests fully laminar flow. Following the criterion set by Oddo [9], a threshold of 0.10 turbulence intermittency established the onset of transition to turbulence in the flow in the current work. Once the intermittency curve first crossed

this 0.10 threshold that is where transition onset begins. This accounts for lingering measurement noise still present in the data. This threshold proved to be a useful threshold in previous, so use of it was continued. Oddo additionally noted originally that 0.80 would be the nominal point where turbulence intensity would appear to plateau and therefore would be the determining threshold for when the flow was fully turbulent and transition was complete.

In the current work, "plateaus" in the data where qualitatively full turbulence has been achieved may, at times, temporarily cross this 0.80 threshold but not stay absolutely above this threshold. One possible explanation for this is lower accuracy in detecting edges in fully turbulent flow. Decreasing the criterions for measuring turbulence for the possibility of meeting this 0.80 threshold sacrificed accuracy with laminar boundary height. Qualitatively, at all driver tube-pressure conditions except 50 psia, the most-downstream viewing window (viewing window 1) was fully turbulent. 50 psia driver tube pressure presented an exception, as here were some brief periods of laminar flow in between the turbulent flow in furthest downstream data. This is to justify qualitatively that fully turbulent data may not be above this 0.80 threshold for the entire length of the viewing window. Figure 29 shows an example of this full turbulence flow for the 200 psia uncooled case viewed from x=482-572 mm in sequence. The flow shown in this figure is fully turbulent, but the corresponding intermittency values in Figure 30d report intermittency values with a maximum around 0.6. Without sacrificing boundary layer thickness accuracy, the quantitative plateau that appears in the data in the final, most downstream viewing window defines the end of transition in addition to the .8 threshold.
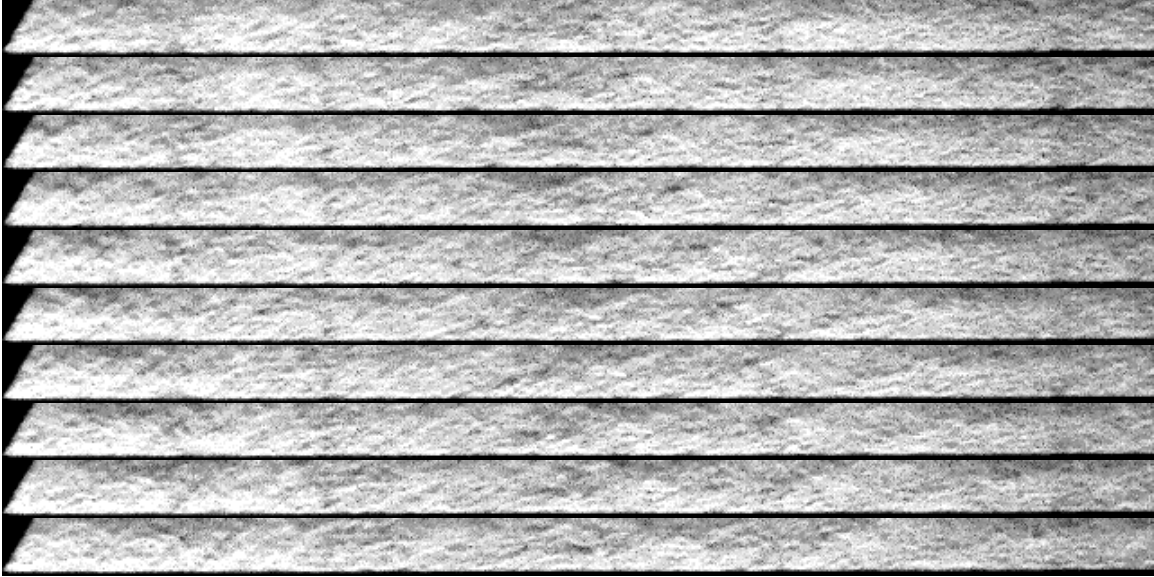
Figure 29: 10 Sequential Frames of Turbulent Boundary Layer Schlieren Data (Flows Left-to-Right) from Run 32 (P_{DT} = 200 psi, x=482-572 mm) Uncooled (T_w/T_0=.59)

Figure 29 also exemplifies large black edges present in some obtained Schlieren data, caused by data gathered at the edge of visible light created by the arc light in the Schlieren set-up. Intermittency data presented trims the areas these black edges occurred from the analyzed results, as including them lead to inaccurate intermittency calculations.

Results for turbulence intermittency for the blunt-tipped cone compare turbulence intermittency results presented by Embrador for the sharp-tipped cone. Those experiments utilized the same facility and the same measurement techniques, as well as similar test articles changing only the nose tip radius on the current model [10]. Figure 30 shows turbulence intermittency calculations for the uncooled cases, presented in order of ascending initial driver tube pressures from 50 psia (.34 MPa) to an upper test bound of 500 psia (3.44 MPa). Thick solid lines denote the data obtained during current work with the blunt-tipped nose for both QS1 and QS2 data. Dashed lines denote Embrador's results for the sharp-tipped cone for similar freestream unit Reynolds numbers (approximately

73

equal initial driver tube pressures). The solid, horizontal line marks the noise floor threshold of 0.1 to help visually denote the location at which the onset of transition occurs.
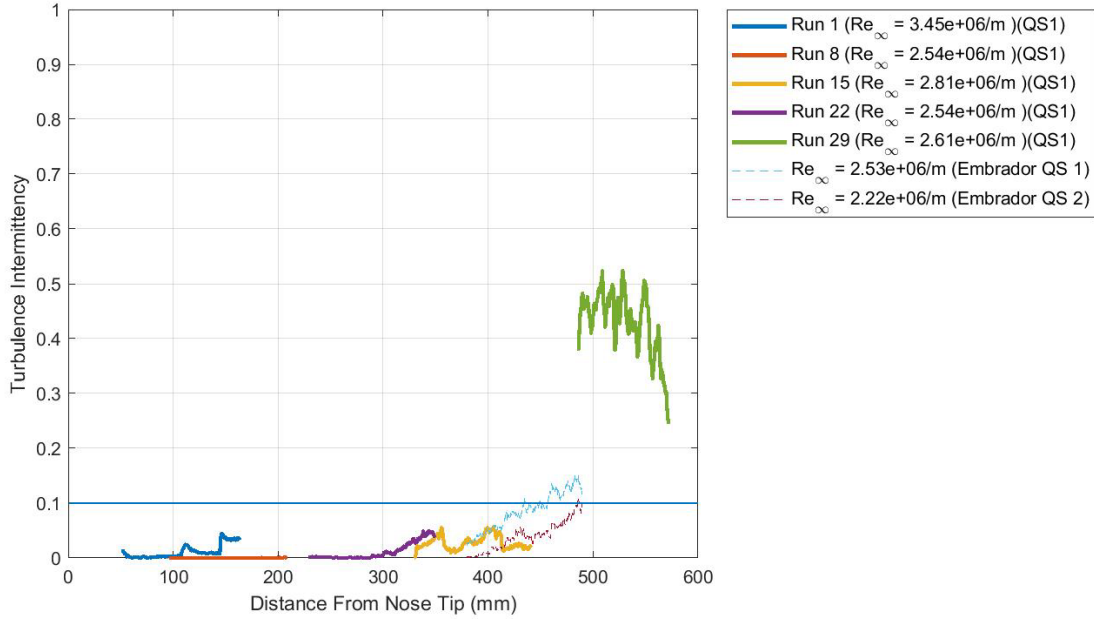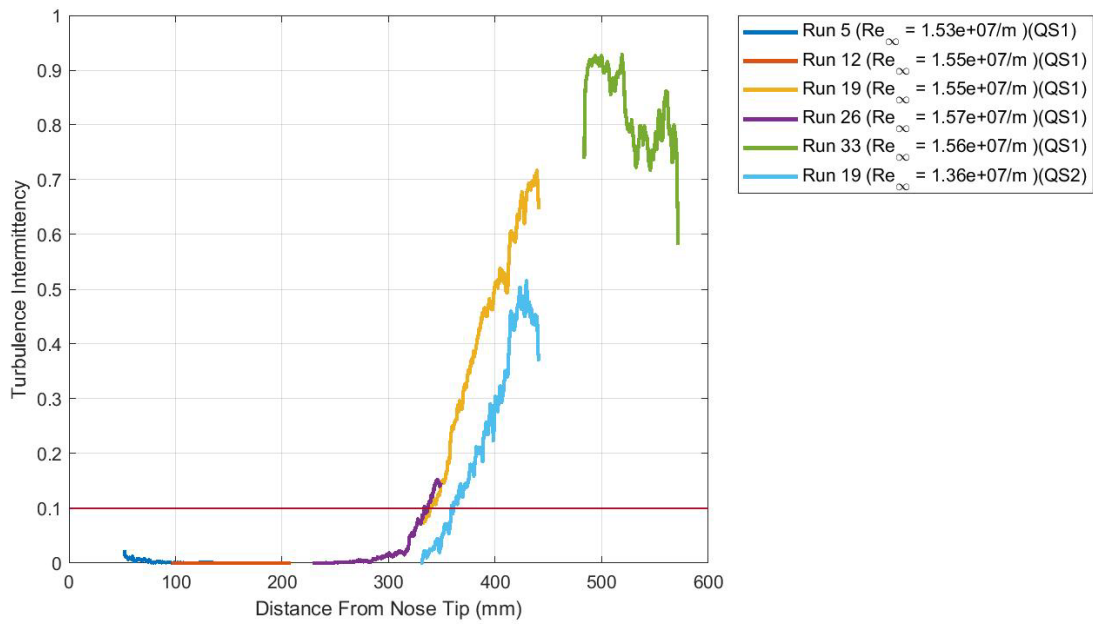

a) P$_{DT}$ = 50 psi (.34 MPa)
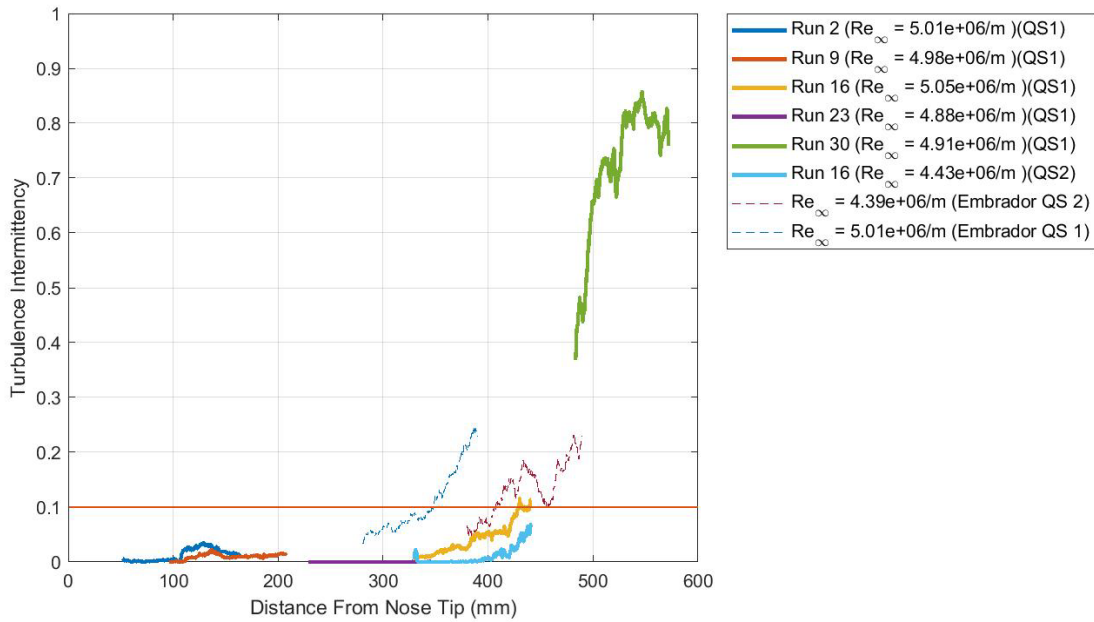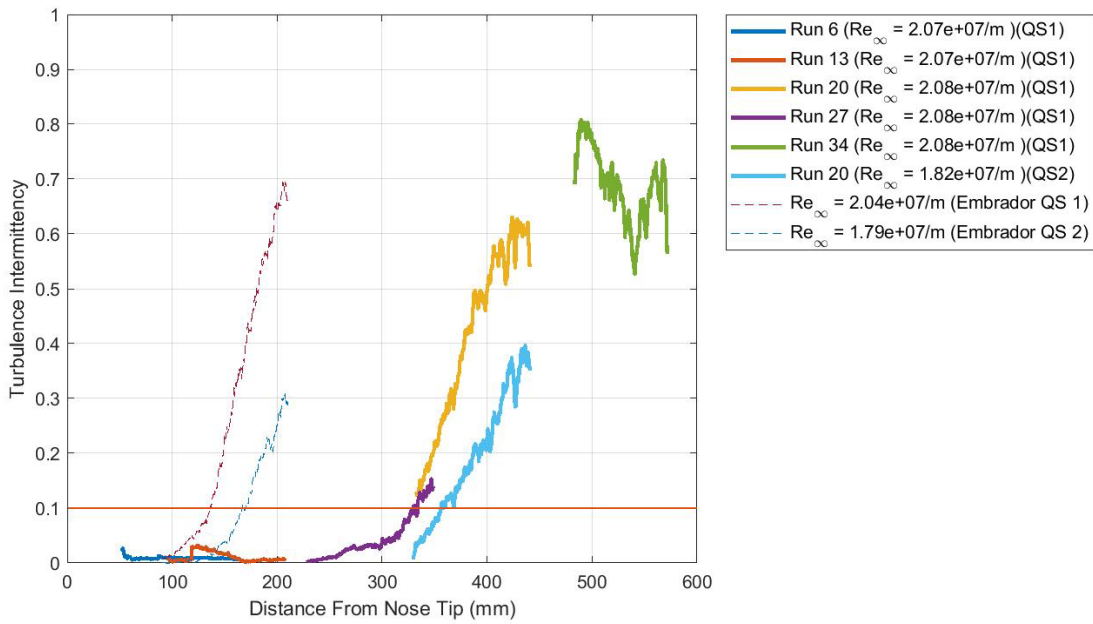

b) P$_{DT}$ = 100 psia (0.69 MPa)
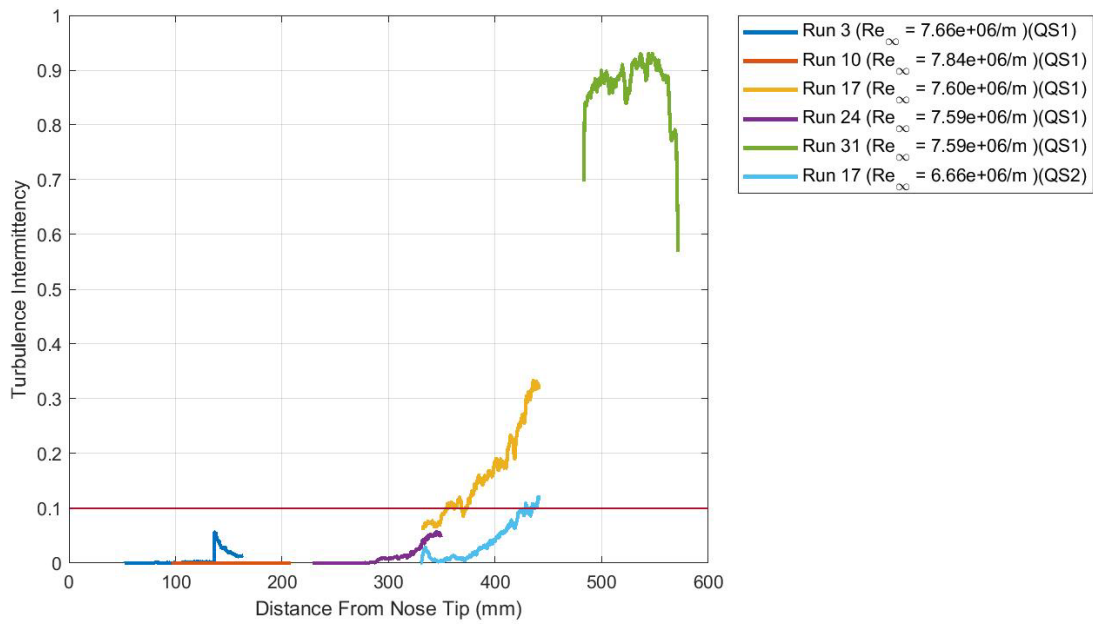
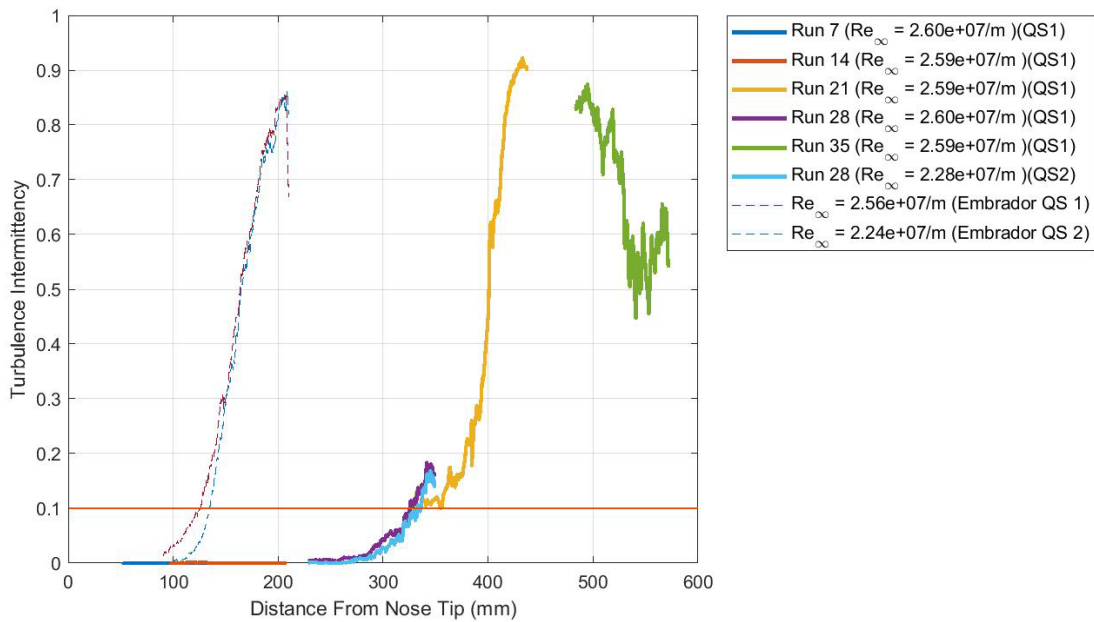**c) P_{DT} = 150 psia (1.03 MPa)**
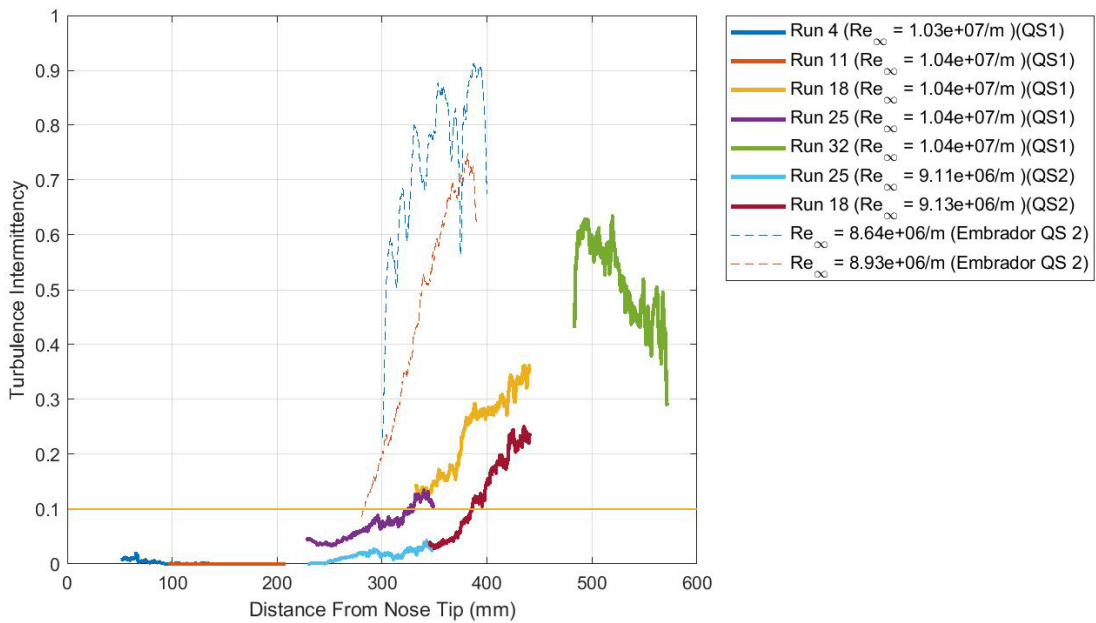
d) P_{DT} = 200 psia (1.38 MPa)

e) P_{DT} = 300 psia (2.07 MPa)
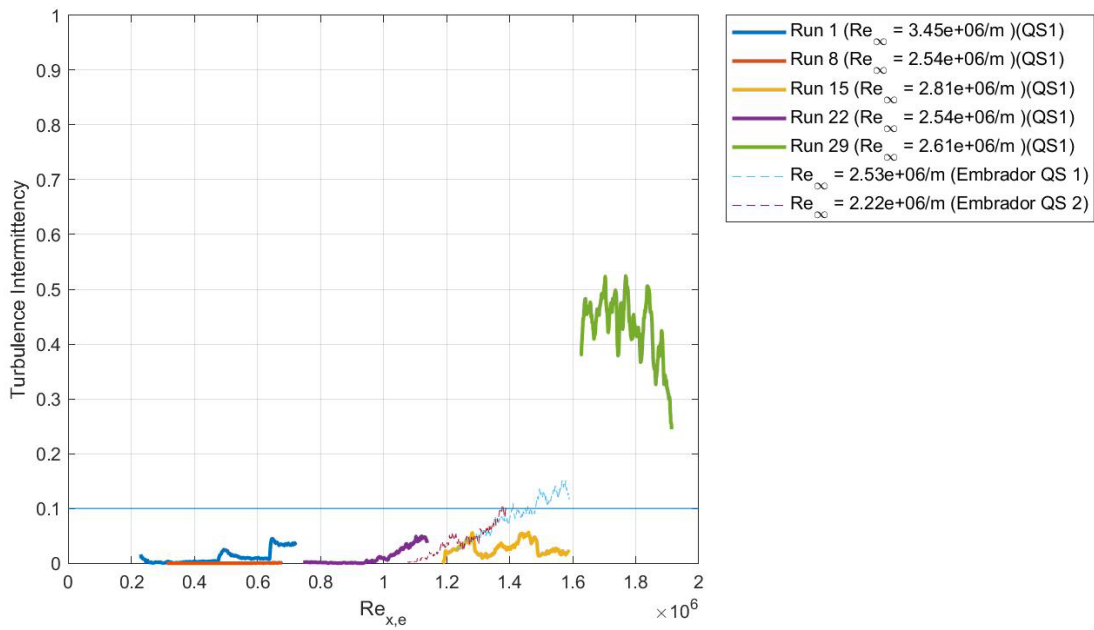

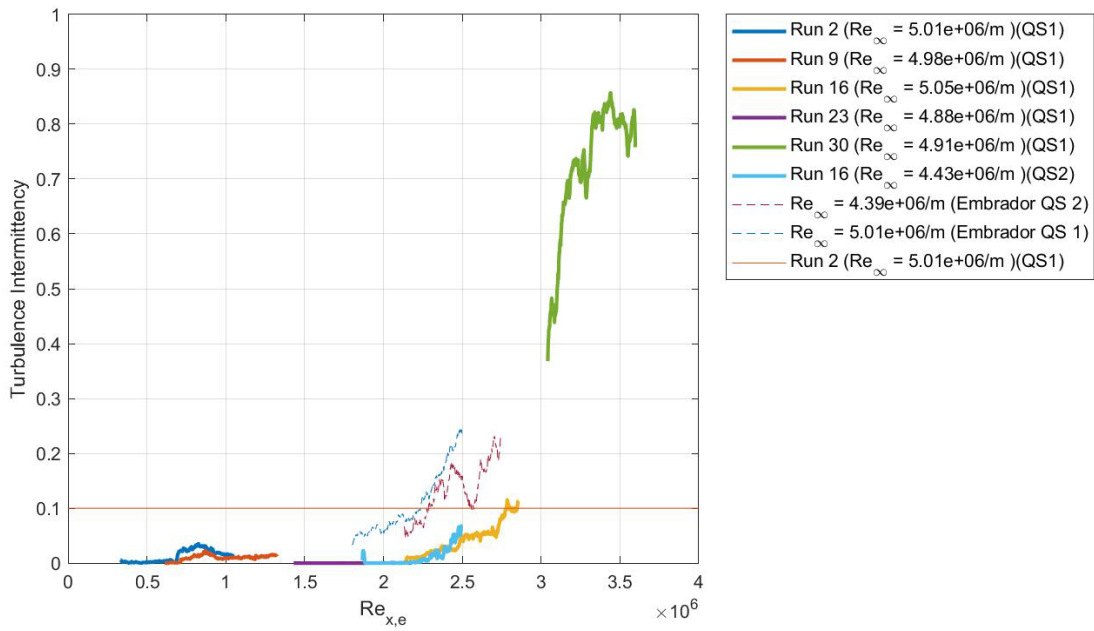f) P_{DT} = 400 psia (2.76 MPa)

g) P_{DT} = 500 psia (3.44 MPa)

Figure 30: Turbulence Intermittency vs. Horizontal Distance from the Nose Tip for Uncooled Experiments Re$_\infty$ = 2.7x10^6 – 2.7x10^7 /m, T_w/T_0 = 0.59 (T_w/T_e=4.35 ± 0.15)

As can be seen in Figure 30, the blunt-tipped cone in the uncooled case does appear to delay transition from what the sharp-tipped case data presents. Transition onset delay increases as unit Reynolds number increases, with almost a 200 mm difference in transition location at the 500-psia driver tube pressure when compared to the 50-psia driver tube-pressure case. These delays remain apparent even when observing the non-dimensional data, as observed in Figure 31. Estimations for surface Reynolds number for the blunt nose cone used a Taylor-Maccoll solution for the equivalent geometry sharp cone case. While analysis occurred for QS1 the full length of the blunt-nosed cone between 92 mm and 576 mm due to the higher quality of the Schlieren data, QS2 analysis focused on the runs that observed an onset to turbulence qualitatively.
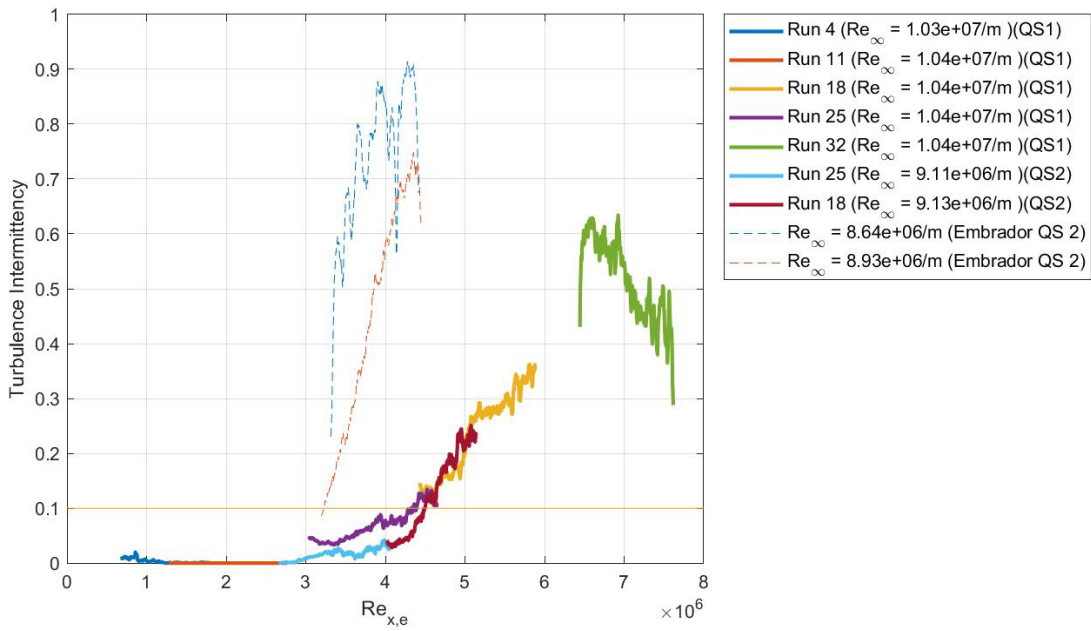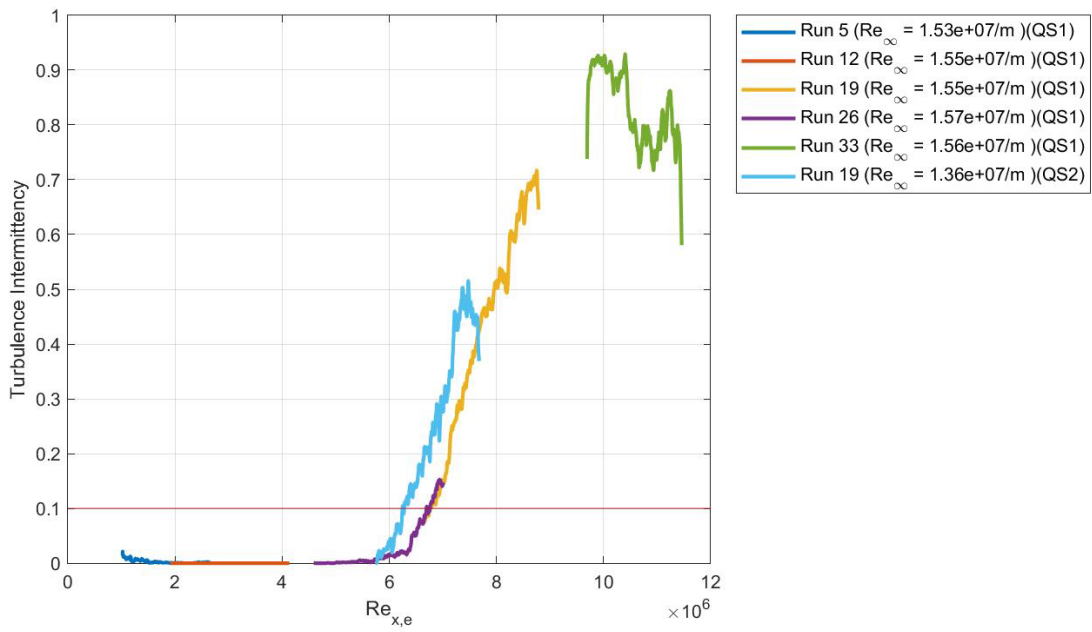
a) P_{DT} = 50 psi (.34 MPa)
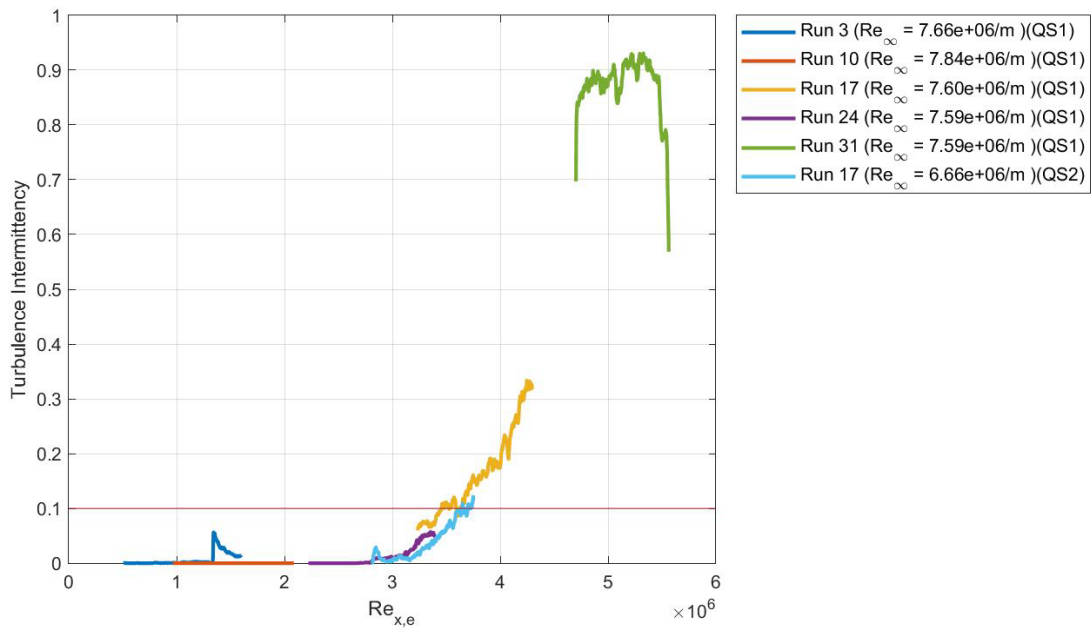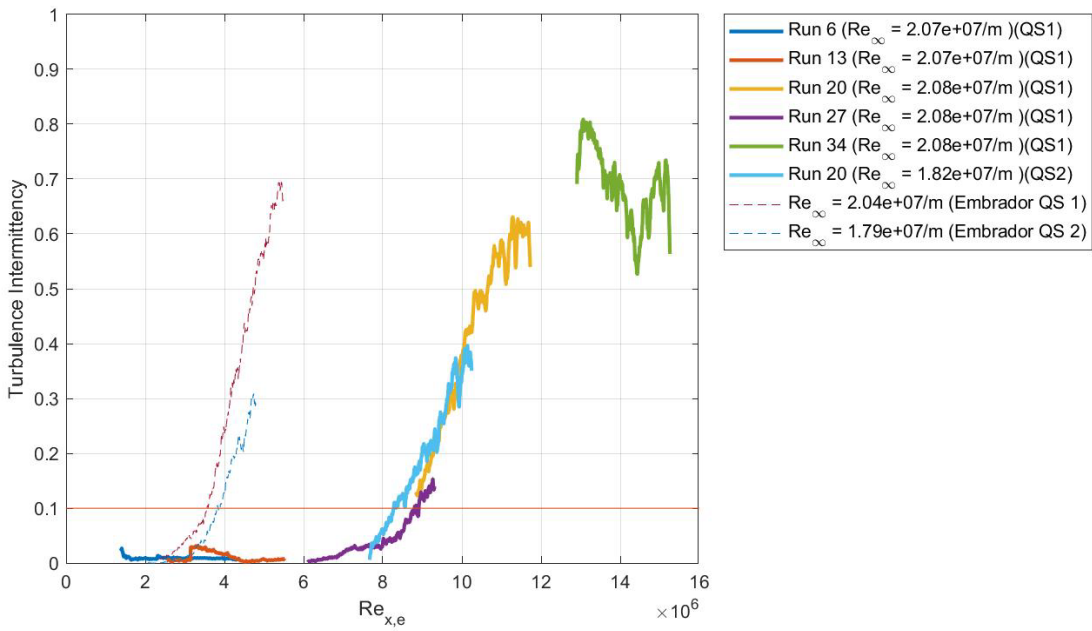

b) P_{DT} = 100 psia (0.69 MPa)
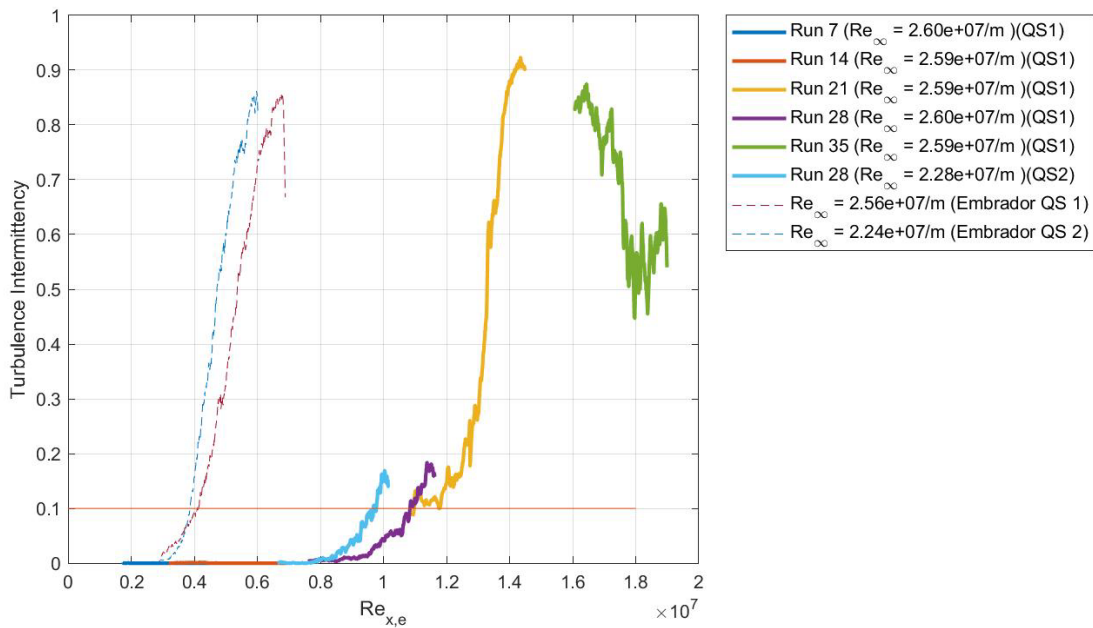
c) P_{DT} = 150 psia (1.03 MPa)

d) P_{DT} = 200 psia (1.38 MPa)

e) P_DT = 300 psia (2.07 MPa)

f) P_DT = 400 psia (2.76 MPa)

g) $P_{DT} = 500$ psia (3.44 MPa)

Figure 31: Turbulence Intermittency vs. Local Surface Reynold's Number for Uncooled Experiments $Re_\infty = 2.7 \times 10^6 – 2.7 \times 10^7$ /m, $T_w/T_0 = 0.59$ ($T_w/T_e = 4.35 \pm 0.15$)

As unit Reynolds number increases both QS1 and QS2 both appear to approach and eventually remain close to a stationary turbulence transition point at around 330 mm in dimensional results. One explanation for this involves the entropy layer swallowing length. The swallowing parameter vs. Mach number relationship developed analytically by Rotta [57] as described in Section 2.8 calculates the expected swallowing distance for each initial driver tube pressure by averaging the unit Reynolds numbers at each condition. Figure 32 shows the resulting estimated swallowing lengths for the cone used in the blunt-tip tests nose tip radius of 1.5 mm. Figure 32 shows the expected swallowing lengths as blue circles, and are shown with respect to the viewing windows chosen for the experiments, with the bounds of each viewing window denoted by different color solid horizontal lines. At the

81

higher driver tube pressures, the swallowing distance begins to approach the experimentally determined transition location. As stated by Stetson [74], an expected result is that transition location and swallowing lengths on the same order of magnitude have a stabilizing effect on the boundary layer. One possible result is that transition onset location in these high unit Reynolds number conditions remain stationary as driver tube pressure increases due to the increasing proximity of the stabilizing effect of the encroaching swallowing length.
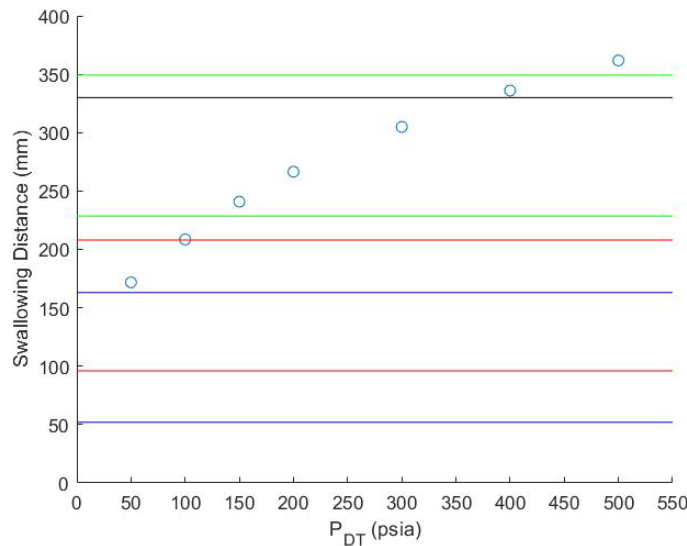

Figure 32: Expected Uncooled Swallowing Length as a Function of Driver Tube Pressure Using Methodology Described by Rotta [57]

There is an observed difference in transition onset location between QS1 and QS2, with QS2 generally transitioning later than QS1 in the dimensional results. This difference in turbulence between QS1 and QS2 does appear to decrease in both the sharp and blunt-tipped cones as increasing unit Reynolds numbers. This is in line with the results from Embrador [10] that found similar results in diverging onset locations between the two

quasi-steady states, and partially explained by the lower Reynolds number in QS2. The possible explanation proposed by Embrador for these diverging trajectories is that QS1 might introduce more noise to the boundary layer leading to more possible disturbance frequencies increasing the possible transition to turbulence. This is remains a possible factor for the blunt-tip case as, generally speaking, QS1 remains more turbulent on average than QS2. The boundary layer could still be receptive to increased disturbances in the freestream, despite stabilization caused by the entropy layer.

4.3   Transition Results – Cooled Wall Experiments

Using the cooling methodology described in Section 3.4, the cone was cooled internally from approximately room temperature to an average surface temperature of 95 K, which equates to a wall-to-stagnation temperature ratio of $T_w/T_0 = .19$ (T_w/T_e 1.40 $\pm$ .05). This is an average obtained the thermal equilibrium temperatures recorded from the six diode locations during initial cool down testing. Readings from this test recorded a surface temperature distribution ranging from a minimum of 83 K near the cone base and 123 K at the cone tip. After a 25-minute LN2 gradual valve opening process, a 95-minute waiting period cooled the model to suitable thermal equilibrium conditions prior to each days' experimentation. An additional cool down period of 30 minutes of LN2 flow with a slightly open valve between runs ensured consistent thermal conditions. Beyond initial testing to measure the expected temperature profile of the cone, there was no confirmation of surface temperature in between runs. Previous work on the sharp-tipped cone by Embrador [10] suggested that these conditions would be suitable to achieve multiple cooled runs across a given day without significant error.

As with the uncooled cases, a mirror-based Schlieren set-up recoding at 600,000 frames per second captured boundary layer data. Prior to cooling on each run day, an initial dummy uncooled test run purged the air circulation system of any remaining moisture to prevent frost build-up. Frost build-up on the model has the possibility of triggering boundary layer transition due to abrupt changes in surface roughness. A visual check in between individual runs confirmed that frost build-up on the test article never exceeded more than a very light sheen. Figure 18 presents an example of the light sheen observed and Figure 33 presents a comparison compared approximate acceptable level of frost sheen Embrador work observed.
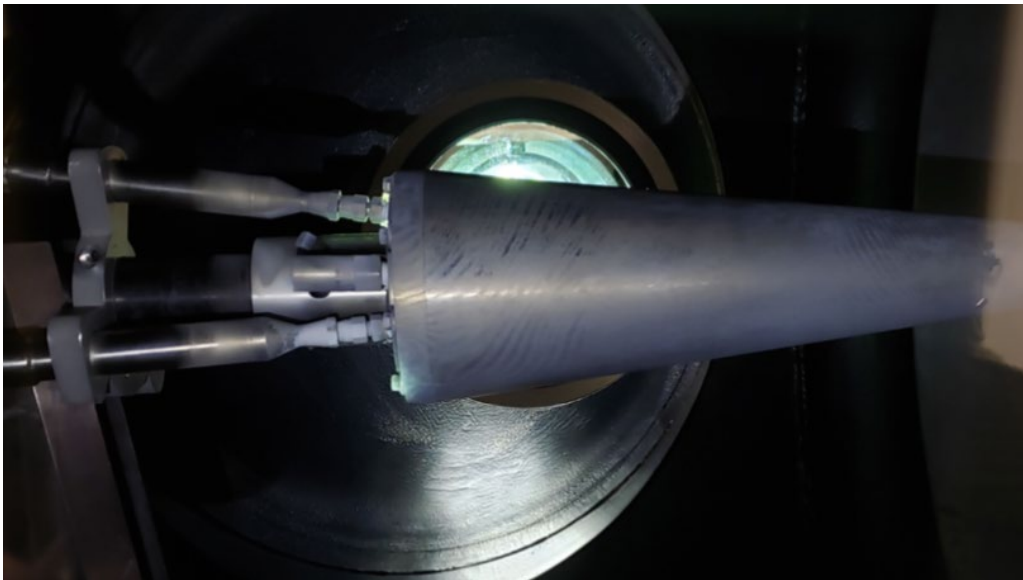

Figure 33: Example of Frost Surface Sheen as Described by Embrador for Sharp-Tipped Cone Run 33 [10]

LN2 "snow" occasionally appeared in the tunnel during initial cool down. This occurred in the days after transfer tube ports on the tunnel were changed, and primarily attributed to a connection not being entirely secure. After consultation with the supervising

wind tunnel operator when observed, experimentation continued as expected. The "snow" disappeared after the initial cooled run of the day and did not appear again after securing and tightening transfer line connections after the day's runs.

Schlieren data underwent turbulence intermittency calculations for nearly identical viewing windows used for uncooled case. Recording of uncooled Schlieren data took place starting from the most upstream location progressing to the most downstream location. Conversely, recording of cooled Schlieren data took place starting from the most downstream location progressing to the most upstream location. Figure 34 shows the results of the turbulence intermittency calculations, and follow a similar figure formatting convention to the analogous uncooled figures. Similar to the uncooled figures, the attempt is to compare the newly obtained blunt-tipped cone data to data obtained by Embrador for the sharp-tipped cone of similar geometry [10].
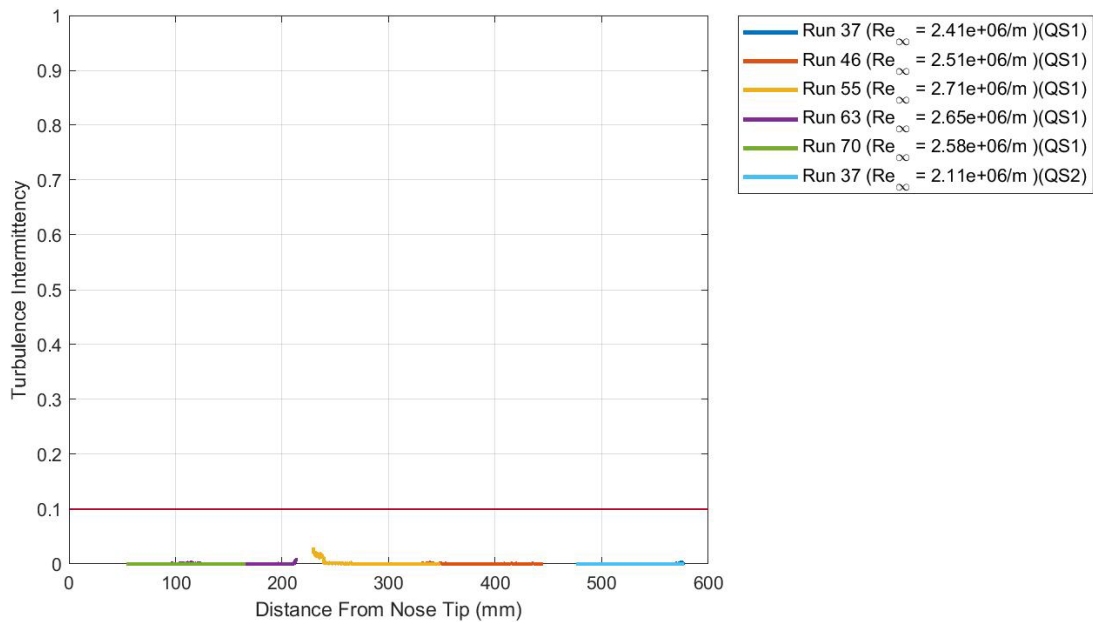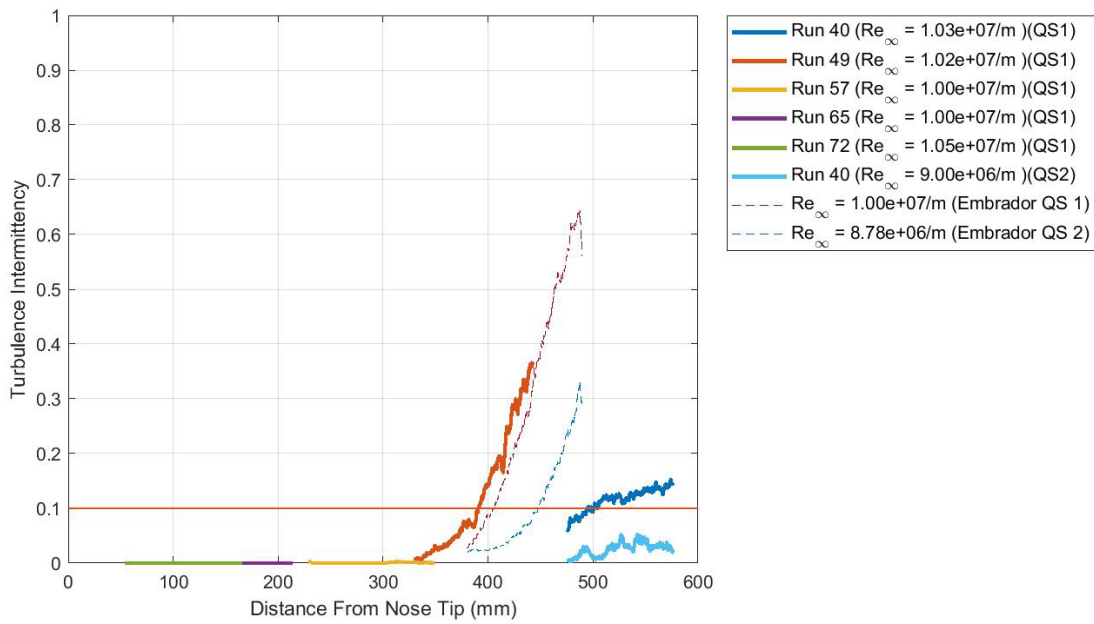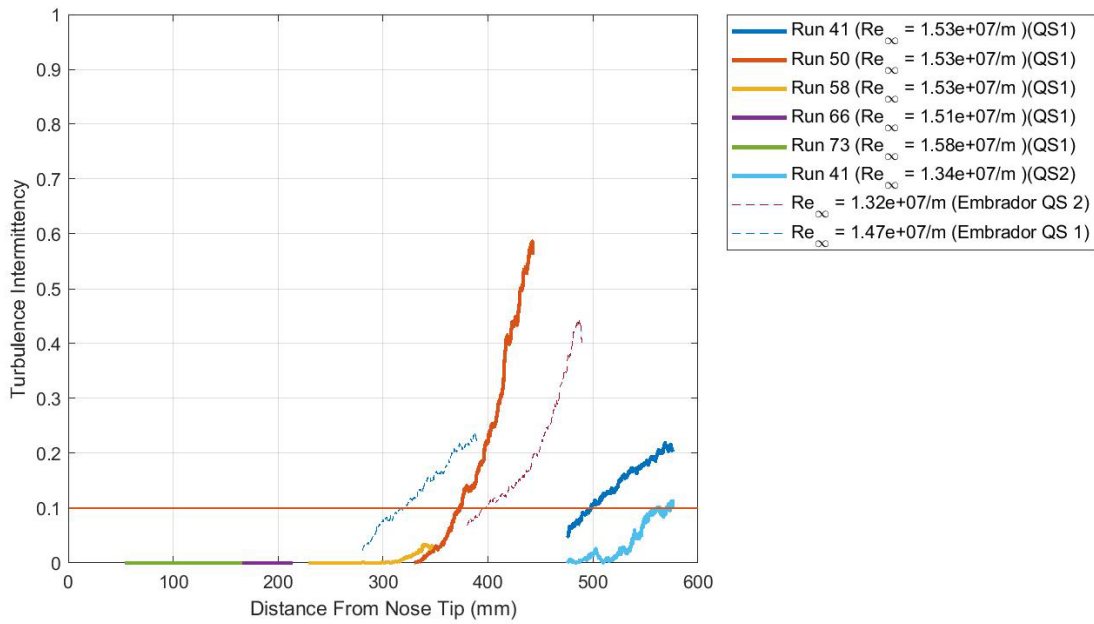

a) P_{DT} = 50 psi (.34 MPa)
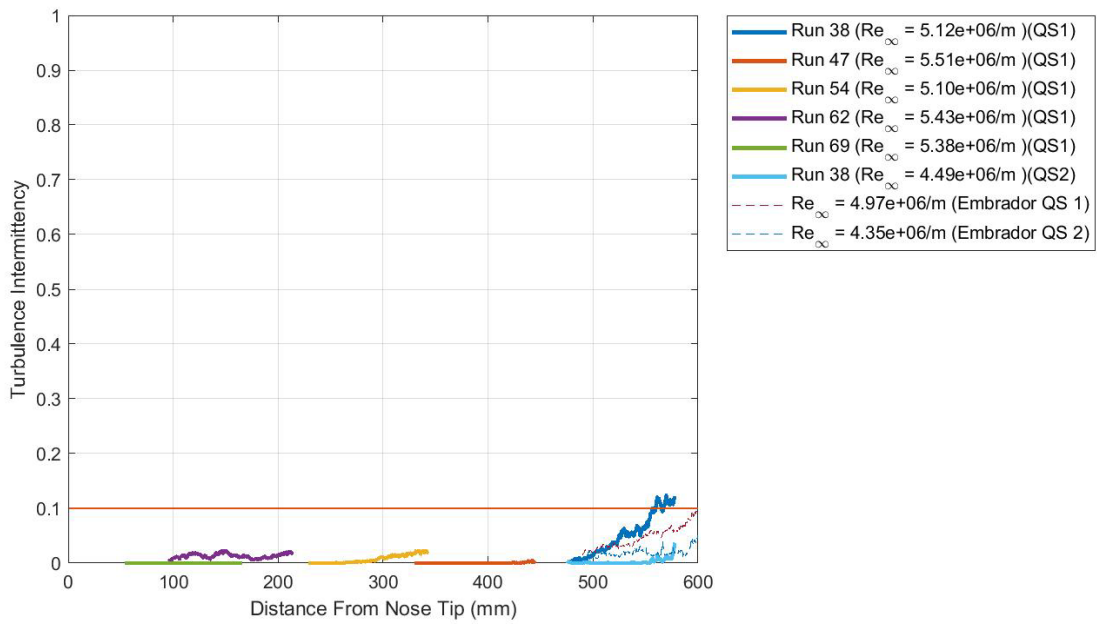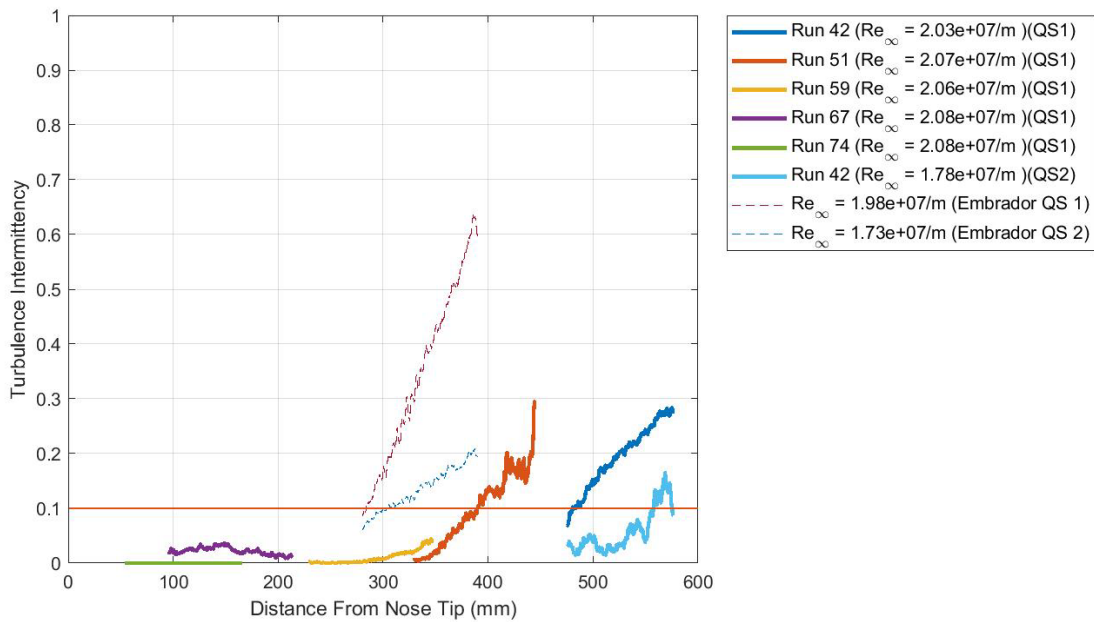
b) P_{DT} = 100 psi (.69 MPa)
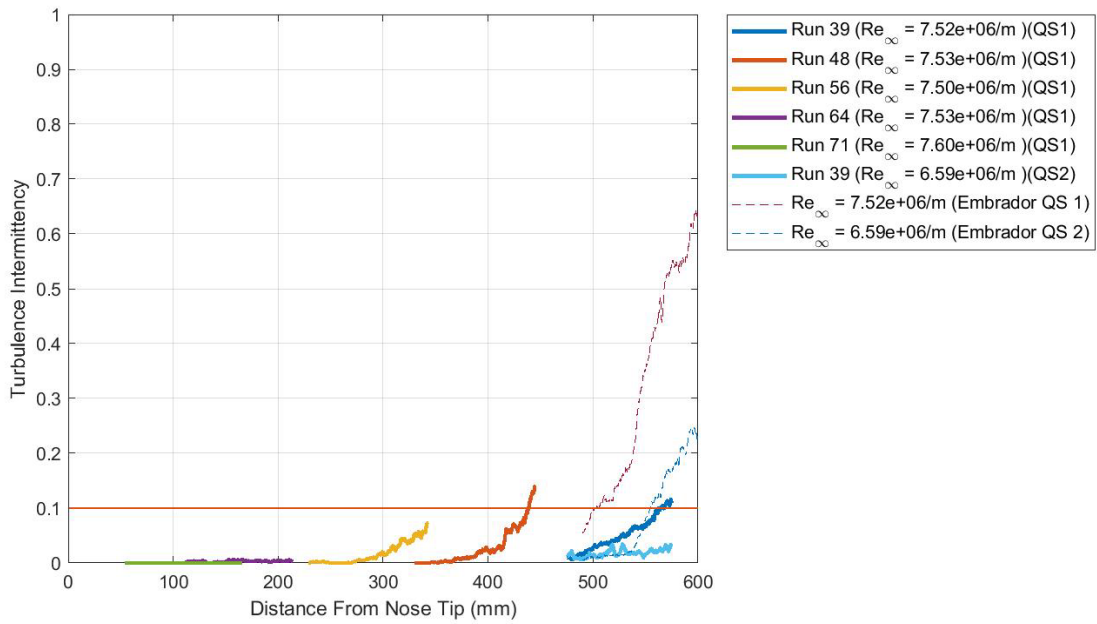
c) P_{DT} = 150 psi (1.03 MPa)

d) P$_{DT}$ = 200 psi (1.38 MPa)

e) P$_{DT}$ = 300 psi (2.07 MPa)

f) P$_{DT}$ = 400 psi (2.76 MPa)

g) P$_{DT}$ = 500 psi (3.44 MPa)

Figure 34: Turbulence Intermittency vs. Horizontal Distance from the Nose Tip for Cooled Experiments Re$_\infty$ = 2.6x10^6 – 2.6x10^7 /m, T$_w$/T$_0$ = .19 (T$_w$/T$_e$=1.40 ± 0.05)

a) P_{DT} = 50 psi (.34 MPa)

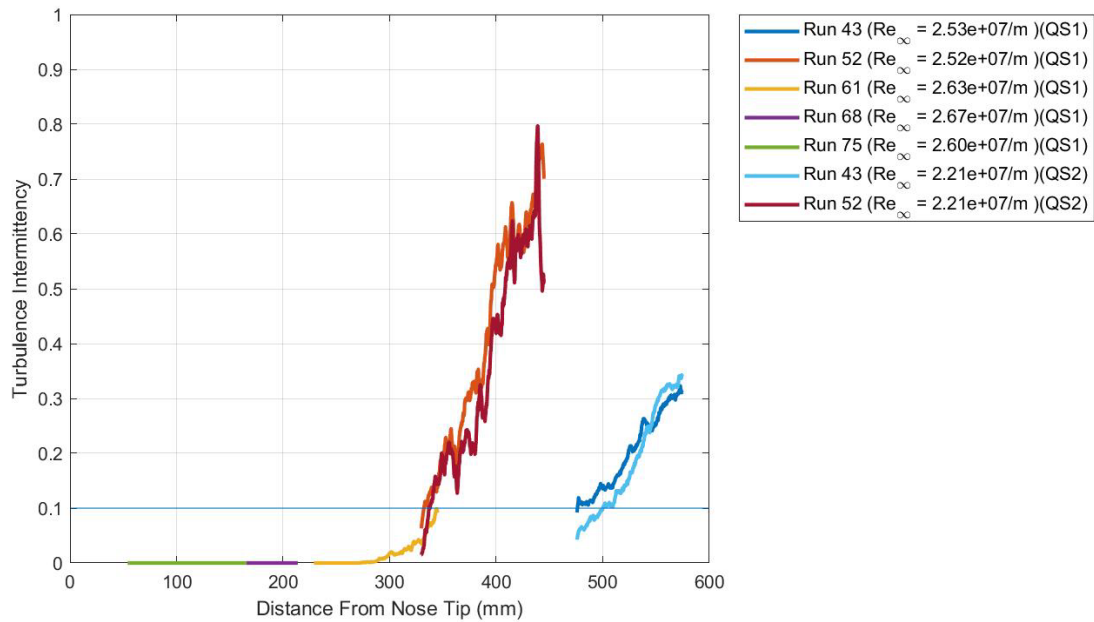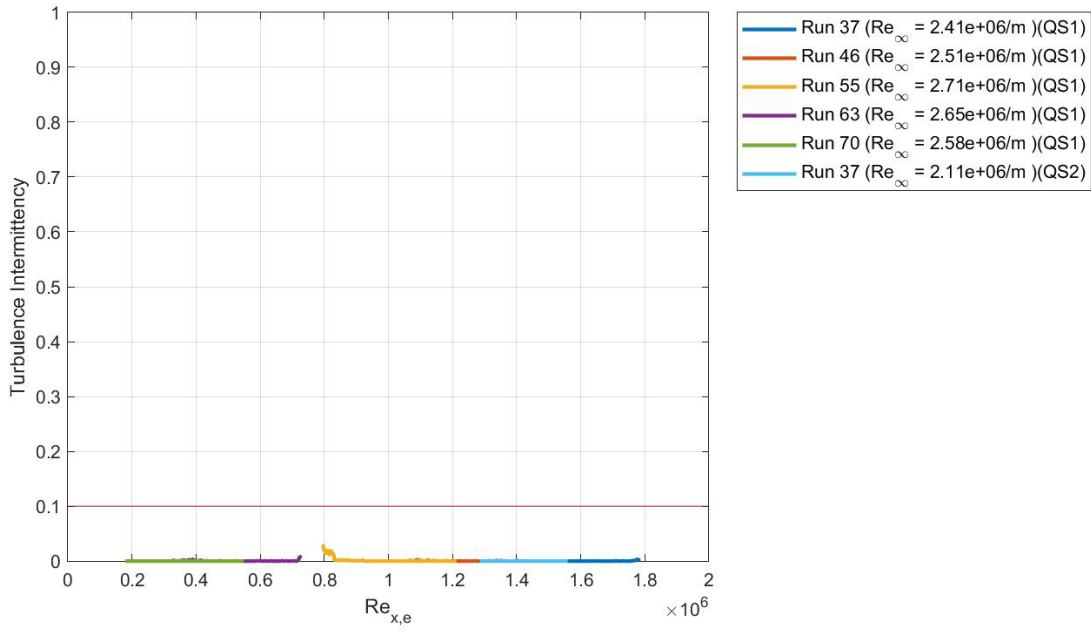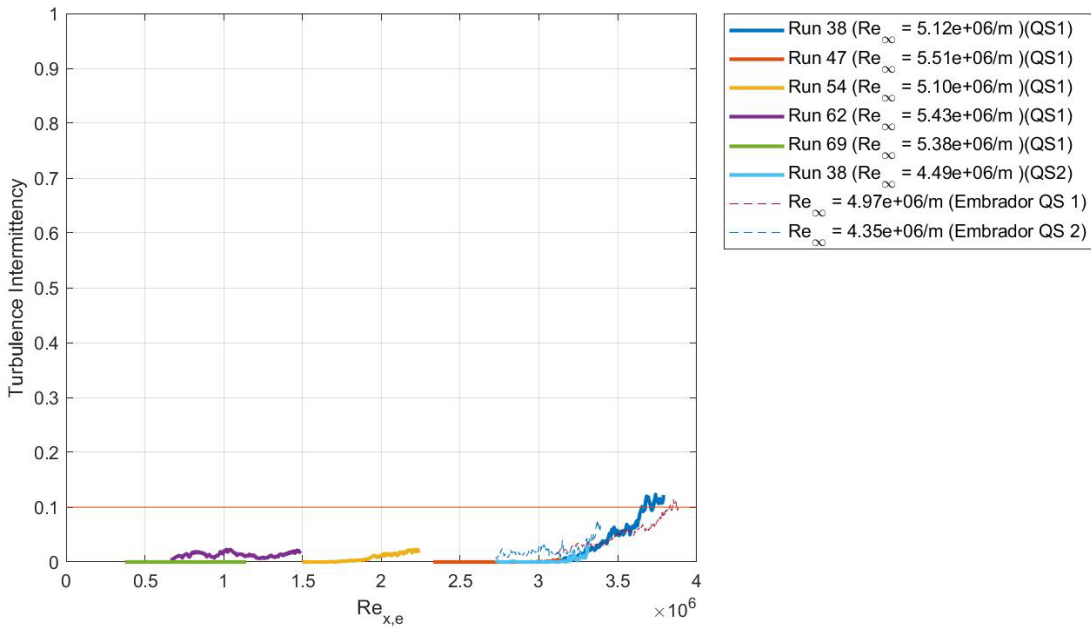b) P_{DT} = 100 psi (.69 MPa)
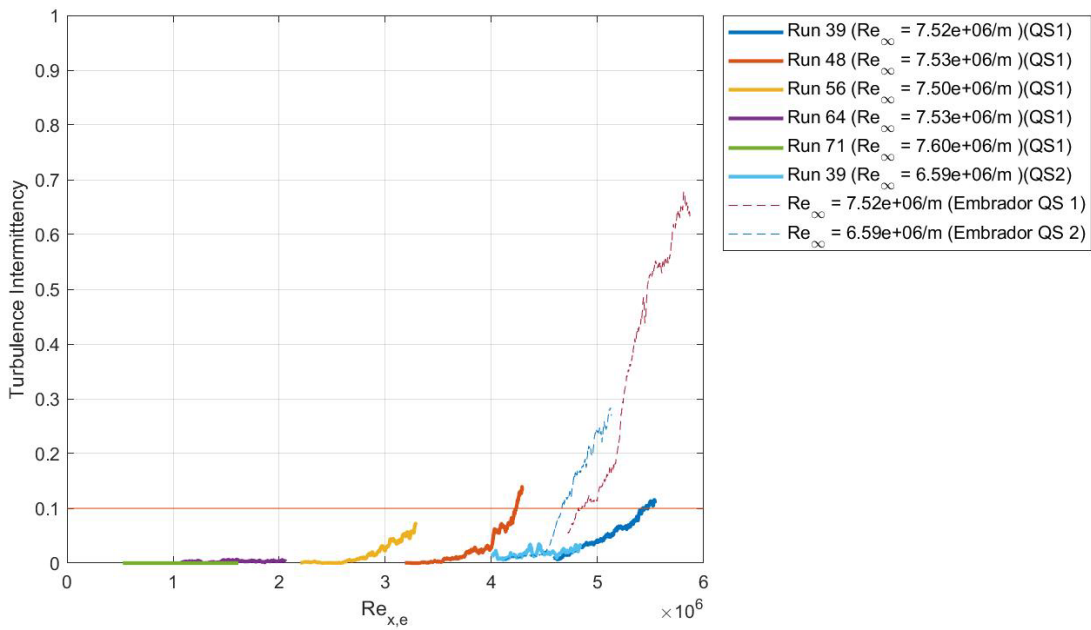
c) P_DT = 150 psi (1.03 MPa)

d) P_DT = 200 psi (1.38 MPa)

e) P$_{DT}$ = 300 psi (2.07 MPa)

f) P$_{DT}$ = 400 psi (2.76 MPa)

g) P_{DT} = 500 psi (3.44 MPa)

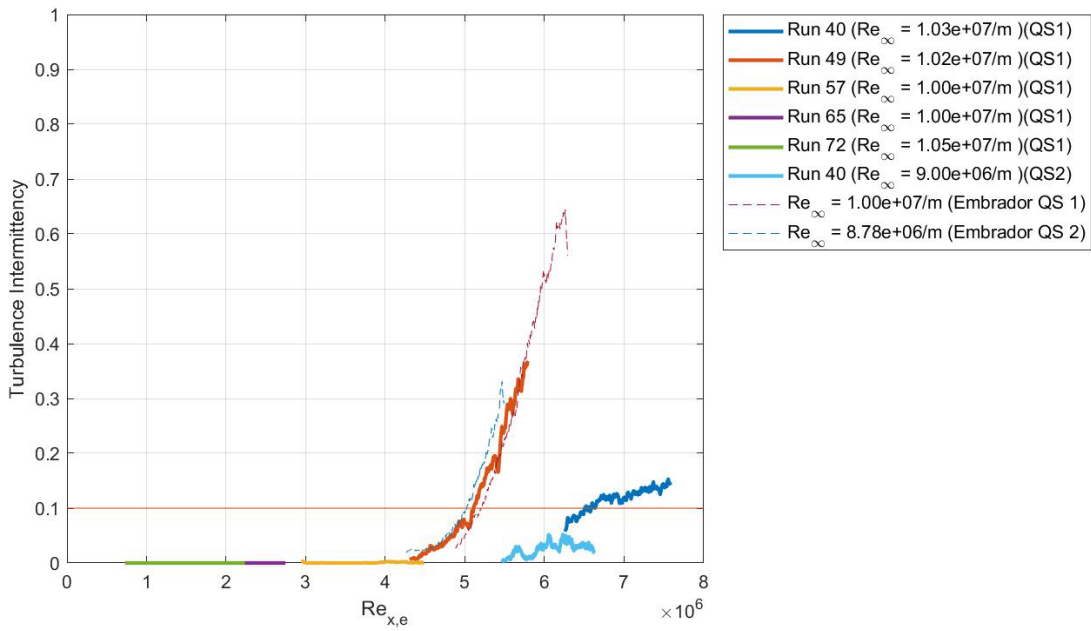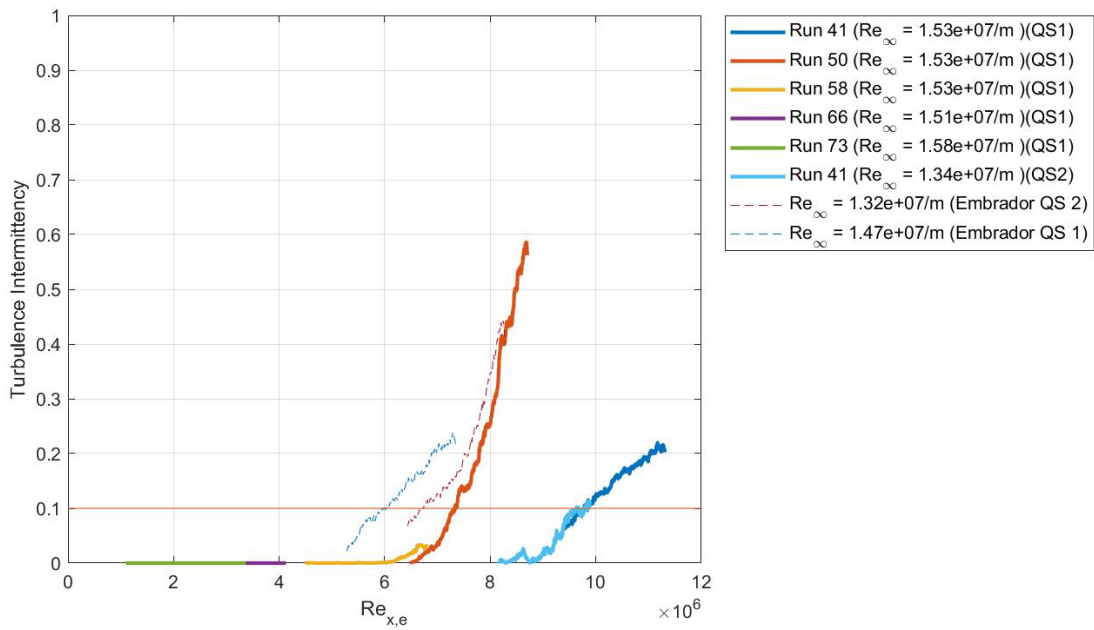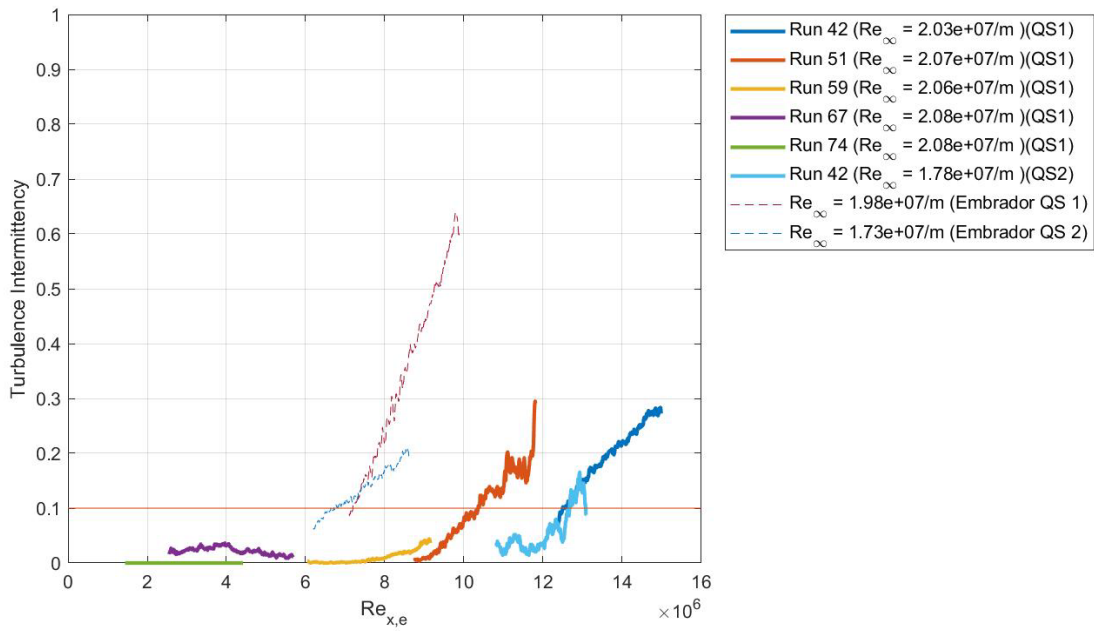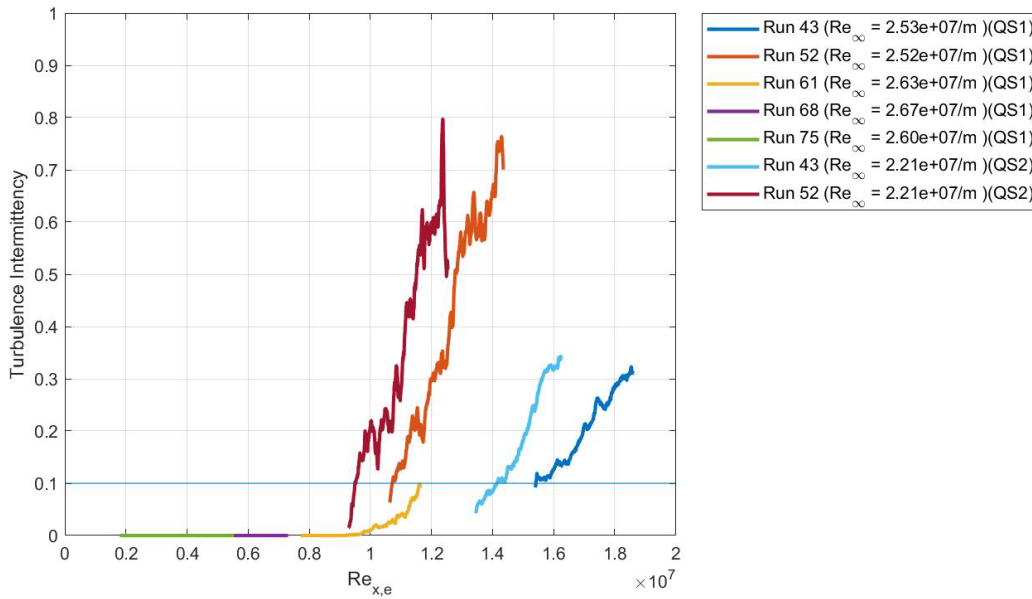Figure 35: Turbulence Intermittency vs. Local Reynolds Number for Cooled Experiments Re_∞ = $2.6 \times 10^6 - 2.6 \times 10^7$ /m, T_w/T_0 = .19 (T_w/T_e=1.40 ± 0.05)

The cooled-model experiments for initial driver tube pressures of 150 psia and over present a conundrum. Two different transition locations are apparent for similar driver tube pressures. Figure 36 presents sequential cooled surface Schlieren data for QS1 in runs 41 and 50 (the two most downstream locations, P_{DT}=300 psia). The observed differences in turbulence onset of the two states in different locations rules out a potential algorithmic cause. Additionally, differences in freestream unit Reynolds numbers cannot account for these differences, as the two separate transition locations still appear in the non-dimentionalized data presented in Figure 35. When combined with evidence of a discontinuity in the boundary layer thickness and uncooled transition data, it suggests best explanation for this is, as postulated in Section 4.1.2, that Runs 46-52 did not down to the appropriate temperature, but Runs 37-43 appeared to cool to sufficient levels. One

92

possibility was the formation of crystals in the LN2 line restricting the available flow in the later runs, but other possibilities also exist. Both sets of runs were operated of the same supply of LN2 in a dewar estimated to be suitable for 2 days' worth of runs. Runs 37-43 happened prior to Runs 46-52, so in addition to the possibility that vapor crystals forming in the transfer lines preventing full cooling, it is also possible that low supply of LN2 could have contributed to insufficient cooling causing early transition on some of the runs closer to scheduled dewar refilling.

a)   b)
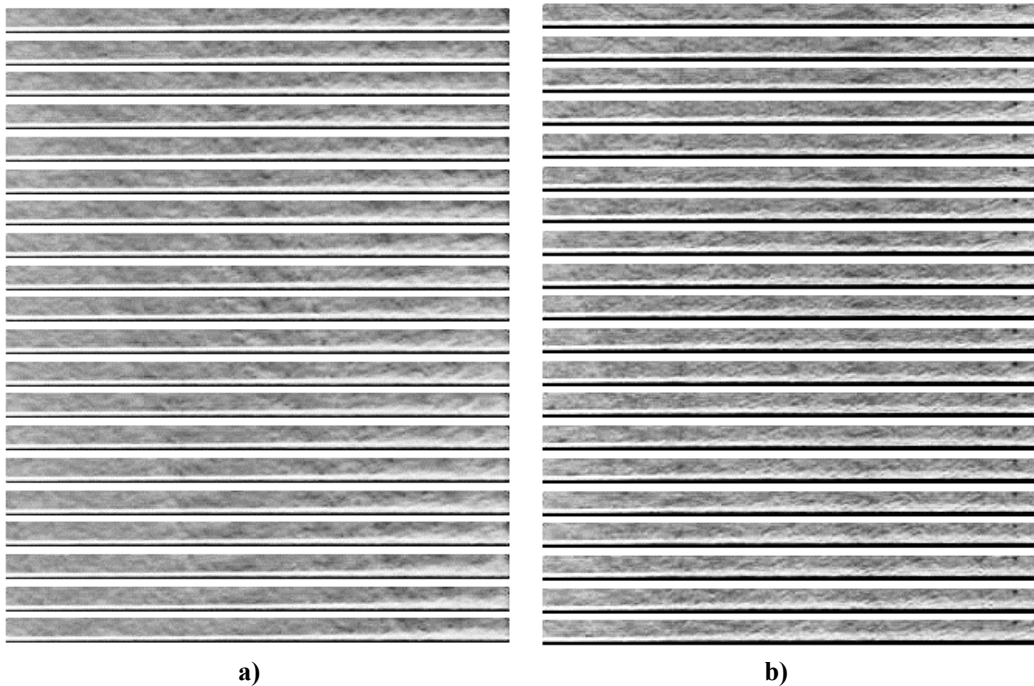
Figure 36: Qualitative Comparison Between Turbulence Intermittency Discontinuity, 20 Sequential Schlieren Images, P_{DT} = 300 psi Cooled (Target: T_w/T_e=1.40 ± 0.05) QS1 at a) Run 41 (x=476-578 mm) and b) Run 50 (x=330-445 mm)

Fortunately, the experiments conducted for the farthest downstream location for the farthest downstream location (Runs 37-43) for the cooled model showed intermittency levels crossing the 0.10 turbulence threshold, indicating a transition location. Notably, this was the first set of cooled runs utilizing a fresh tank of LN2. Examining the Schlieren video

data from this location confirmed laminar flow qualities that matched an expected cooled surface condition. Therefore, the data obtained in Runs 37-43 are trusted to represent best the desired cooled wall condition for the purposes of turbulence transition onset.

At 100 psia, it does show a slightly earlier transition on the blunt-tip case than on the sharp-tip case, but the intermittency level in the blunt-tip model just overcomes the 0.10 noise floor. An observed delay in transition begins to occur in the 150 psia case and higher pressures. From 150 psia and higher, the delay in transition onset location between the sharp-tipped cone and blunt-tipped cone then begins to increase with increasing freestream unit Reynolds numbers. While there is an observed trend that QS1 does generally have higher turbulence than QS2, both QS states approach a similar stabilization point at higher unit Reynolds numbers similar to the uncooled case. Overall, it was found that for both QS1 and QS2 that there existed a significant delay in turbulence transition between the sharp-tipped and blunt-tipped cooled cases, which is especially evident in the higher-pressure cases.

While more delayed than the uncooled cases, cooled QS1 and QS2 approach similar transition onset locations dimensionally and reach similar turbulence values at the highest tested freestream unit Reynolds numbers. In the uncooled case, swallowing length approximately coinciding with transition onset distance provided a theory for stability. However, there is a dearth of literature regarding the effects of surface cooling on entropy layer swallowing length for cones, other than occurring further up the cone than the uncooled case. The ability to ascertain swallowing length in the cooled case is not available with the given data.

4.4 Comparison of Transition Results – Uncooled vs. Cooled

Section 4.2 and 4.3 present data to allow for the comparison of effects of cooling between the sharp-tipped and blunt-tipped cones. As noted by Schnieder [12], a proper comparison between cooled and uncooled experiments must match freestream conditions and disturbance spectra between the experiments. All experiments take place at the same facility using the same driver tube pressures and methodologies. Therefore, freestream conditions between sets of experiments at similar driver tube pressures would remain constant. Additionally, the disturbance spectra of the overall tunnel flow would remain the same throughout all experiments where driver tube pressure remains fixed. Figure 37 shows a direct comparison of transition onset location of both the cooled and uncooled cases on the blunt-tipped cone at each initial driver tube pressure, with figures shown in order of ascending initial driver tube pressure.
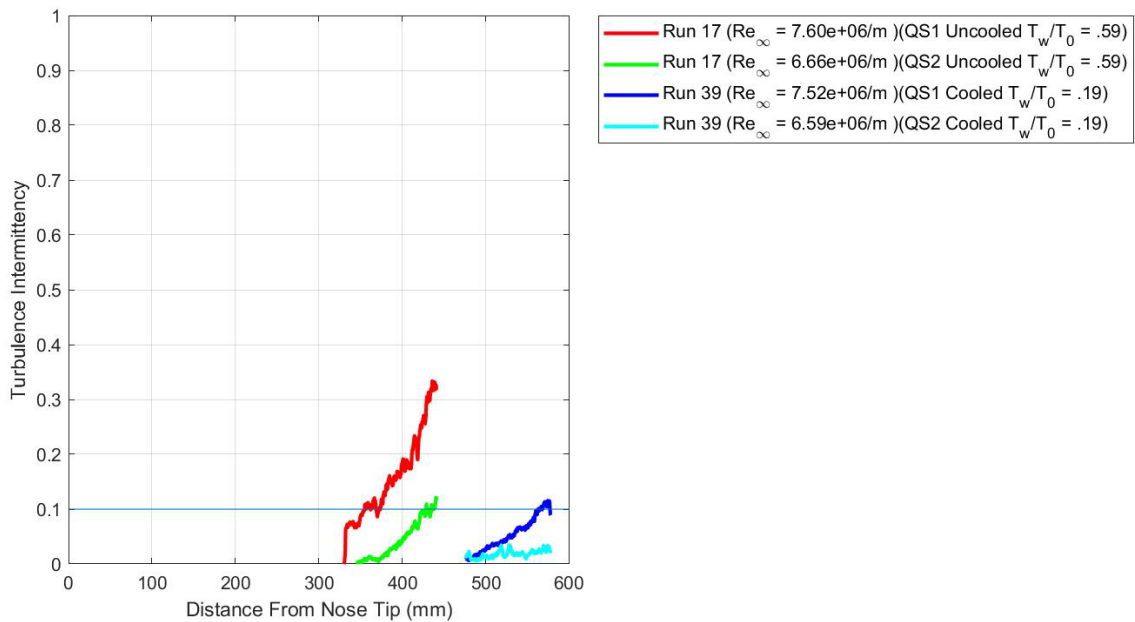
a) P_{DT} = 150 psia (1.03 MPa)

95
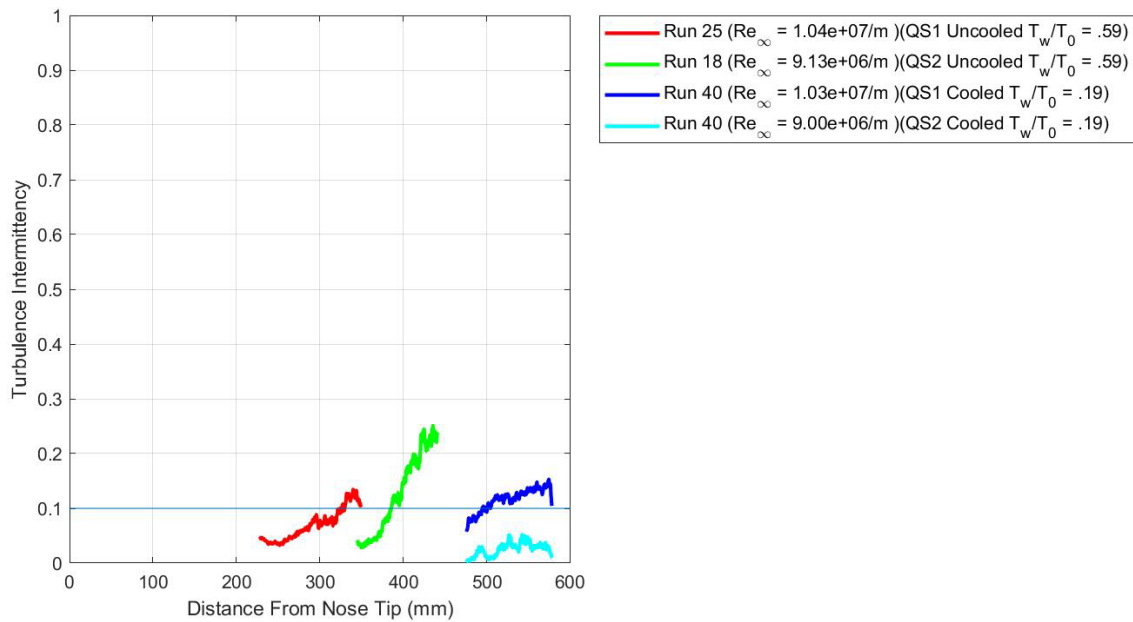
b) P$_{DT}$ = 200 psia (1.38 MPa)
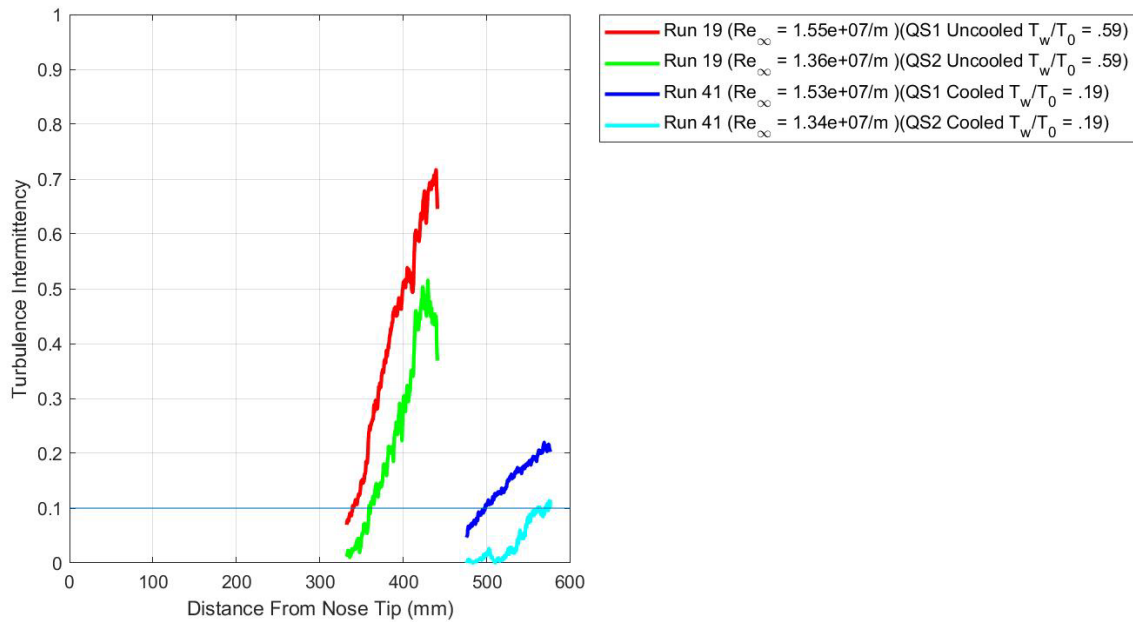
c) P$_{DT}$ = 300 psia (2.07 MPa)
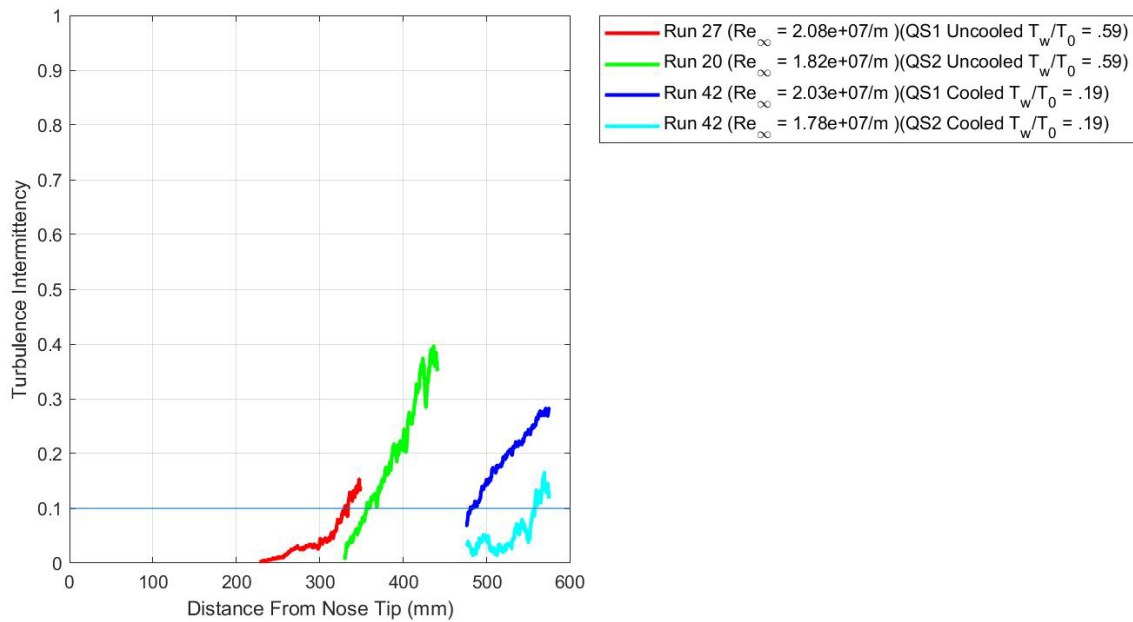
d) P_{DT} = 400 psia (2.76 MPa)

e) P_{DT} = 500 psia (3.44 MPa)

Figure 37: Comparison of Cooled (T_W/T_0 = .19) vs. Uncooled (T_W/T_0 = .59) Turbulence Transition Onset Locations for Blunt-Tipped Cone, P_{DT} = 150 - 500 psia
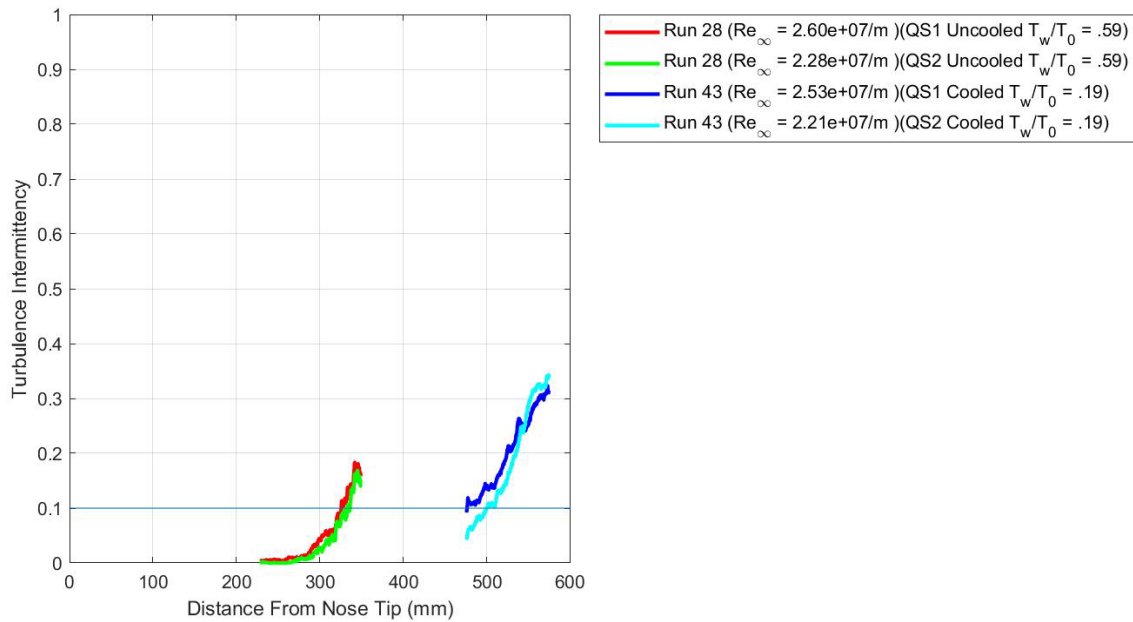
97

The transition onset location is then determined by examining the first instance of representative data where the turbulence intermittency values for each initial driver tube-pressure case first crosses the 0.10 threshold. Transition Reynolds number ($Re_{x,e,tr}$) is developed from the unit Reynolds number at the surface as estimated from the Taylor-Maccoll solution for the 7-degree half angle cone at a given freestream condition. This value for Reynolds number represents the Reynolds number at the edge of the boundary layer, and multiplying it by the distance at which transition onset occurs produces the transition Reynolds number.

This method calculated transition Reynolds numbers for both sharp and blunt-tipped cone cases. The approximated the blunt-tipped cone as a similar sharp-tipped cone so that sharp-tipped cone data was comparable. Transition onset occurred sufficiently far from the tip such that the shock wave above the transition location was approximately oblique. A Taylor-Maccoll solution approximates an inviscid edge condition for the blunt-tipped cone (which would normally require advanced techniques), allowing comparison to a sharp-tipped cone.

Figure 38 presents an overall comparison of transition Reynolds number against freestream unit Reynolds number for both the sharp and blunt-tipped cones. Red triangles for the sharp-tipped cone data and red circles for the blunt-tipped cone data denote the uncooled results. Blue triangles for the sharp-tipped cone data and blue circles for the blunt-tipped cone data denote the cooled surface results. The figure includes transition results for both QS1 and QS2, if transition occurred in the available data. The difference in QS states denotes whether the type of respective shape, with QS1 values receiving solid shapes and QS2 receiving shape outlines.

98
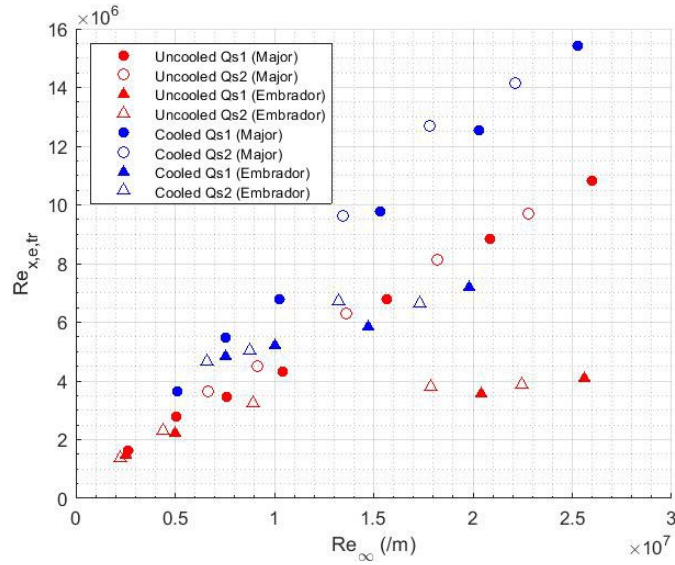
Figure 38: Transition Reynolds Number at the Boundary Layer Edge with Varying Freestream Unit Reynolds Number, Cooled (T_W/T_0 = .19) and Uncooled (T_W/T_0 = .59) Experiments for Both Sharp-Tipped (Embrador) and Blunt-Tipped (Major) Results

The figure concurs with the results of Sections 4.2 and 4.3 in that there is a measureable delay, especially at higher unit Reynolds numbers, between the sharp and blunted-tipped Reynolds numbers. Thus, the evidence demonstrates an observed greater impact on transition delay due to the combined effects of cooling and rounding the tip as compared to each individually. Additionally, transition Reynolds number for the blunt-tipped cone appears to be more linear with respect to unit Reynolds number than the sharp-tipped cone cases. One possible explanation is the interplay with the entropy layer swallowing distance. The stabilizing effect could be the reason that the transition onset location does not move upstream as drastically as the sharp-tipped case. This increases the transition Reynolds number with increasing unit Reynolds number. QS1 and QS2 do exhibit similar trends. QS2 transition data shows consistency with the data presented in

99

QS1, with both the uncooled and cooled data having both QS1 and QS2 transition Reynolds numbers occurring approximately within the same respective linear trend.
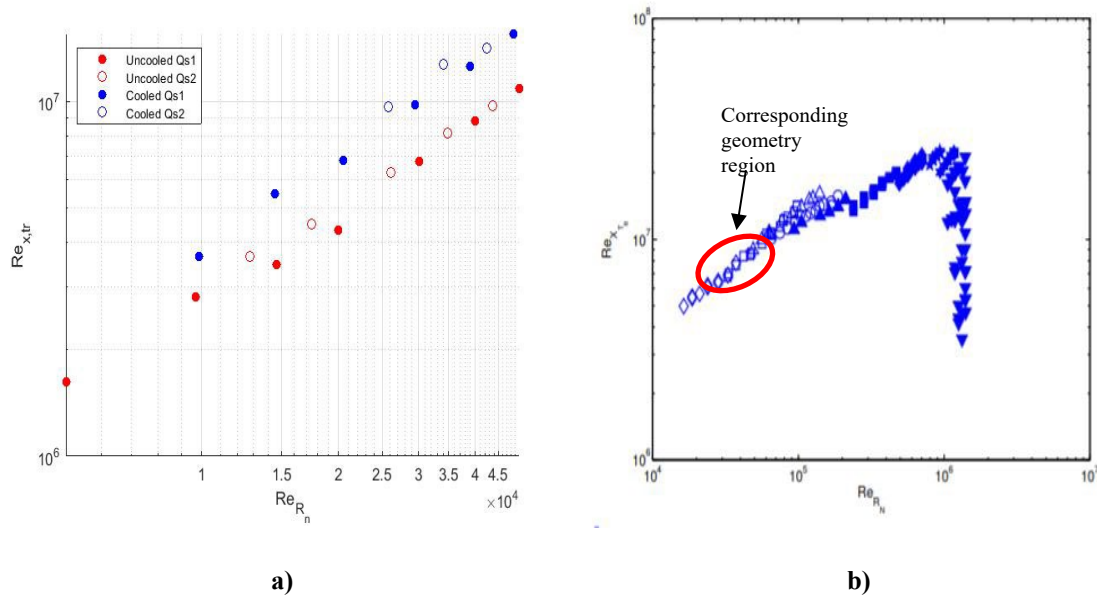
Figure 39: Freestream Transition Reynolds Number as a Function of Nose Tip Radius Reynolds Number, a) Current Results, R_n = 1.5 mm, b) Analysis from Stetson's Mach-6 Experiments (Uncooled Surface), With Identified Region R_n/R_b=0.02 [33].

These presented results do diverge from the trend established by the sharp-tipped case. The uncooled results do generally match past experiments for similar blunt-tipped cones of this radius. The results for freestream transition Reynolds number as a function of nose tip Reynolds number, as shown in Figure 39, agree with experimental evidence produced by Stetson for cones matching the current test article's base to nose tip radius ratio, at least in reference to the uncooled data [33]. In Figure 39, just as in previous figures, the blue circles stand for cooled data while red circles stand for uncooled data, all exclusively for the current blunt-tipped model.

4.5   Boundary Layer Instability Frequency Spectrum Analysis

At hypersonic speeds up to around Mach 14, in the sharp cone cases at zero-degree angle of attack Mack's second mode is the most dominant instability mechanism in the boundary layer [3]. Increasing nose bluntness up to the critical radius adds a stabilizing effect to boundary layer receptivity, shifting the overall frequency characteristics of instabilities [75]. Increasing nose bluntness additionally introduces wisp structures of increasing size as a possible instability mechanism within the boundary layer [59]. The analysis performed a cross-correlation for select Schlieren frames displaying sufficiently developed instabilities in the region where they are likely to cause transition. For cooled-surface conditions, this analysis utilized only the data that was the most trusted to represent the desired cooled wall condition.

Figure 40 shows an example of second mode instabilities present in the flow for both the cooled and uncooled cases. These figures exemplify the "rope-like" structure of these instability waves. These instabilities "ride" along the upper edges of the boundary layer. These instabilities appeared quite frequently in the uncooled flow, with an increase in appearance frequency approaching the transition location. However, these were not the sole cause of transition, as turbulence transition occurred sometimes without the observation of these instability waves. In the cooled flow, second mode instabilities appeared much less frequently. This could be a result of lack of spatial resolution to observe them due to low boundary layer thickness, rather than necessarily a suppression of second mode instabilities or them not being present.

Wisp structures, like those observed by Kennedy et al. [59], were less distinguishable in the flow at higher unit Reynolds numbers and in cooled surface

conditions. The work by Kennedy et al. predicted that the nose radius of the current test article would not develop many significant wisp structures. Some instabilities resembling the expected wisps appeared occasionally in the uncooled tests, such as the one exemplified in Figure 27 or in interaction with the boundary layer as seen in Figure 41. However, no wisps appeared in cooled-surface condition data.
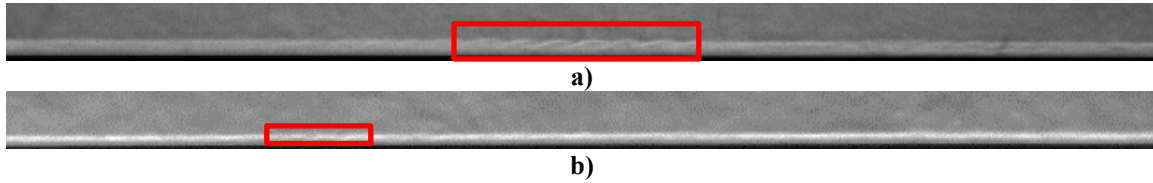

a)

b)

Figure 40: Example of Rope-Like Second Mode Waves Traveling Left-to-right, P_{DT} = 200 psia for a) Uncooled Run 25 (Viewing Window 2, x=229-349 mm) and b) Cooled Run 40 (Viewing Window 1, x=476-578 mm)

Figure 41: Wisp Structure Interacting with the Boundary Layer Traveling Left-to-Right, Uncooled Run 25 (Viewing Window 2, x=229-349 mm) P_{DT} = 200 psia

Some limitations prevented universal identification of instability waves in all Schlieren data obtained for each run. As previously stated, if the boundary layer was too thin due to cooling, high freestream unit Reynolds numbers, or some combination of the two, pixel resolution was insufficient to determine whether instability waves existed at given frame in the composition of the boundary layer.

For both cooled and uncooled runs, identification of boundary layer instability waves occurred for frames from viewing windows close to the onset of transition with sufficiently thick boundary layers to discern flow details. Uncooled surface conditions near transition onset typically exhibited laminar boundary layers thick enough for this purpose.

Figure 42 shows an example of a second mode instability transitioning across the boundary layer into an oncoming transition onset location in 0.3 μsec intervals. Second mode waves observed grew as they progressed down the boundary layer. The "rope-like" features that identified these instabilities grew more pronounced as they traveled. The growth of these features provides evidence that these instabilities within the boundary layer are a cause of a natural growth transition.
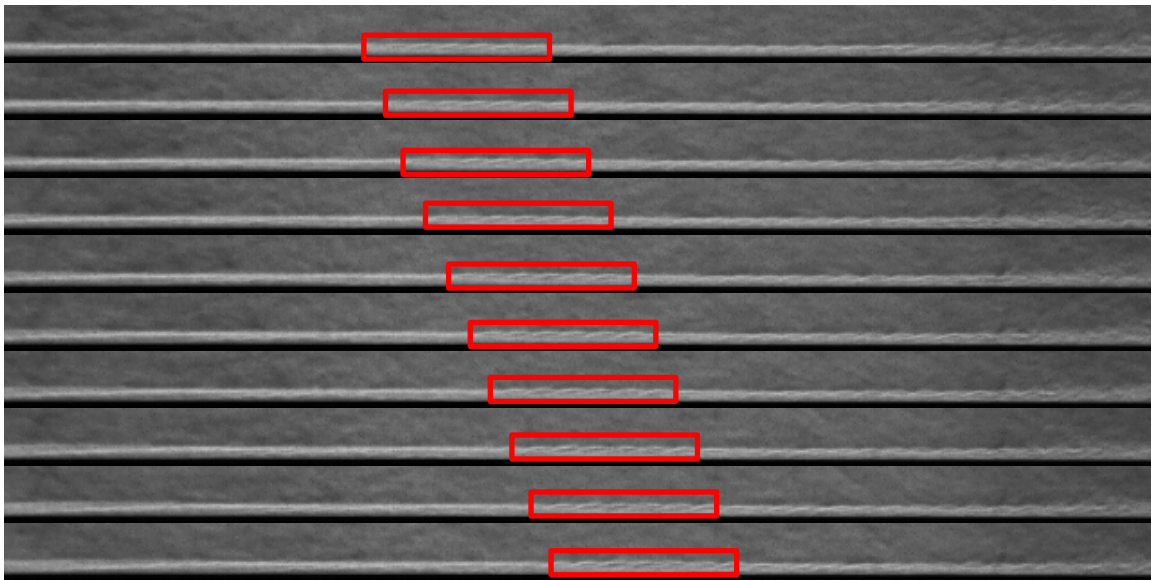
Figure 42: Mack's Second Mode Instabilities (Red Boxes) Flowing (From Left-to-Right) into Turbulence Transition Onset for Uncooled Run 27 (x=229-349 mm), P_{DT} = 400 psia

Given the Schlieren data, a cross-correlation between frames found the wave propagation velocities of these instabilities. The cross-correlation technique employed a wave speed-finding algorithm, which applied an FFT between frames to calculate the speed at which these disturbances travel along the boundary layer. This algorithm calculated that the second mode waves traveled at an average of about 749 m/s and the observed wisps traveled at about 650 m/s. This compares to an estimated freestream velocity in QS1 of about 899 m/s. The second mode instability wave-speed does match measurements taken

by Hill for similar instabilities at this same facility [76]. Nose bluntness of the article does impart some speed delay due to the frequency shift imparted on the boundary layer instabilities.

To find the frequency characteristics of each type of instability a spatial Fast Fourier Transform (SFFT), as described in Section 2.10 and Section 3.7.1, was performed focusing on frames where each type of instability mechanism was present in the flow. These occurred over both cooled and uncooled test runs, and a power spectrum diagram (PSD) represented the data. The PSD identifies dominant frequency characteristics of desired flow features through predominant local maximum points on the figure. Instabilities were taken from windows where onset to transition turbulence first begins for driver tube pressures of 200, 300, and 400 psia in both QS1 and QS2 of the uncooled case. An analysis of multiple pressures provided insight of how the instabilities change over a range of unit Reynolds numbers. A low pixel resolution contributing to observed disturbances, if present, being less identifiable resulted in only one pressure condition analyzed for the cooled case. Figure 43 shows the resulting PSD results for second mode instabilities in both cooled and uncooled cases. PSD plots for the wisps showed no relative frequency peaks when attempted, possibly indicating that the sampling frequency of the data was not sufficient to capture frequency information of the disturbance.

A comparison of the second mode instabilities presented in Figure 43 yields several conclusions. First, as initial driver tube pressure is increased, the observed peak frequency of the second mode instabilities also increases. Additionally, the peak frequency also increases during the transition from QS1 to QS2 at a given driver tube pressure. While the first of these observations agree with the peak frequency data obtained by Embrador [10],

the second observation contrasts with observations for the sharp cone data. The sharp cone data presented that QS2 peak frequency decreased from that found in QS1.
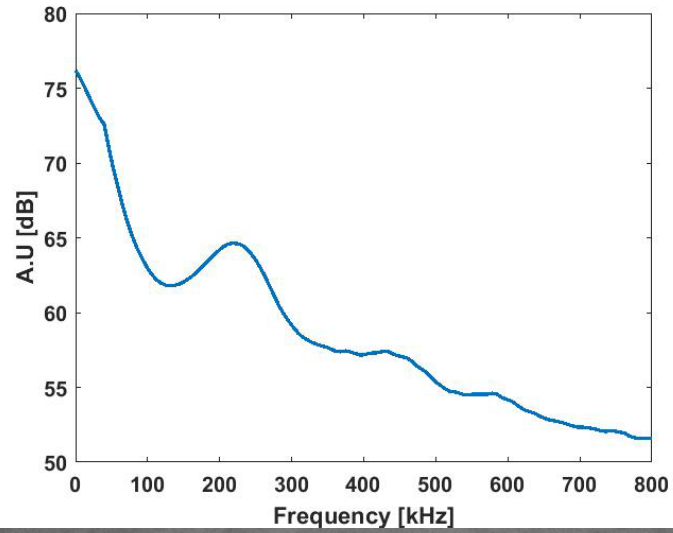
a) PSD plot for Uncooled Run 25 (x=229-349 mm) QS1 Second Mode, P_{DT} = 200 psia, peak frequency = 223 kHz
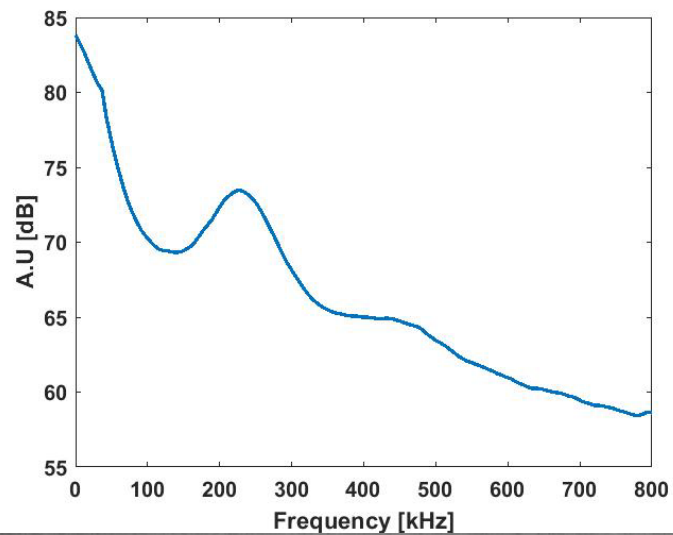
b) PSD plot for Uncooled Run 26 (x=229-349 mm) QS1 Second Mode, P_{DT} = 300 psia, peak frequency = 226 kHz
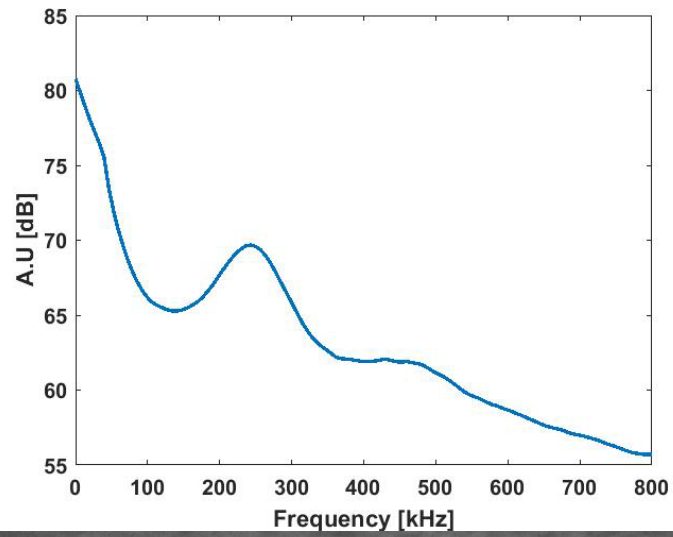
c) **PSD plot for Uncooled Run 27 (x=229-349 mm) QS1 Second Mode, P_{DT} = 400 psia, peak frequency = 243 kHz**
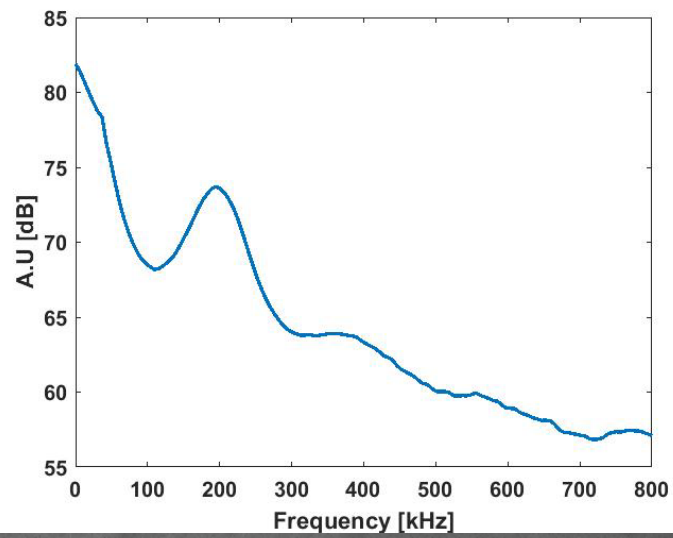
d) **PSD plot for Uncooled Run 18 (x=330-441 mm) QS2 Second Mode, P_{DT} = 200 psia, peak frequency = 195 kHz**

106

e) **PSD plot for Uncooled Run 19 (x=330-441 mm) QS2 Second Mode, P_{DT} = 300 psia, peak frequency = 215 kHz**
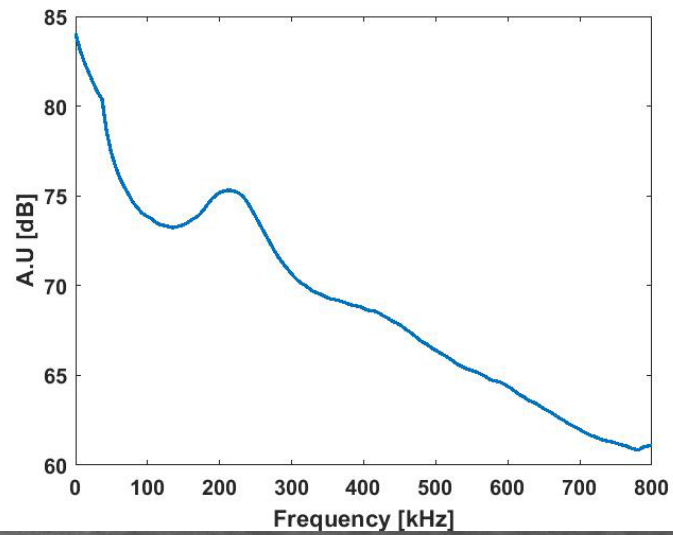
f) **PSD plot for Uncooled Run 20 (x=330-441 mm) QS2 Second Mode, P_{DT} = 400 psia, peak frequency = 214 kHz**
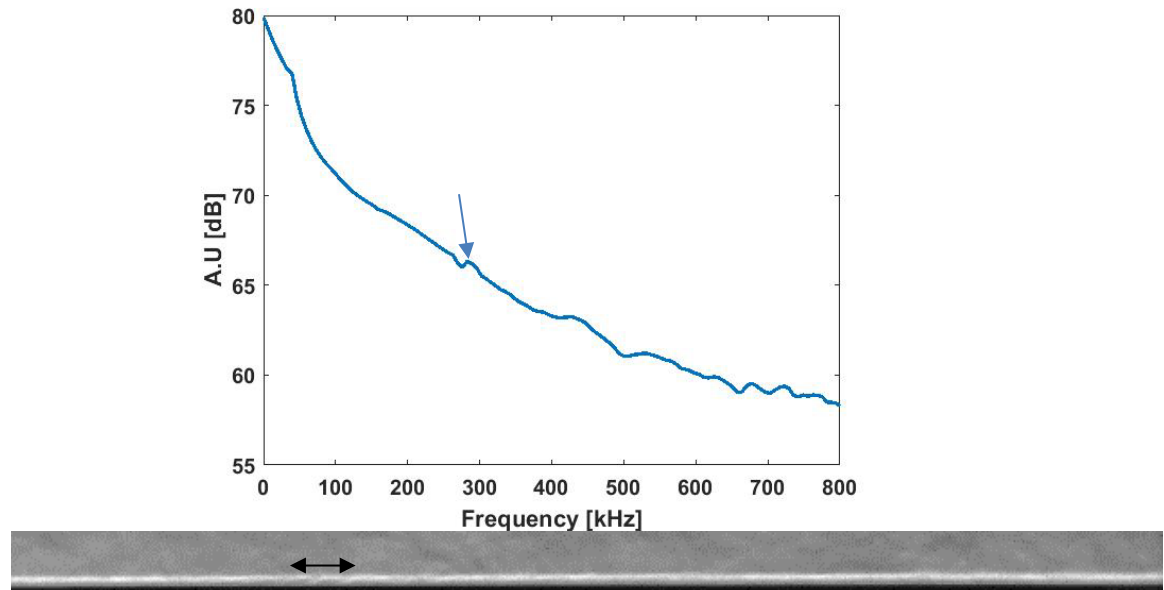
g) **PSD plot for Cooled Run 40 (x=476-578 mm) QS1 Second Mode, P_{DT} = 200 psia, peak frequency = 289 kHz**

Figure 43: PSD Plots For Second Mode Instabilities On a Blunt-Tip Cone with Peak Frequencies for QS1 vs. QS2 and Cooled Vs. Uncoooled Surfaces Near Transition Onset, Flow in Images Travels Left-to-Right
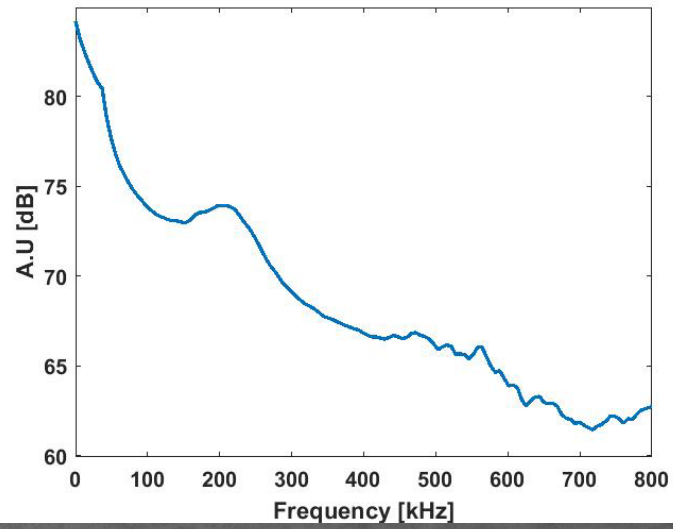
For the Figure 43(g), the peak frequency of the second mode instabilities during the cooled surface conditions increased significantly compared to uncooled second mode instabilities under similar freestream conditions. However, in qualitatively examining the Schlieren data, second mode and wisps do not distinctly appear in the flow as frequently as the uncooled cases. The low spatial resolution of the boundary layer itself could be a factor, but could possibly correlate to a suppression of the instabilities leading to the relative low intensity value of the peak dominant frequency.

V. Summary

Boundary layer transition measurements were executed at the Air Force Research Laboratory (AFRL) Mach-6 Ludweig Tube wind tunnel using a spherically blunted 7-degree half-angle cone with a nose tip radius of 1.5 mm. The purpose of this study was to observe the effects of surface cooling on boundary layer transition and characteristics on the blunted-tipped cone, and then compare those results to previously obtained data for a similar, sharp-tipped cone geometry previously investigated by Embrador [10]. These tests both employed single piece cones with internal cavities for cooling. Circulating LN2 into the test article provided cooling prior to testing.

Experiments on the new model included the characterization of two surface conditions. The uncooled surface condition kept the model at a constant 298 K with a wall-temperature ratio of $T_w/T_0 = 0.59$ ($T_w/T_e = 4.35 \pm 0.15$). Circulating LN2 in the internal cavity of the model under vaccum for around 110 minutes to achieve thermal equilibrium achieved the cooled-wall condition for testing. At thermal equilibrium, the model exhibited a maximum temperature at the tip of 128 K (temperature ratio of $T_w/T_0 = 0.26$), and a minumum temperature at the nose base of 83 K (temperature ratio of $T_w/T_0 = 0.17$). The average temperature measured across the surface, 95 K (temperature ratio of $T_w/T_0 = 0.19$, $T_w/T_e = 1.40 \pm 0.05$), characterized the surface condition.

During wind tunnel testing, two periods of quasi-steady state flow per run, each lasting for about 0.1 seconds, defined the Mach-6 flow conditions of the tunnel. The two periods, refered to as the first quasi-steady state (QS1) and the second quasi-steady state (QS2), were the main intervals of study during wind tunnel operation. QS1 and QS2 do exhibit some differences in flow conditions, namely pressure losses between QS1 and QS2.

Experiments surveyed an order of magnitude of freestream unit's Reynolds numbers (Re_∞ = $2.7x10^6$ – $2.7x10^7$ /m) for both cooled and uncooled surface conditions, determined by the set initial driver tube pressure ranging from 50 psia to 500 psia.

Schlieren visualization, paired with a high-speed camera, captured the hypersonic boundary layer data at a framerate of 600,000 fps and a shutter speed of 0.16 µsec. Several viewing windows were characterized the boundary layer across the length of the test article closely matching the viewing windows used by Embrador during the sharp-tipped cone experiments. Vibrations from the tunnel on the Schlieren set-up during QS2 caused light intensity variations that made the ability to remove noise from the boundary layer during that period inconsistant for large ammounts of frames. So while every run condition offered 2000 frames of schlieren data, QS2 data focused on viewing windows where transition onset was qualitatively seen to begin. In these windows, an average of about 1000 Schlieren frames represented good QS2 data that mitigated the effects of light intensity variation.

120-L LN2 dewar connected to the internal cavity suplied the necessary cooling to the test model. The circulation operated by a system of insulated crygenic hoses attached to the base of the cone, eventually venting outside the laboratory. Care was taken so that tunnel air during cooled runs contained minimal moitsture content. This was done through maintaining a vaccuum condition of 0.02 psia or less and running dry air through the tunnel once before cooling. Some cooling errors occurred during test runs such that the upstream conditions, while cooled somewhat, did not fully reach the desired thermal condition. This error surfaced only upon data analysis.

Viewing windows closely matched the viewing windows selected by Embrador. Schlieren data captured flow details in these regions, with particular focus payed on viewed

regions with an observed onset to turbulence transition. Data analysis for both cooled and uncooled conditions output turbulence intermittency statistics and instability frequencies according to procedures outlined by Casper et al. [69] and Jagde et al. [70], respectively. Turbulence intermittency calculations identified transition regions and provided a comparison between the cooled and uncooled conditions on the blunt-tipped model and to past data from the sharp-tipped model. Frequency characteristics of instability waves also offered a comparison between models and surface temperature conditions.

5.1 Key Findings

5.1.1 Transition Onset Delay

Switching model geometries and creating cooled surface conditions delayed the onset of transition. For the current blunt-tipped model, there was a delay in onset to transition between uncooled surface conditions ($T_w/T_0 = .59$) and cooled surface conditions ($T_w/T_0 = .19$). Other current studies support these results of a delay in transition due to cooling [50]. Shifting to QS2 from QS1 also delayed transition dimentionally, but these differences began to converge on location with rising freestream unit Reynolds number. In addition, the higher freestream unit reynolds numbers observed produced increasingly small differences dimentionally in transition onset location. Based on models of expected entropy swallowing length, the entropy layer was anticipated to have a stabilizing effect on boundary layer transition.

For both cooled and uncooled surface conditions, blunt-tipped cone data presented a clear delay in transition onset compared to the sharp-tipped cone data. Morkovin described that the combination of cooling and rounding the tip might not always lead to an

additive combinatory effect in delaying transition in flight tests; however, the present experiment showed that rounding the tip and cooling the surface with regard to delaying transitiononset did combine to increase delay even further [28]. Plotting freestream unit Reynolds number against transition Reynolds number at the edge of the boundary layer vividly visualized the difference in delay between the test conditions. The transition Reynolds number for the blunt-tipped cone also appeared to increase more rapidly with respect to freestream unit Reynolds number than similar data for the sharp tipped cone. QS2 largely matched trends in transition Reynolds number exhibited by QS1.

5.1.2   Instability Frequency Differences

The two main instability waves identified during flow conditions on the blunt-tipped model were wisps and Mack's second mode instabilities. These instabilities traveled at an average of about 749 m/s for second mode waves and about 650 m/s for the wisps. This is in comparison to a predicted 899 m/s freestream velocity. Wisp-shaped waves were clearly present in the Schlieren frames but did not provide enough signal to register a peak in the spatial FFTs, possibly implying that they are not a dominant characteristic of the flow. Power Spectrum Diagrams (PSD) analyzed dominant frequency characteristics of observed instabilities across several pressure conditions on the uncooled surface condition, in QS1 and QS2, and then compared to a cooled surface condition.

 As initial driver tube pressure increased, the peak frequency of the second mode instabilities increased. Additionally, peak frequency also increased during the transition from QS1 to QS2 at a given driver tube pressure. While the first of these observations agree with the peak frequency data obtained by Embrador for the sharp-tipped cone data [10], the second observation contrasts to observations for the sharp-tipped cone.

The peak frequency of the second mode instabilities during the cooled surface conditions increased significantly compared to uncooled second mode instabilities under similar freestream conditions. However, in qualitatively examining the Schlieren data, second mode and wisps do not distinctly appear in the flow as frequently as the uncooled cases. The low spatial resolution of the boundary layer itself could be a factor, but could possibly correlate to a suppression of the instabilities leading to the relative low intensity value of the peak dominant frequency.

5.2   Recommendations and Future Work

Improvements to the experimental set-up could be of use for future work on similar research efforts. First, it would be of great interest to future research to fix vibrational issues with the Schlieren set-up due to tunnel operation. This would allow more Schlieren data collected later in the run, particularly QS2, to be of equal or similar quality to that taken during QS1 for better comparisons of boundary layer features. Secondly, implementing a method of confirming surface temperature prior to running would be helpful. Especially in cases where runs and data collection are days apart, visual identification of data differences can be difficult. A way to confirm surface temperature would allow spotting of issues like low levels of LN2 or possible cryogenic line blockage early. Additionally, the Schlieren set-up could see general improvements. Improvements could include light quality, reduction of beam elongation, improving spatial resolution, or improvement of knife-edge alignment methods for more consistent lighting intensity in the data.

More research into the interplay of entropy swallowing length and the boundary layer is needed. There is a dearth of available data on entropy layer swallowing length in a

cooled surface condition, other than that it moves downstream. An investigation into entropy layer dynamics with the boundary layer in cooled conditions could prove of value in showing causal links between entropy layer swallowing length and boundary layer transition in blunt-tipped cones.

In addition, noise characterization of the flow in the AFRL Ludweig Tube needs further investigation into the causes of transition. While this work observes a delay in transition, there still is not established a direct causal link for the transition. Therefore, further work into both noise characterization of the facility and transition mechanisms in cooled surface conditions could be warranted.

Appendix A: Cone Set-up

Table 5: Parts for Cone Model Assembly Line

| Part Description	Material	Size	Ultimate Tensile Strength	Torque	Number Required
Flanged Hex Head Screw	18-8 Stainless Steel	5/16"-18 1 1/4" Long	170,000 psi	10 ft-lbs.	8
Square Head Cup-Point Set Screw	316 Stainless Steel	3/8"-16 1" Long		Wrench-tight	4
Cryogenic Relief Valve (P_s=100psia)	316 Stainless Steel PCTFE Seal	1/4" NPT	N/A	Wrench-tight	1
FEP Encapsulated Steel Spring Core	316 Stainless Steel FEP Jacket	3.99 mm Cross-section 113.03 mm ID	N/A	N/A	1
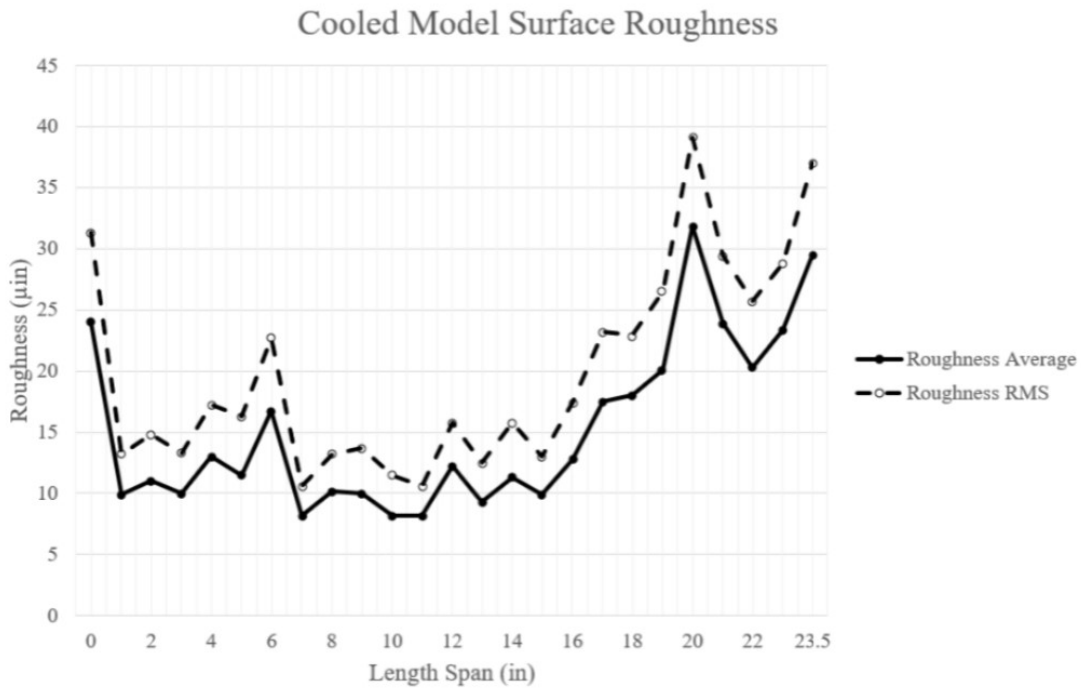
Figure 44: Average and Root-Mean-Squared Roughness for the cone employed in experiments by Oddo and Embrador [9]
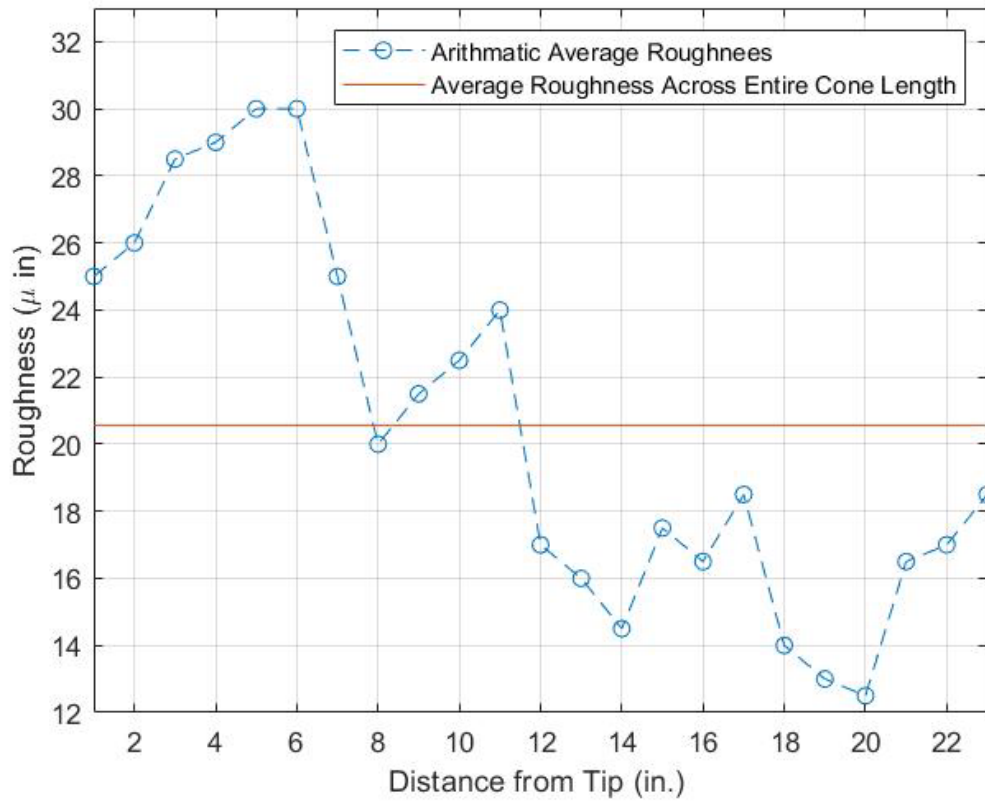
Figure 45: Roughness Report for Average Roughness at Different Stations Along the Length of the Rounded Tip Cone
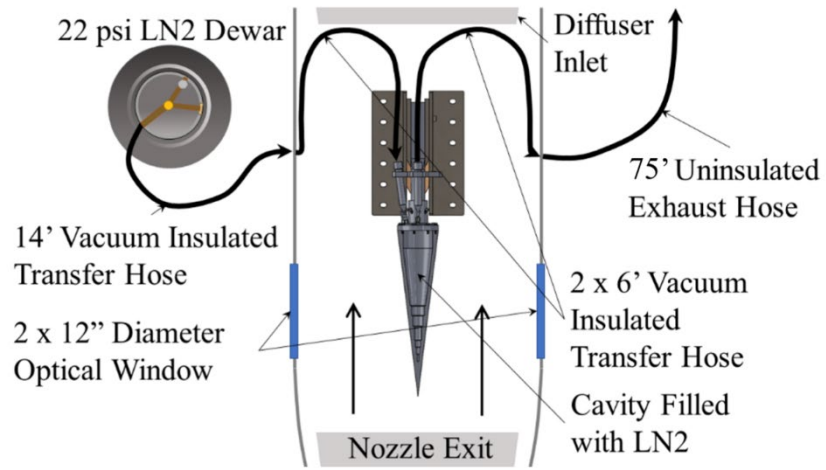
Appendix B: Cryogenic System

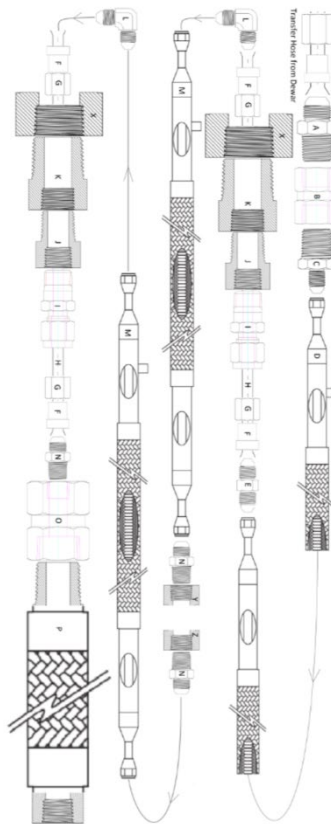**Figure 46: Full Schematic of Cryogenic Cooling System**

Figure 47: Schematic of Cryogenic Transfer Line

Table 6: Parts for Cryogenic Line

Part Letter	Part Description	Material	Size
A	Male 37° Flare – Male NPT Straight Adapter	316 Stainless Steel	0.5-inch Flare, 0.5-inch NPT
B	Female NPT – Female NPT Hex Coupling	316 Stainless Steel	0.5-inch NPT, 0.5-inch NPT
C	Male NPT – Male 37° Flare Straight Adapter	Zinc-Plated Steel	0.5-inch NPT, 0.25-inch Flare
D	Vacuum Insulated Transfer Hose – Braided Exterior	Stainless Steel	0.25-inch ID, 1.2-inch OD, 14-foot length, 0.25-inch Flared ends
E	Male 37° Flare – Male 37° Flare Straight Adapter	Zinc-Plated Steel	0.25-inch Flare, 0.25-inch Flare
F	Ferule for 37° Flared Steel Tubing	316 Stainless Steel	For 0.25-inch OD Tubing
G	Nut for 37° Flared Steel Tubing	316 Stainless Steel	For 0.25-inch OD Tubing
H	Steel Tubing	Stainless Steel	0.25-inch OD, 0.20-inch ID, 6-inch length
I	Compression Fitting for Steel Tubing, Male NPT, Middle Bored Out	316 Stainless Steel	0.25-inch NPT, For 0.25-inch OD Tubing, 0.25-inch OD Bore
J	Male NPT – Female NPT, Bushing Reducer Adapter	PTFE	0.375-inch NPT, 0.25-inch NPT
K	Male NPT – Female NPT, Bushing Reducer Adapter	PTFE	0.75-inch NPT, 0.375-inch NPT
L	Male 37° Flare – Male 37° Flare 90° Elbow Adapter	316 Stainless Steel	0.25-inch Flare, 0.25-inch Flare
M	Vacuum Insulated Transfer Hose – Braided Exterior	Stainless Steel	0.25-inch ID, 1.2-inch OD, 6-foot length, 0.25-inch Flared ends
N	Male 37° Flare – Male NPT Straight Adapter	316 Stainless Steel	0.25-inch Flare, 0.25-inch NPT
O	Female NPT – Female NPT Hex Reducing Coupling	316 Stainless Steel	0.75-inch NPT, 0.25-inch NPT
P	Uninsulated Transfer Hose – Braided Exterior – Male NPT, Female NPT	Stainless Steel	1.2-inch OD, 48-foot length, 0.75-inch NPT, 0.75-inch NPT
X	Ludwieg Tube Access Port	Carbon Steel	0.75-inch NPT
Y	Test Article Flow Inlet	303 Stainless Steel	0.25-inch NPT
Z	Test Article Flow Outlet	303 Stainless Steel	0.25-inch NPT

Appendix C: Cooling and Defrost Data from Oddo and Embrador

Cooling Test #1

Figure 48: Results of Oddo Two Diode Cooling Test #1 on a Sharp-Tipped Cone Model [9]
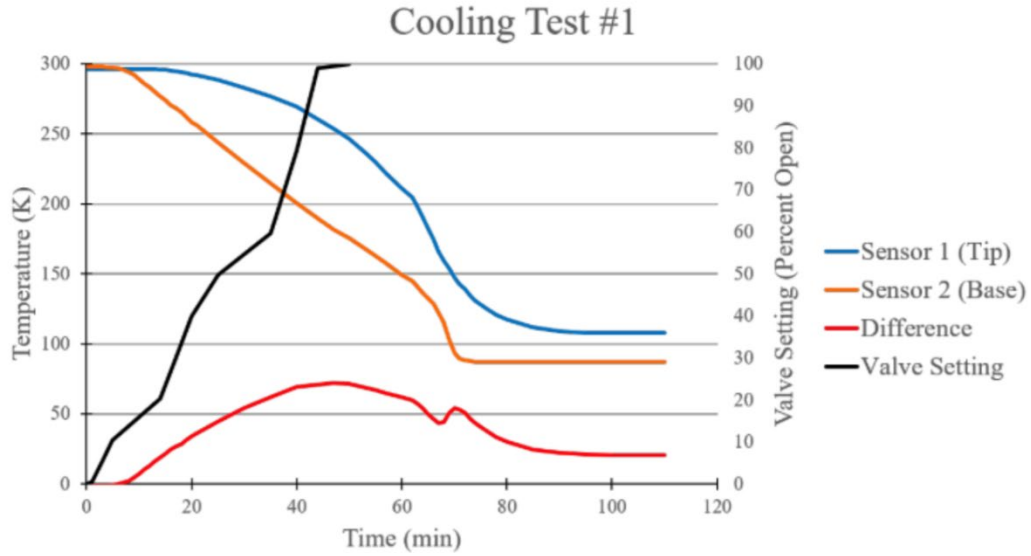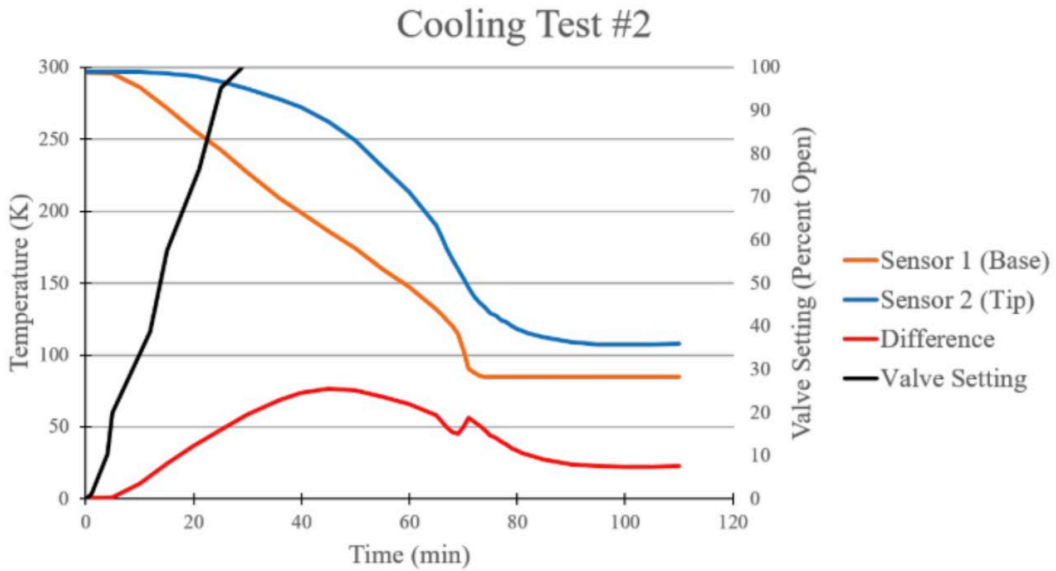
Cooling Test #2

Figure 49: Results of Oddo Two Diode Cooling Test #2 on a Sharp-Tipped Cone Model [9]
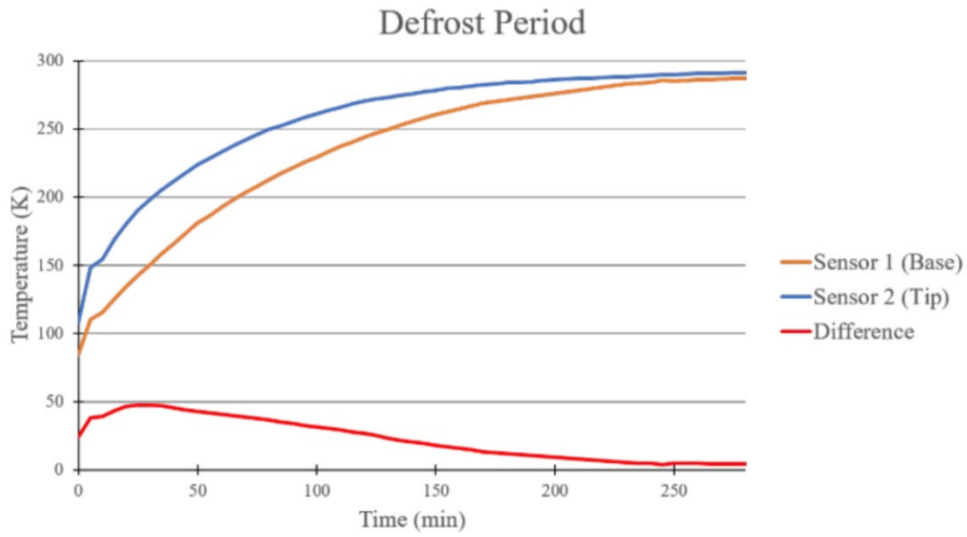
Figure 50: Results of Oddo Two Diode Defrost Test on a Sharp Tipped Cone Model [9]
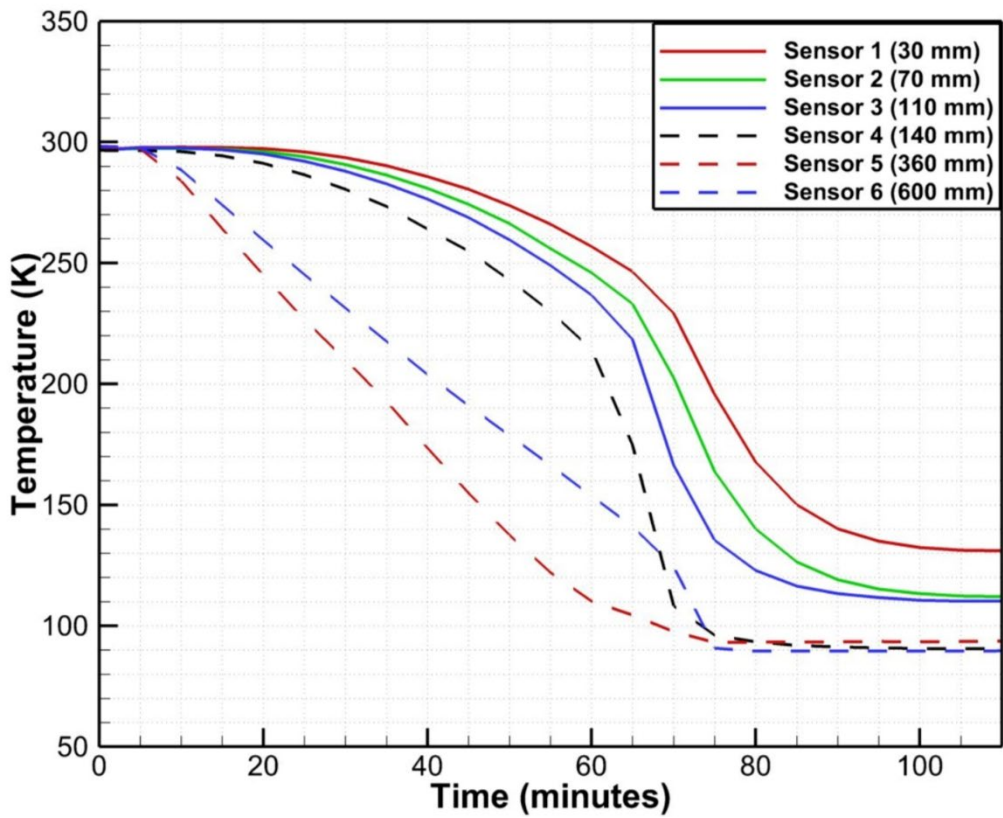

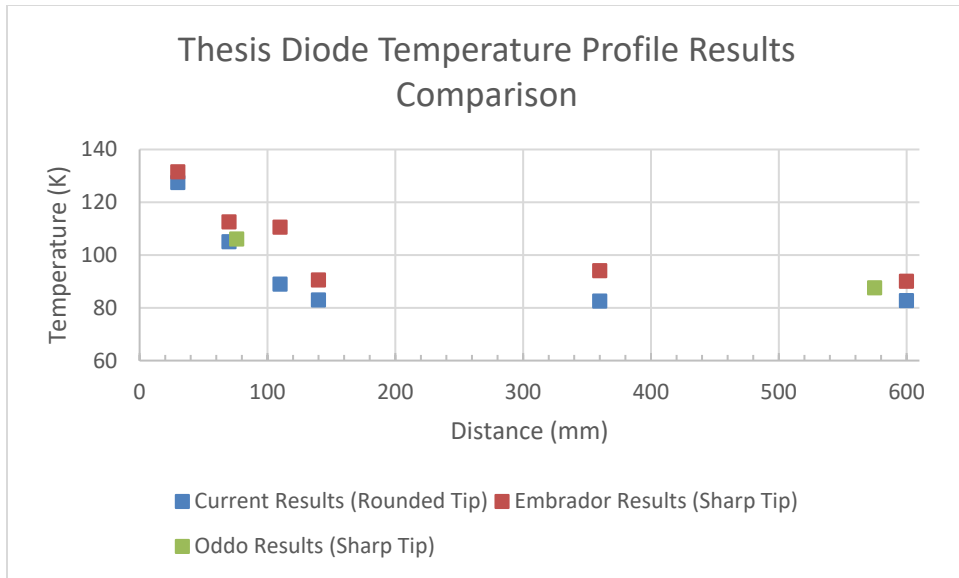**Figure 51: Results of Embrador Six Diode Cooling Test on a Sharp-Tipped Model [10]**

Figure 52: Comparison of Minimum Surface Temperature Distributions Over Varying distances Across the Cone Measured from the Tip

Appendix D: Full Run Schedule and Notes

Camera Settings for all runs:

FPS – 600000

Shutter Speed - .16 μs

Resolution – 640x32 pixels

Table 7: Uncooled Run Schedule

Uncooled Runs			
Run # (Sequential Order)	Aimed Driver Tube Pressure (psia)	Actual Driver Tube Pressure (psia)	Notes
Viewing Window #5 (Range: 52-163 mm from cone tip) on 9/22/21			
1	50	66.562	
2	100	96.599	
3	150	147.692	
4	200	197.732	
5	300	294.767	
6	400	399.723	
7	500	500.946	
Viewing Window #4 (Range: 96-208 mm from cone tip) on 9/22/21			
8	50	48.981	
9	100	96.012	
10	150	151.11	
11	200	200.467	
12	300	299.274	
13	400	399.978	
14	500	499.966	
Viewing Window #2 (Range: 330-441 mm from cone tip) on 9/23/21			
15	50	54.197	Viewing Window 2 was performed before Viewing Window 3
16	100	97.437	
17	150	146.629	
18	200	200.825	
19	300	299.849	

20	400	400.358	
21	500	498.67	
Viewing Window #3 (Range: 229-349 mm from cone tip) on 9/23/21			
22	50	49.074	
23	100	94.147	
24	150	146.288	
25	200	200.437	
26	300	302.071	
27	400	401.648	
28	500	501.122	
Viewing Window #1 (Range: 482-572 mm from cone tip) on 9/24/21			
29	50	50.357	
30	100	94.652	
31	150	146.355	
32	200	200.515	
33	300	301.485	
34	400	401.477	
35	500	499.805	

Table 8: Cooled Run Schedule

Cooled Runs			
Run # (Sequential Order)	Aimed Driver Tube Pressure (psia)	Actual Driver Tube Pressure (psia)	Notes
Viewing Window #1 (Range: 476-578 mm from cone tip) on 10/19/21			
36	200	193.582	Uncooled Dummy run to remove Water Vapor
37	50	46.504	
38	100	98.751	
39	150	145.083	
40	200	198	
41	300	295.616	
42	400	391.513	
43	500	487.063	
44	100	106.704	Comparison run after completion of

			1st 7 cooled runs to compare/discover any noticeable change over the course of running (No noticeable difference)
Viewing Window #2 (Range: 330-445 mm from cone tip) on 10/21/21			
45	200	200.044	Uncooled Dummy run to remove Water Vapor
46	50	48.465	
47	100	106.179	
48	150	145.237	
49	200	196.769	
50	300	295.727	
51	400	399.623	
52	500	485.402	LN2 refill was performed after this run.
Viewing Window #3 (Range: 229-349 mm from cone tip) on 10/25/21			
53	50	195.976	Uncooled Dummy run to remove Water Vapor. New dewar was implemented from this point on due to a valve becoming loose during refilling.
54	100	98.441	
55	50	52.283	
56	150	144.568	
57	200	193.542	
58	300	294.955	
59	400	397.147	
60	500	495.681	Bad save, camera was turned off so file was not properly saved

61*	50	55.976	Uncooled Dummy run to remove Water Vapor. Performed on 10/26/21.
62	500	507.715	Performed on 10/26/21.
Viewing Window #4 (Range: 96-214 mm from cone tip) on 10/27/21			
63*	400	400.000	Uncooled Dummy run to remove Water Vapor
64	100	104.641	
65	50	51.141	
66	150	145.178	
67	200	193.198	
68	300	290.498	
69	400	400.444	
70	500	514.522	LN2 Refill was performed after this run
Viewing Window #5 (Range: 54-166 mm from cone tip) on 10/28/21			
71*	400	300.000	Uncooled Dummy run to remove Water Vapor.
72	100	103.821	
73	50	49.785	
74	150	146.559	
75	200	202.855	
76	300	305.469	
77	400	400.956	
78	500	502.133	

*Run Data not recorded for runs marked with this

Table 9: Pixel Scales for Each Viewing Window (Measurement Uncertainty for each direction included)

Cooled vs. Uncooled	Viewing Window	Horizontal Pixel Scale (Pixels/mm) (±5 mm)	Vertical Pixel Scale (Pixels/mm) (±.1 mm)
Uncooled	5	5.7658	5.3286
Uncooled	4	5.7143	4.9734
Uncooled	3	5.3046	5.3286
Uncooled	2	5.7658	5.1510
Uncooled	1	7.1111	5.3286
Cooled	1	6.2992	5.5062
Cooled	2	5.5993	5.1510
Cooled	3	5.3046	4.9734
Cooled	4	5.3046	5.3286
Cooled	5	5.7593	5.5062

Appendix E: Boundary Layer Thickness Data
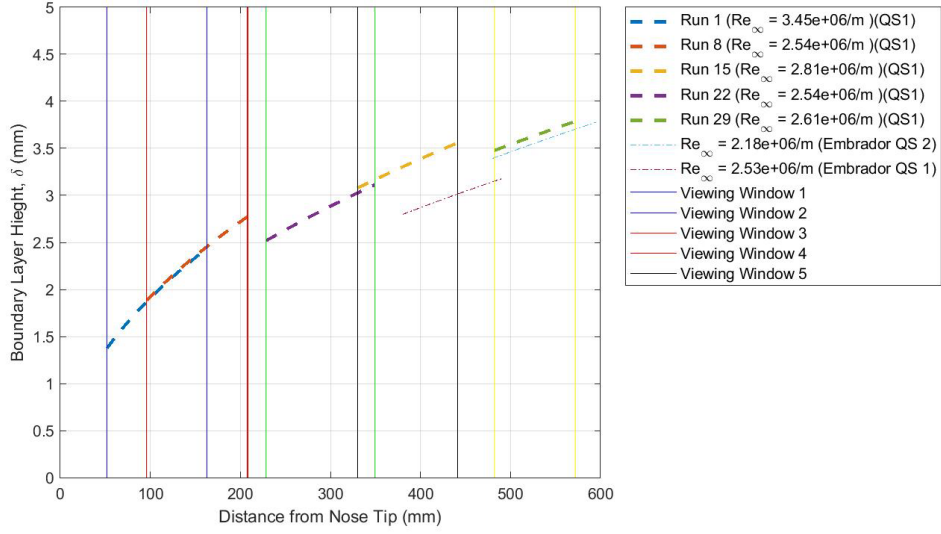
Uncooled Data

Figure 53: Laminar Boundary Layer Thickness for Uncooled Experiments at P$_{DT}$ = 50 psi, T$_w$/T$_0$ = .59 (T$_w$/T$_e$=4.35 ± 0.15)
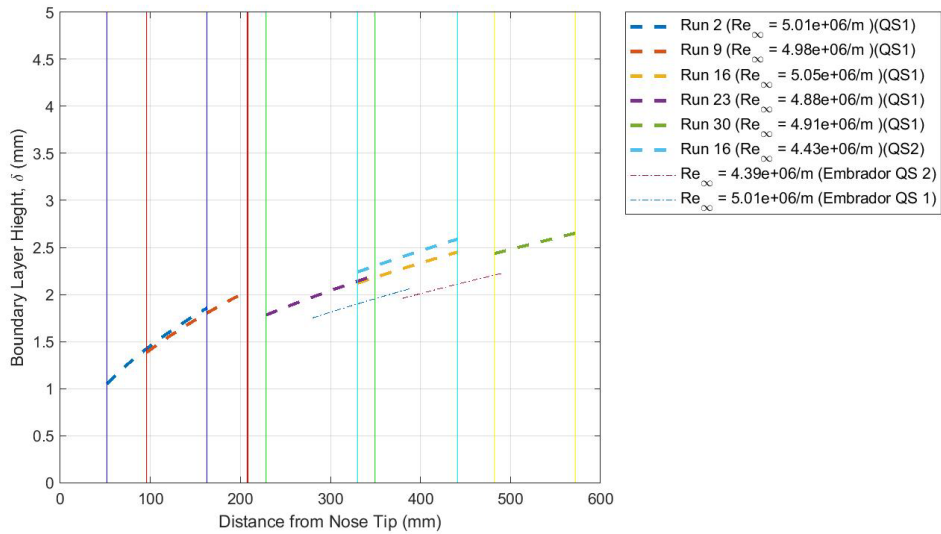

Figure 54: Laminar Boundary Layer Thickness for Uncooled Experiments at P$_{DT}$ = 100 psi, T$_w$/T$_0$ = .59 (T$_w$/T$_e$=4.35 ± 0.15)
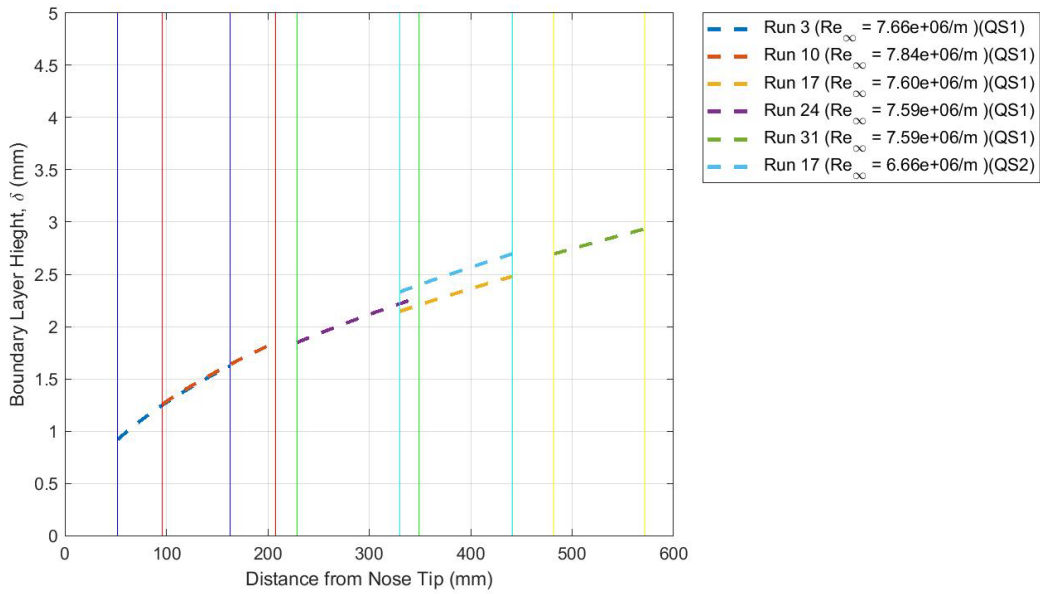
Figure 55: Laminar Boundary Layer Thickness for Uncooled Experiments at $P_{DT} = 150$ psi, $T_w/T_0 = .59$ ($T_w/T_e = 4.35 \pm 0.15$)
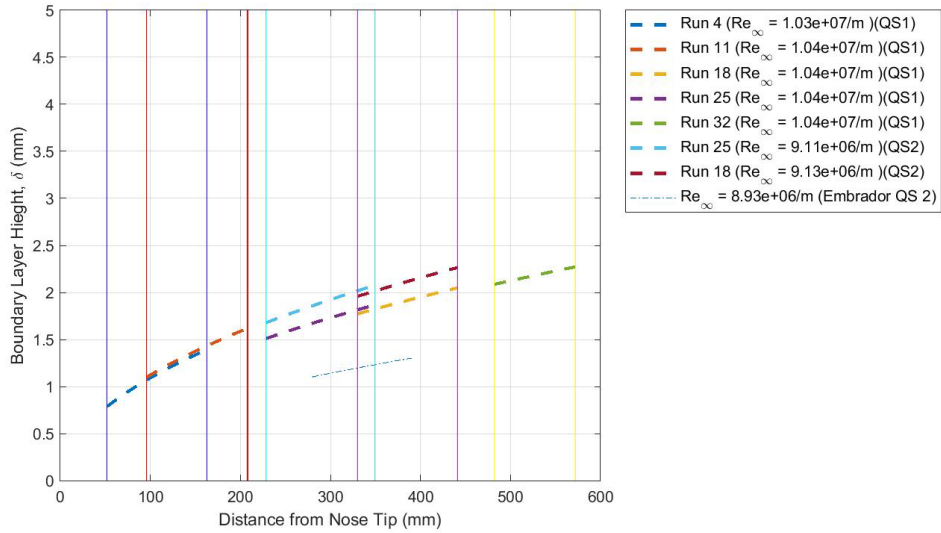

Figure 56: Laminar Boundary Layer Thickness for Uncooled Experiments at $P_{DT} = 200$ psi, $T_w/T_0 = .59$ ($T_w/T_e = 4.35 \pm 0.15$)
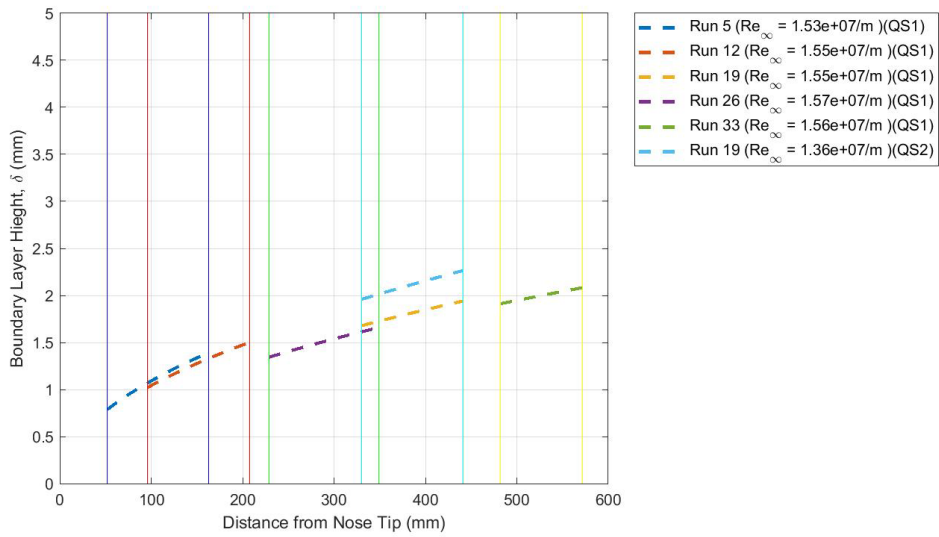
Figure 57: Laminar Boundary Layer Thickness for Uncooled Experiments at P$_{DT}$ = 300 psi, T$_w$/T$_0$ = .59 (T$_w$/T$_e$=4.35 ± 0.15)

Figure 58: Laminar Boundary Layer Thickness for Uncooled Experiments at P$_{DT}$ = 400 psi, T$_w$/T$_0$ = .59 (T$_w$/T$_e$=4.35 ± 0.15)

Figure 59: Laminar Boundary Layer Thickness for Uncooled Experiments at P_{DT} = 500 psi, T_w/T_0 = .59 (T_w/T_e=4.35 ± 0.15)
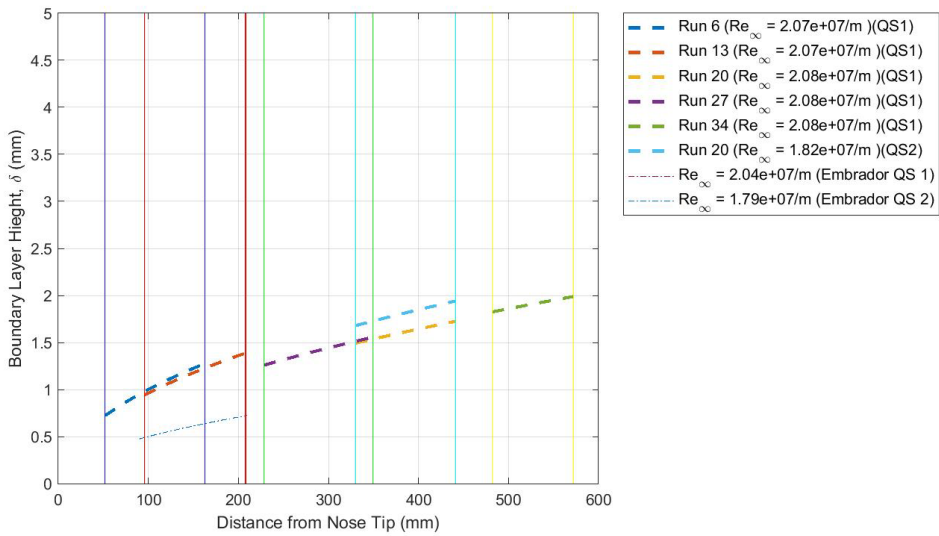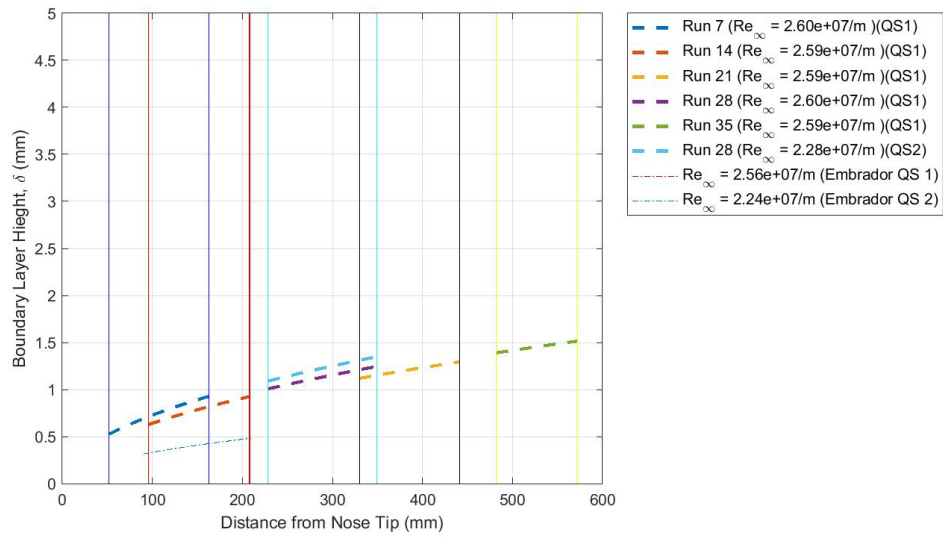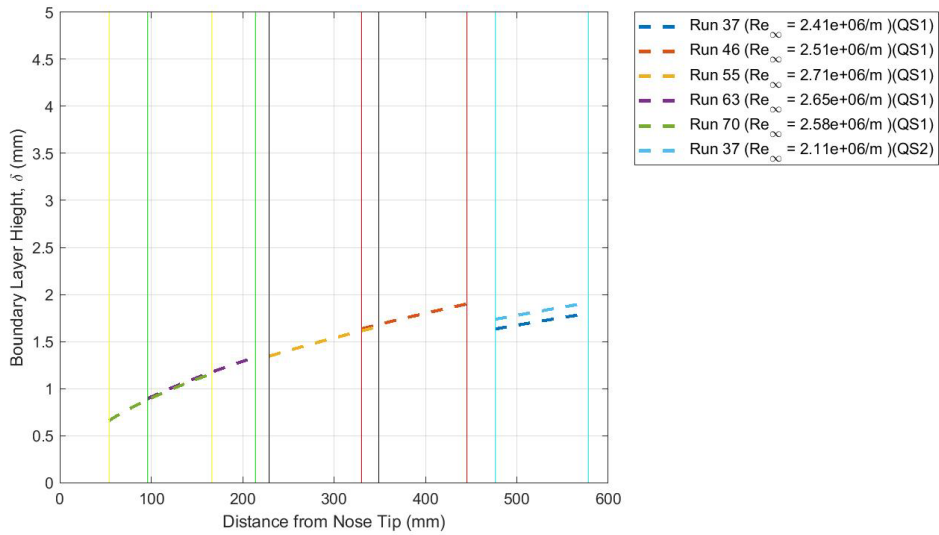
Cooled Data

Figure 60: Laminar Boundary Layer Thickness for Uncooled Experiments at P_{DT} = 50 psi, T_w/T_0 = .19 (T_w/T_e=1.40 ± 0.05)

Figure 61: Laminar Boundary Layer Thickness for Cooled Experiments at P_{DT} = 100 psi, T_w/T_0 = .19 (T_w/T_e=1.40 ± 0.05)

Figure 62: Laminar Boundary Layer Thickness for Cooled Experiments at P_{DT} = 150 psi, T_w/T_0 = .19 (T_w/T_e=1.40 ± 0.05)

Figure 63: Laminar Boundary Layer Thickness for Cooled Experiments at P_{DT} = 200 psi, T_w/T_0 = .19 (T_w/T_e=1.40 ± 0.05)

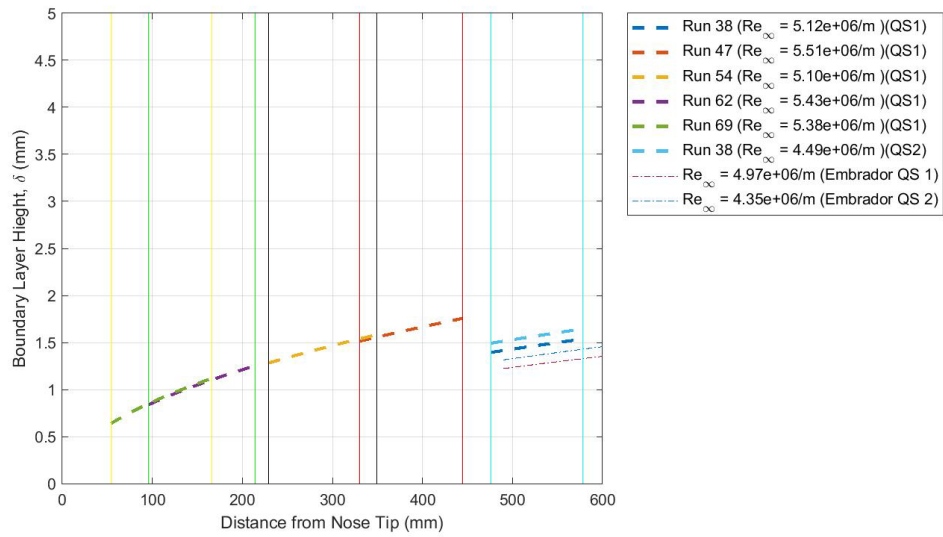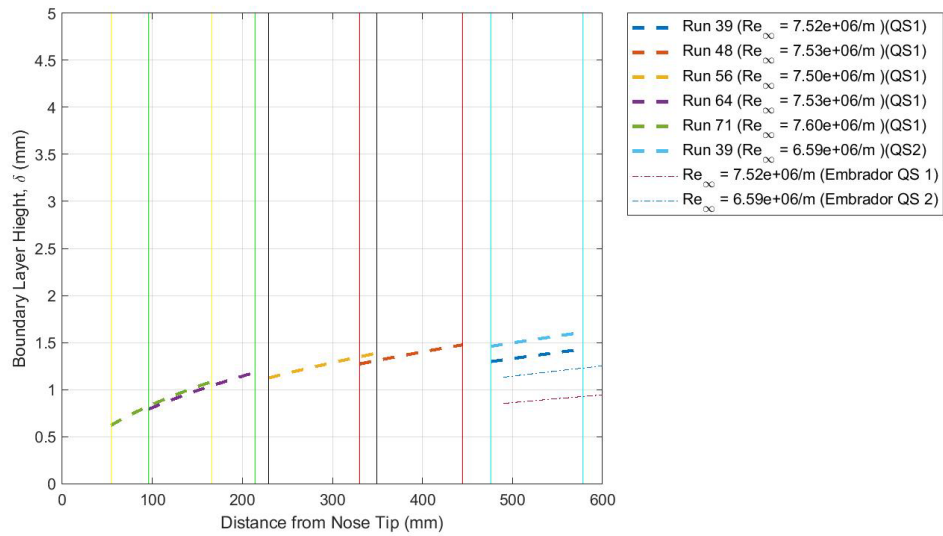**Figure 64: Laminar Boundary Layer Thickness for Cooled Experiments at P_{DT} = 300 psi, T_w/T_0 = .19 (T_w/T_e=1.40 ± 0.05)**

Figure 65: Laminar Boundary Layer Thickness for Cooled Experiments at P$_{DT}$ = 400 psi, T$_w$/T$_0$ = .19 (T$_w$/T$_e$=1.40 ± 0.05)

Figure 66: Laminar Boundary Layer Thickness for Cooled Experiments at P$_{DT}$ = 500 psi, T$_w$/T$_0$ = .19 (T$_w$/T$_e$=1.40 ± 0.05)
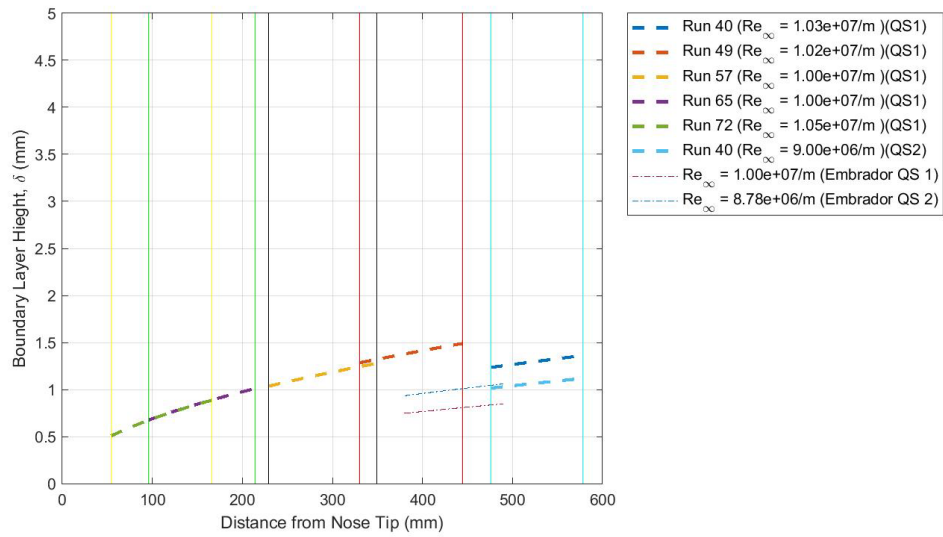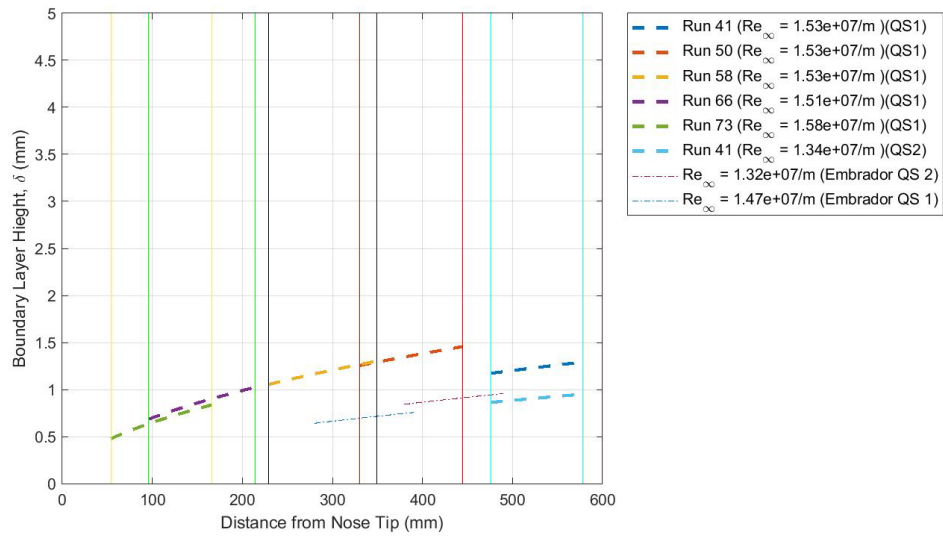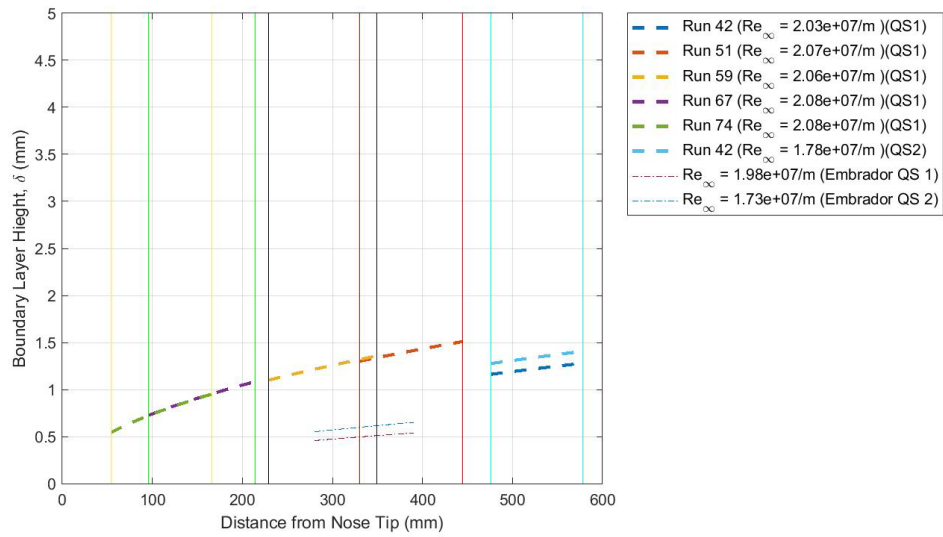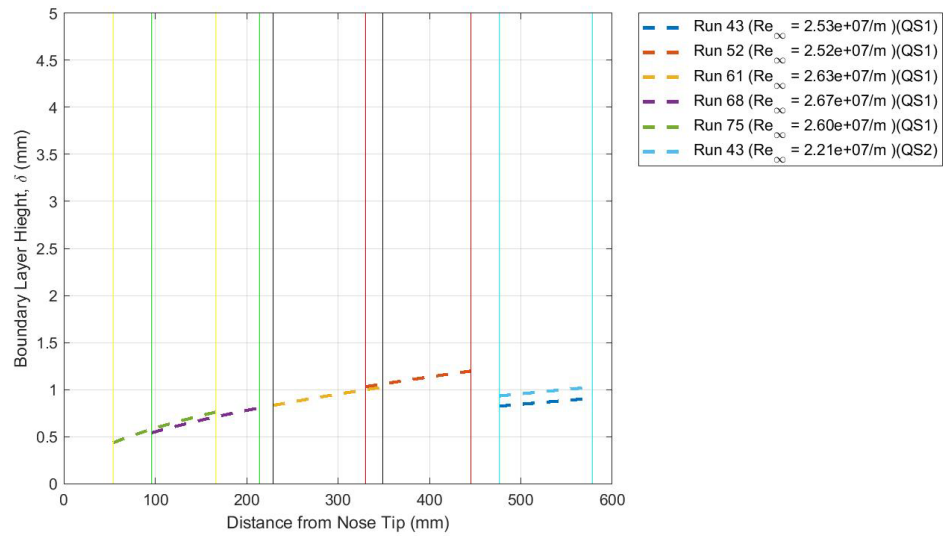
Bibliography

[1] T. Lin, "Influence of Laminar Boundary Layer Transition on Entry Vehicle Design," *Journal of Spacecraft and Rockets,* vol. 45, no. 2, pp. 165-175, 2008.

[2] N. P. Bitter, "Stability of Hypervelocity Boundary Layers," PhD thesis, California Institute of Technology, Pasadena, CA, 2015.

[3] L. Mack, Boundary Layer Linear Stability Theory, Pasadena, CA: California Institute of Technology, 1984.

[4] L. Lees, "The Stability of the Laminar Boundary Layer in a Compressible Fluid," NACA, Tech. Rep. 876, Pasadena, CA, 1947.

[5] K. F. Stetson, E. R. Thompson, J. C. Donaldson and L. G. Siler, "Laminar Boundary Layer Stability Experiments on a Cone at Mach 8, Part 5: Tests with a Cooled Model," in *AIAA 20th Fluid Dynamics: Plasma Dynamics and Lasers Conference*, Buffalo, NY, 1989.

[6] J. M. Kendall, "Wind Tunnel Experiments Relating to Supersonic and Hypersonic Boundar-Layer Transition," *AIAA Journal,* vol. 13, no. 3, pp. 290-299, 1975.

[7] P. E. Everhart and H. H. Hamilton, "Experimental Investigation of Boundary Layer Transition on a Cooled 7.5 Degree Total-Angle Cone at Mach 10," NASA TN D-4188, Hampton, VA, 1967.

[8] T. J. Juliano, D. Adamczak and R. L. Kimmel, "HIFiRE-5 Flight Test Results," *Journal of Spacecraft and Rockets,* vol. 52, no. 3, pp. 650-663, 2015.

[9] R. Oddo, "High-speed Schlieren Imaging of Second Mode Disturbances in a Super-Cooled Hypersonic Boundary Layer," Air Force Institute of Technology, Wright-Patterson AFB, OH, 2020.

[10] J. Embrador, "Effects of Highly-Cooled Walls on Hypersonic Boundary Layer Transition and Turbulence," Air Force Institute of Technology, Wright-Patterson AFB, OH, 2021.

[11] R. Oddo, J. L. Hill, M. F. Reeder, D. Chin, J. Embrador, J. Komives, M. Tufts, M. Borg and J. S. Jewell, "Effect of Surface Cooling on Second Mode Dominated Hypersonic Boundary Layer Transition," *Experiments in Fluids,* vol. 144, no. 62, pp. 1-18, 2021.

[12] S. P. Schnieder, "Hypersonic Laminar–Turbulent Transition on Circular Cones and Scramjet Freebodies," *Progress in Aerospace Sciences,* vol. 40, no. 1, pp. 1-50, 2004.

[13] J. Anderson, Fundamentals of Aerodynamics Sixth Edition, New York, NY: McGraw Hill, 2017.

[14] R. Karwa, "Convective Heat Transfer," in *Heat and Mass Transfer*, Jodhpur, India, Springer, 2020, pp. 381-538.

[15] R. L. Panton, Incompressible Flow, Hoboken, NJ: Wiley, 2013.

[16] W. M. Kays and M. E. Crawford, Convective Heat and Mass Transfer, 3rd ed., Highstown, NJ: McGraw Hill, 1993.

[17] F. M. White, Viscous Fluid Flow, New York, NY: McGraw Hill, 1974.

[18] E. R. V. Dreist, "Investigation of Laminar Boundary Layers in Compressible Fluids Using the Crocco Method," NACA TN 2597, 1952.

[19] E. R. Von Dreist, "Investigation of Laminar Boundary Layers in Compressible Fluids Using the Crocco Method," NACA TN 2597, Washington D.C., 1952.

[20] J. Anderson, Hypersonic and High Temperature Gas Dynamics Second Edition, Retson: AIAA, 2006.

[21] K. F. Stetson, E. R. Thompson, J. C. Donaldson and L. G. Siler, "On Hypersonic Transition and Testing," in *15th Aerodynamic Testing conference*, San Diego, CA, 1988.

[22] M. V. Morkovin, "Critical Evaluation of Transition from Laminar to Turbulent Shear Layers with Emphasis on Hypersonic Traveling Bodies," Research Institute For Advanced Studies, Baltimore, MD, 1968.

[23] H. L. Reed, W. S. Saric and D. Arnal, "Linear Stability Theory Applied to Boundary Layers," *Annual Review of Fluid Mechanics,* vol. 28, no. 1, pp. 389-428, 1996.

[24] K. F. Stetson and R. Kimmel, "On Hypersonic Boundary-Layer Stability," in *30th Aerospace Sciences Meeting and Exhibit*, Reno, NV, 1992.

[25] Y. S. Kachanov, "Physical Mechanisms of Laminar-Boundary-Layer Transition," *Annual Review of Fluid Mechanics,* vol. 26, no. 1, pp. 411-483, 1994.

[26] W. S. Saric, E. B. White and H. L. Reed, "Boundary Layer Receptivity to Freestream Disturbances and Its Role in Transition (INVITED)," in *30th AIAA Fluid Dynamics Conference*, Norfolk, VA, 1999.

[27] A. Federov, "Transition and Stability of High-Speed Boundary Layers," *Annual Review: Fluid Mechanics,* vol. 43, no. 1, pp. 79-95, 2010.

[28] M. V. Markovin, "On the Many Faces of Transition," in *C.S. Wells (eds) Viscous Drag Reduction*, New York, New York, 1969.

[29] J. Ren, Y. Xi and S. Fu, "The New Mode of Instability in Viscous High-Speed Boundary Layer Flows," *Advances in Applied Mathematics and Mechanics,* vol. 10, no. 5, pp. 1057-1068, 2018.

[30] Y. S. Kachanov, V. V. Kozlov and L. V. Y, "Beggining of Turbulence in Boundary Layers," *Novosibirsk: Nauka, Siberian Div.,* 1982.

[31] L. Duan, M. M. Choudhari, A. Chou, F. Munoz, R. Radespiel, T. Schilden, W. Schröder, E. C. Marineau, K. M. Casper, R. S. Chaudhry, G. V. Candler, K. A. Gray and S. P. Schneider, "Characterization of Freestream Disturbances in Conventional Hypersonic Wind Tunnels," *Journal of Spacecraft and Rockets,* vol. 56, no. 2, pp. 357-368, 2019.

[32] L. M. Mack, "Linear Stability Theory and the Problem of Supersonic Boundary Layer Transition," *AIAA Journal,* vol. 13, no. 3, pp. 278-289, 1975.

[33] J. S. Jewell and R. L. Kimmel, "Boundary-Layer Stability Analysis for Stetson's Mach 6 Blunt-Cone Experiments," *Journal of Spacecraft and Rockets,* vol. 54, no. 1, pp. 258-265, 2017.

[34] A. Federov and A. Tumin, "High-Speed Boundary-Layer Instability: Old Terminology and a New Framework," *AIAA Journal,* vol. 49, no. 8, pp. 1647-1657, 2011.

[35] L. Mack, "Boundary Layer Stability Theory," JPL Report, Pasadena, CA, 1969.

[36] C. Zhang, Y. Zhu, X. Chen, H. Yuan and J. Wu, "Transition in Hypersonic Boundary Layers," *AIP Advances,* vol. 5, no. 1, pp. 1-6, 2015.

[37] C. Knisely, "Supersonic Unstable Modes in Hypersonic Boundary Layers with Thermochemical Nonequilibrium Effects," UCLA, Los Angeles, CA, 2018.

[38] N. D. Sandham, "Shock-wave/Boundary-Layer interactions," NATO, South Hampton, UK, 2017.

[39] C. P. Knisely and X. Zhong, "Significant Supersonic Modes and the Wall Temperature Effect in Hypersonic Boundary Layers," *AIAA Journal,* vol. 57, no. 4, pp. 1552-1566, 2019.

[40] S. Craig, R. Humble, J. Hofferth and W. Saric, "Nonlinear Behaviour of the Mack Mode in a Hypersonic Boundary Layer," *Journal of Fluid Mechanics,* vol. 872, no. 8, pp. 72-89, 2017.

[41] S. P. Schnieder, "Flight Data for Boundary Layer Transition at Hypersonic and Supersonic Speeds," *Journal of Spacecraft and Rockets,* vol. 36, no. 1, pp. 8-20, 1999.

[42] K. W. Cassel, A. I. Rubin and D. A. Walker, "The Influence of Wall Cooling on Hypersonic Boundary-Layer Seperation and Stability," *Journal of Fluid Mechanics,* vol. 321, no. 8, pp. 189-216, 1996.

[43] K. Kara, P. Balakumar and O. A. Kandil, "The Effects of Wall Cooling on Hypersonic Boundary Layer Receptivity Over a Cone," in *38th Fluid Dynamics Conference and Exhibit*, Seattle, WA, 2008.

[44] A. Fedorov, A. Sidorenko, Y. Gromyko, D. Bountin, P. Polivanov and A. Maslov, "High Speed Boundary Layer Stability on a Cone with Localized Wall Heating or Cooling," *AIAA Journal,* vol. 53, no. 9, pp. 2512-2524, 2015.

[45] J. R. Jack, R. J. Wisniewski and N. S. Diaconis, "Effects of Extreme Cooling on Boundary-Layer Transition," NACA, Tech. Rep., Cleveland, OH, 1957.

[46] J. R. Jack and R. J. Winiewski, "Recent Studies on the Effect of Cooling on Boundary-Layer Transition at Mach 4," *Journal of Aerospace Science,* vol. 3, no. 4, pp. 250-251, 1961.

[47] J. L. Potter, "Review of the Influence of Cooled Walls on Boundary-Layer Transition," *AIAA Journal,* vol. 18, no. 8, pp. 1010-1012, 1980.

[48] K. F. Steston and G. H. Rushton, "Shock Tunnel Investigation of Boundary-Layer Transition at M=5.5," *AIAA Journal,* vol. 5, no. 5, pp. 899-906, 1967.

[49] G. C. Mateer, "Effects of Wall Cooling and Angle of Attack on Boundary Layer Transition on Sharp Cones at M=7.4," NASA TN D-6908, Moffett Field, CA, 1972.

[50] A. Hameed, N. J. Parziale, L. Paquin, S. J. Laurence and C. Butler, "Spectral Analysis of a Hypersonic Boundary Layer on a Right, Circular Cone," in *AIAA SciTech Forum*, Orlando, FL, 2020.

[51] A. Demetriades, "New Experiments on Hypersonic Boundary Layer Stability Including Wall Temperature Effects," in *Proceedings of the 26th Meeting of the Heat Transfer and Fluid Mechanics Institute*, Pullman, WA, 1978.

[52] E. A. Blanchard, V. G. Selby and P. S. Wilkinson, "A Quiet Tunnel Investigation of Hypersonic Boundary-Layer Stability Over a Cooled, Flared Cone," NASA Langley Research Center, Hampton, VA, 1996.

[53] R. J. Sanator, J. P. Decarlo and D. T. Torrillo, "Hypersonic Boundary-Layer Transition Data for a Cold-Wall Slender Cone," *AIAA Journal,* vol. 3, no. 4, pp. 758-760, 1965.

[54] R. E. Deem and J. S. Murphy, "Flat-Plate Boundary Layer Transition at Hypersonic Speeds," USAF Flight Dynamics Lab, FDL-TDR-64-129, Wright-Patterson AFB, OH, 1964.

[55] V. I. Lysenko, A. A. Maslov and N. M. Semenov, "Experimental Study of the Effect of Wall Heating on the Transition and Stability of Supersonic Boundary Layers," *Fluid Mechanics - Soviet Research,* vol. 11, no. 6, pp. 32-43, 1982.

[56] H. Goparaju, S. Unnikrishnan and D. V. Gaitonde, "The Effect of Nose Bluntness on Hypersonic Boundary Layer Receptivity and Stability," *Journal of Spacecraft and Rockets,* vol. 58, no. 3, pp. 669-684, 2021.

[57] N. R. Rotta, "EFFECTS OF NOSE BLUNTNESS ON THE BOUNDARY LAYER CHARACTERISTICS OF CONICAL BODIES AT HYPERSONIC SPEEDS," Office of Naval Research, New York, NY, 1966.

[58] K. F. Stetson, "Hypersonic Boundary Layer Transition Experiments," Air Force Wright Flight dynamics Labratory, Wright Patterson Air Force Base, OH, 1980.

[59] R. E. Kennedy, E. K. Jagde, S. J. Laurence, J. S. Jewell and R. L. Kimmel, "Visualization of Hypersonic Boundary-Layer Transition on a Variable Bluntness Cone," in *AIAA Aviation Forum*, Dallas, TX, 2019.

[60] G. Grossir, F. Pinna, G. Bonucci, T. Regert, P. Rambaud and O. Chazot, "Hypersonic Boundary Layer Transition on a 7 Degree Half-Angle Cone at Mach 10," in *AIAA AVIATION Forum*, Atlanta, GA, 2014.

[61] M. R. Malik, R. E. Spall and C. L. Chang, "Effect of Nose Bluntness on Boundary Stability and Transition," in *28th Aerospace Science Meeting*, Hampton, VA, 1990.

[62] K. F. Stetson, "Laminar Boundary Layer Stability Experiments on a Cone at Mach 8, Part 2: Blunt cone," in *AIAA 22nd Aerospace Sciences Meeting*, Reno, NV, 1984.

[63] K. F. Stetson and G. H. Rushton, "Shock Tunnel Investigation of Boundary Layer Transition at M=5.5," *AIAA Journal,* vol. 5, no. 5, pp. 899-906, 1967.

[64] Y. Zhang, J. Chen, X. Yuan, X. Chen and X. Xiang, "Hypersonic boundary layer receptivity on flat plate with blunt leading edge due to acoustic disturbances," in *The 11th Asia Conference on Mechanical and Aerospace Engineering*, Chengdu, China, 2020.

[65] X. Zhong and Y. Ma, "Boundary-Layer Receptivity of Mach 7.99 Flow over a Blunt Cone to Free-Stream Acoustic Waves," *Journal of Fluid Mechanics,* vol. 556, no. 1, pp. 55-103, 2006.

[66] A. Fedorov and A. Tumin, "Evolution of Disturbances in Entropy Layer on Blunted Plate in Supersonic Flow," *AIAA Journal,* vol. 42, no. 1, pp. 89-94, 2004.

[67] A. A. Maslov, "Experimental Study of Stability and Transition of Hypersonic Boundary Layer Around Blunted Cones," Institute of Theoretical and applied Mechanics, Novosibirsk, Russia, 2001.

[68] D. A. Cook, J. Thome, J. M. Brock, J. Nichols and G. Candler, "Understanding Effects of Nose-Cone Bluntness on Hypersonic Boundary Layer Transition Using Input-Output Analysis," in *2018 AIAA Aerospace Sciences Meeting*, Kissimmee, FL, 2018.

[69] K. M. Casper, S. J. Beresh, J. F. Henfling, R. W. Spillers and B. O. Pruett, "High-Speed Schlieren Imaging of Disturbances in a Transitional Hypersonic Boundary Layer," in *51st AIAA Aerospace Sciences Meetings including the New Horizons Forum and Aerospace Exposition*, Grapevine, TX, 2013.

[70] E. K. Jagde, R. E. Kennedy, S. J. Laurence, S. J. Jewell and R. L. Kimmel, "Visualizations of Boundary-Layer Transition on a Sharp Cone at Mach 6," in *AIAA Aviation 2019 Forum*, Dallas, TX, 2019.

[71] R. Kimmel, M. Borg, J. Jewell, K. Yiu Lam, R. Bowersox, R. Srinivasan and S. Fuchs, "AFRL Ludweig Tube Initial Performance," Air Force Research Lab Aerospace Systems Directorate, Wright Patterson AFB, OH, 2017.

[72] D. Labuda, J. Komives, M. Reeder, M. Borg and J. Jewell, "Schlieren Imaging on Cone Variations in the AFRL Ludweig Tube," in *AIAA AVIATION Forum*, Virtual Event, 2020.

[73] A. Mazumdar, "Principles and Techniques of Schlieren Imaging Systems," Columbia University, New York, NY, 2013.

[74] K. F. Stetson, "Nosetip Bluntness Effects on Cone Frustrum Boundary Layer Transition in Hypersonic Flow," in *AIAA 16th Fluid and Plasma Dynamics Conference*, Danvers, MA, 1983.

[75] K. Kara, P. Balakumar and O. A. Kandil, "Effects of Nose Bluntness on Stability of Hypersonic Boundary Layers Over Blunt Cones," in *37th AIAA Fluid Dynamics Conference and Exhibit*, Miami, FL, 2007.

[76] J. L. Hiil, "Experimental Measurements of Hypersonic Instabilities Over Ogive-cylinders at Mach-6," Air Force Institute of Technology, Fairborn, OH, 2020.

1. REPORT DATE *(DD-MM-YYYY)* 24-03-2022	2. REPORT TYPE Master's Thesis	3. DATES COVERED *(From – To)* August 2020 – March 2022

TITLE AND SUBTITLE EFFECTS OF CONE TIP CHANGES ON WALL-COOLED HYPERSONIC BOUNDARY LAYER TRANSITION AND TURBULENCE	5a. CONTRACT NUMBER
	5b. GRANT NUMBER
	5c. PROGRAM ELEMENT NUMBER

6. AUTHOR(S) Major, Mathew M., Mr., USAF	5d. PROJECT NUMBER JON 20Y328
	5e. TASK NUMBER
	5f. WORK UNIT NUMBER

7. PERFORMING ORGANIZATION NAMES(S) AND ADDRESS(S) Air Force Institute of Technology Graduate School of Engineering and Management (AFIT/EN) 2950 Hobson Way, Building 640 WPAFB OH 45433-7765	8. PERFORMING ORGANIZATION REPORT NUMBER AFIT-ENY-MS-22-M-307

9. SPONSORING/MONITORING AGENCY NAME(S) AND ADDRESS(ES) Air Force Research Laboratory 2145 5th Street, Building 24c WPAFB, OH 45433-7542 (937) 713-6697 matthew.borg.3@us.af.mil	10. SPONSOR/MONITOR'S ACRONYM(S)
	ASAFA (HVSI/AFOSR)
	11. SPONSOR/MONITOR'S REPORT NUMBER(S)

12. DISTRIBUTION/AVAILABILITY STATEMENT   DISTRUBTION STATEMENT A. APPROVED FOR PUBLIC RELEASE; DISTRIBUTION UNLIMITED.

13. SUPPLEMENTARY NOTES   This material is declared a work of the U.S. Government and is not subject to copyright protection in the United States.   Work was funded through USAFA (Prof. Russ Cummings). Work was performed and monitored at AFRL/RQH.

14. ABSTRACT

Boundary layer measurements took place at Air Force Research Lab's (AFRL) Mach-6 Ludwieg tube hypersonic wind tunnel on a 7-degree half angle spherically blunted nose cone with a 1.5 mm radius to study the effects of a cooled surface on the transition process. Experiments compared uncooled and cooled flow conditions on the blunt-nosed model, and then compared to past data for a sharp-tipped cone of similar geometry. Cooling the surface delayed the onset of transition on the blunt nose model. Combining the effects of nose blunting and cooling further increased transition delay than each acting individually compared to the sharp-tipped case. This outcome provides much needed data in an area of study with inconclusive results.

15. SUBJECT TERMS   Hypersonic, Boundary Layer Transition, Nose Bluntness, Surface Temperature

16. SECURITY CLASSIFICATION OF:			17. LIMITATION OF ABSTRACT	18. NUMBER OF PAGES	19a. NAME OF RESPONSIBLE PERSON Dr. Mark Reeder, AFIT/ENY
a. REPORT	b. ABSTRACT	c. THIS PAGE	UU	141	19b. TELEPHONE NUMBER *(Include area code)* (937) 255-6565, ext 4530; (mark.reeder@afit.edu)
U	U	U			